*eXPRESS Polymer Letters Vol.8, No.7 (2014) 458*
*Available online at www.expresspolymlett.com*
*DOI: 10.3144/expresspolymlett.2014.49*

# Editorial corner – a personal view
## Reviewing: Why, when, what and how?

*J. Karger-Kocsis*[*]

MTA–BME Research Group for Composite Science and Technology and Department of Polymer Engineering, Faculty of Mechanical Engineering, Budapest University of Technology and Economics, Műegyetem rkp. 3., H-1111, Budapest, Hungary

Researchers nowadays prefer to publish reviewing papers instead of writing book chapters. This is mostly due to the facts that books have a much smaller readership than journals, the book chapters are not properly cited, and citation data bases disregarded book contributions (fortunately this policy seems to be changing now). Last but not least, reviewing is a straightforward tool to boost the citations of the authors (which is frequently a key parameter for academic promotion). By surveying a given topic you may figure out those open issues which are worth of following in your future research. Another driving force of reviewing is to draw the attention for unsolved, acute problems when you are leaving a given research topic. Thus reviewing is an indispensable tool for guiding, 'channeling' the research.

Reviews usually address emerging 'hot' topics. When you have missed the right moment for that, you may still come out with good reviews thereby focusing on well selected, actual and until that time disregarded aspects. In that case you have to insert in the title of your paper 'recent advancements' or the like. This is a better strategy than to deliver an '$n$+1$^{th}$ visitation' to a well surveyed topic. Editors like 'critical reviews'. To the right criticism, however, you should have the necessary knowledge, overview and even some courage. Old, i.e. at present less 'fashionable', research themes may also deserve surveys. In this case the task of the writer is not only to 'dig in' properly in the history of the selected topic but also to pinpoint open left issues which can be clarified by contemporary experimental methods.

A review is, however, not merely a worded list of the related publications. The success, i.e. the acceptance by the community, well reflected by the citations, depends on the structuring of the information released. The outline of the review should be perfectly organized (the outline itself is a suitable advertisement for the paper) and to cover all aspects you want to refer to. To support this, you may think about new grouping, and even to introduce novel definitions. Beside of the clear definitions and well structured outline never forget about the 'artwork'. The artwork, included in a review, is of paramount importance! Researchers follow the scientific literature (if at all) via 'eye scanning'. Therefore good summary charts, 'self-explaining' schemes are the real 'eye catchers' and 'selling tools' of your review. A review is never 'complete' irrespective of the number of cited works. A mini review may be as useful as an exhaustive one provided that the current information is adequately shared with the reader.

According to my opinion reviewing is an art and thus not necessarily the task for everyone. You will learn, however, from reviewing activities a lot – so, why not to try yourself in this field, as well?

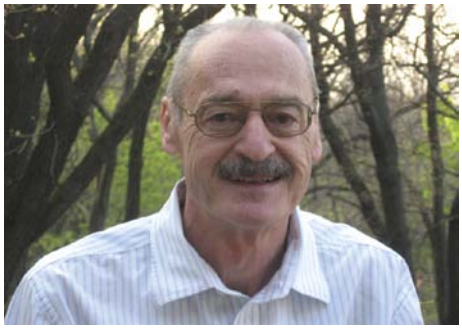

Prof. Dr. Dr. h.c. József Karger-Kocsis
Editor-in-Chief

[*]Corresponding author, e-mail: karger@pt.bme.hu

*eXPRESS Polymer Letters Vol.8, No.7 (2014) 459–466*
*Available online at www.expresspolymlett.com*
*DOI: 10.3144/expresspolymlett.2014.50*

# Ripple polystyrene nano-pattern induced by KrF laser

*P. Slepička[1,*], O. Neděla[1], J. Siegel[1], R. Krajcar[1], Z. Kolská[2], V. Švorčík[1]*

[1]Department of Solid State Engineering, Institute of Chemical Technology, 166 28 Prague, Czech Republic
[2]Faculty of Science, J.E. Purkyně University, Ústí nad Labem, Czech Republic

*Received 9 December 2013; accepted in revised form 26 February 2014*

**Abstract.** The study of excimer laser treatment of polystyrene surface was performed. The influence of laser fluence and number of laser pulses on surface chemistry and morphology was determined. The surface morphology and roughness were studied with atomic force microscopy. Surface wettability and aging studies were characterized by the water contact angle measurements. Surface oxygen concentration and chemistry were evaluated from X-ray photoelectron spectroscopy and zeta potential measurements. The optimal polystyrene treatment parameters for the most regular pattern were determined. The foils with optimal ripple pattern were subsequently sputtered with gold nano-layers of 100 nm thickness. It was found that the surface roughness of PS strongly depends on number of pulses. The aging study revealed that the higher contact angle achieve the samples treated with higher laser fluence. The deposition of gold nano-layer increases the surface roughness of nano-patterned surface. It was proved that the oxygen concentration is significantly influenced by the KrF laser exposure.

***Keywords:*** *nanomaterials, excimer laser, ripple pattern, polymer, metal coating*

## 1. Introduction

Excimer laser treatment has been recently used for production of LIPPS nanostructures on PS, PET, PI or semiconductor surfaces [1–3]. Different methods (ArF excimer laser irradiation and radio-frequency (RF) plasma treatment) were applied in separate procedures to create a vast range of physicochemical characteristics on the surface of polystyrene (PS) and investigate their effects on blood compatibility of treated surfaces [1]. The changes in surface topography and chemistry were analyzed by atomic force microscopy (AFM). Recently, one-dimensional metal nanostructures with high aspect ratio have drawn remarkable attention owing to their anisotropic electrical and optical properties that differ from those observed in the bulk materials. These properties offer interesting applications in various areas e.g. in electronic devices [4] or surface-enhanced Raman scattering (SERS) [5]. The detailed description of polystyrene ageing process, its morphological study and interaction with metal nanolayers after excimer laser treatment remained still unclear. Electrical conductivity of organic polymers can be permanently changed by the series of excimer laser pulses [1–5]. Therefore the polymers can be transformed in situ into an electrical conductors with sufficient space resolution (micrometer and lower). Advantages of conductivity change induced by excimer laser are its simplicity and easy adaptability to excimer laser equipment [6]. Factor which is limiting for potential applications of laser exposed polymers is the spatial resolution. By direct ablation of polyimide by KrF excimer laser it is possible to prepare lines with the width of less than 100 nm [7]. Such structures can be used in micro-electronics, e.g. for construction of semiconductor lasers in visible light area [8]. Metallization of polymer surface is important for several applications, involving microelectronic integrated circuits or bio-compatible carriers for medical applications. Adhesion at the metal/

*Corresponding author, e-mail: petr.slepicka@vscht.cz

polymer interface is influenced by the structure and chemical properties of material and can be, therefore, influenced by heat treatment, chemical etching or exposure of polymer to inert or reactive plasma before the metallization itself [9]. Also other methods for ripple nanopatterning have been proposed recently, which are based on the combination of plasma treatment, metallization and subsequent heating [10–12].

Polystyrene is a thermoplastic polymer widely used in many technological fields, such as micro-electronics, LOC (lab-on-chip) devices, membranes and scaffolds for cell cultivation [13]. The important PS properties are hardness, stiffness, easiness in thermal manufacturing and excellent thermal and electrical properties, they are easily applicable as insulators [14]. Functional properties are affected by low surface energy, hydrophobicity and low reactivity of this polymer. For suppression of last mentioned properties, and therefore improvement of adhesive potential of such substrate it is possible to use multiple approaches, such are e.g. plasma treatment or exposure by UV-lamp, so that the surface layer could be altered [15]. Increase of surface energy induced by these methods influences not only the adhesion, but also its tribological properties [16]. Laser beam allows performing precise changes of only small fragments or thickness of surface layer [17]. UV light can also induce several chemical reactions, which may alter the amount of surface polar groups on the surface [18, 19]. Nanosecond pulses of UV-beam of high energy lead to creation of significantly higher amount of radicals on the surface. Due to time dependence of diffusion processes in gas phase and surface layer cannot be the radicals fully saturated by reaction with air oxygen, therefore the recombination processes take place [15]. Physico-chemical processes connected with changes induced by laser beam are not still yet fully understood and are subject of continual intensive research [20]. Considerable attention has been devoted to laser assisted patterning and treatment of PS in connection with its application in research field of cell cultivation [21]. Changes of surface properties induced in the PS layer by ArF excimer laser were recently presented [22]. PET foils have been also treated with excimer lasers and the ripple pattern has been constructed [23, 24].

Papers regarding the nano-pattern formation on PS have been already published [21, 22, 25, 26]. Also their applications in cell biocompatibility were proposed [15, 21, 27]. The main motivation and novelty of the work is the detail study of PS wettability and ageing, morphology and zeta-potential changes induced by KrF laser, which are presented in this paper in detail. Also the growth of the consequently sputtered metal layers is described. The changes in the surface morphology were studied with atomic force microscopy (AFM), chemical structure was analyzed with X-ray induced photo-electron spectroscopy (ARXPS) and zeta potential measurement. Consequent metallization with gold nanolayer on selected pattern was performed and studied with AFM.

## 2. Materials and methods

Oriented PS foils with a thickness of 50 μm ($T_m$ ~ 240°C, $T_g$ ~ 100°C, supplied by Goodfellow Ltd., UK) were used.

The PS samples were treated with a KrF laser (Lambda Physik Compex Pro 50, wavelength of 248 nm, repetition rate 10 Hz). For the sake of homogeneity only central part of the beam profile, defined by an aperture 5×10 mm, was used for the irradiation. The samples were mounted onto a translation stage and scanned perpendicularly to the sample surface normal under ambient atmosphere (irradiation in air). The laser fluence used in present experiment was in interval 6–14 mJ·cm$^{-2}$, number of pulses varied from 200 to 8000, applied frequency was 10 Hz. The optical table Performance 07OTM501 (Melles Griot) with air pressured outriggers was used. For the polarization the cube of UV grade fused silica 25×25×25 mm$^3$ with active polarization layer was used. Optical path was constructed from dielectric mirrors from $SiO_2$ for reflectance 248/633 nm. The stage with the samples was directed by Laser XY software, the motorized shift NRT100/M2 (Melles Griot).

The gold layers on pristine and laser treated PS (original dimensions of non-treated sample 2×2 cm$^2$, the treated area 0.5×1 cm$^2$) were deposited from a gold target (99.999%) by means of diode sputtering technique (BAL-TEC SCD 050 equipment). Typical sputtering conditions were: room temperature, time 300 s, total argon pressure of about 5 Pa, electrode distance of 50 mm and current 40 mA. For the layer thickness measurement the gold was deposited under the same conditions on a Si (100) substrate. The gold layer thickness was determined from scratches (steel

needle) measured with AFM. Typically five measurements on three scratches each were accomplished on each sample. The thickness of the gold layer sputtered under above described conditions was 100±10 nm.

The surface morphology was examined using the AFM. The AFM images were taken under ambient conditions on a Digital Instruments CP II set-up. The samples were mounted on a sample holders using double-sided adhesive tape. The 'tapping mode' was chosen for the measurements to minimize damage to the samples surfaces. A Veeco oxide-sharpened P-doped silicon probe RTESPA-CP attached to a flexible micro-cantilever was used near its resonant frequency of 300 kHz. The scans were acquired at ambient atmosphere at a line scanning rate of 1 Hz. All surfaces were characterized both quantitatively by measuring the mean roughness ($R_a$, 10×10 μm$^2$) and morphology. $R_a$ represents the arithmetic average of the deviations from the center plane of the sample. Four areas of each sample were scanned in order to obtain representative data.

Water contact angle (CA) characterizing surface wettability was determined by goniometry. The measurements of the CA were performed using distilled water on 4 different positions (i.e. 4 droplets, droplet volume 8 μL). The water drops were applied on surface of the substrate, photographed and evaluated by three-point method using the Surface Energy Evaluation System (Advex Instruments, CR). The error of contact angle measurements did not exceed ±5°.

An Omicron Nanotechnology ESCAProbeP spectrometer was used to measure ARXPS spectra. The 2×3 mm$^2$ area was analyzed. The X-ray source provided monochromatic radiation of 1486.7 eV. The spectra were measured stepwise with a step in the binding energy of 0.05 eV at each of the six different sample positions with respect to the detector axis, which translated into different angles (0, 67 and 81°). The spectra evaluation was carried out by using CasaXPS software. The concentrations of the elements were given in at %.

Zeta potential measurements of all samples were accomplished on SurPASS Instrument (Anton Paar GmbH, Austria) by a streaming current method and Helmholtz-Smoluchowski equation for zeta potential calculation was employed. Samples were studied inside the adjustable gap cell with an electrolyte of 0.001 mol·dm$^{-3}$ KCl at constant pH = 6.1. Two samples of each surface were measured four times with the relative error of 10%. Zeta potential was measured on pristine sample, and on sample treated by laser: (i) in parallel and (ii) perpendicularly to the ripple pattern to study an effect of surface roughness to surface chemistry, surface charge and zeta potential.

## 3. Results and discussion

### 3.1. Pattern properties and morphology

The first goal of our study was to determine the influence of different laser energies onto surface morphology when a constant number of pulses is applied. Polystyrene foils were exposed to the laser beam with fluences 6–12 mJ·cm$^{-2}$ using 6000 pulses (Figure 1). We determined that with increasing laser fluence a mild increase of surface roughness occurred (fluences below 10 mJ·cm$^{-2}$) (Figure 2). The consequent increase of laser fluence to up to 12 mJ·cm$^{-2}$ is connected with rapid increase of the surface roughness. The second goal was to determine the laser fluence from which the ripple pattern appears. For treated PS the value was determined to be 8 mJ·cm$^{-2}$. If the applied laser fluence is between 9 and 10 mJ·cm$^{-2}$ the fully developed ripple pattern accomplished with significant roughness increase appears. Consequent increasing of laser fluence leads to slow diminishing of ripple nano-pattern. The nano-pattern diminishing is connected with the roughness decrease, since the Z-values of pattern decrease (see Figure 2). The dimensions of fully developed ripples were determined as follows: for laser fluence 9 mJ·cm$^{-2}$ the height of the structures was (38.6±4.0) nm and the width was (250.0±12.3) nm, for fluence 10 mJ·cm$^{-2}$ the observed ripple height

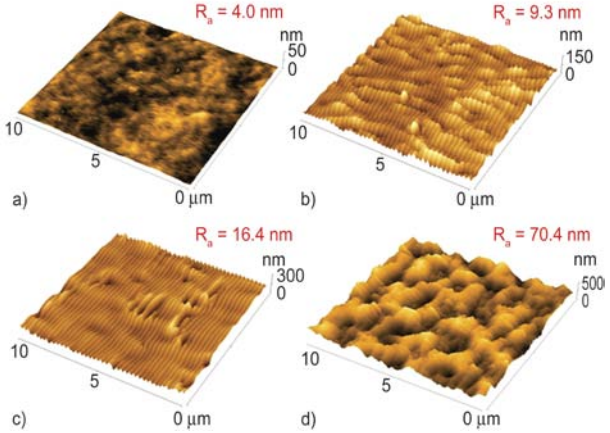


**Figure 1.** The surface morphology of PS exposed with laser fluence with 6 (a), 8 (b), 10 (c) and 12 mJ·cm$^{-2}$ (d) for number of pulses 6000. The $R_a$ represents the average surface roughness in nm.

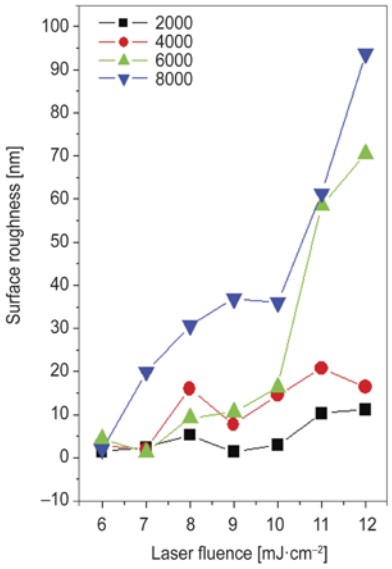


**Figure 2.** Dependence of PS surface roughness $R_a$ (10×10 μm$^2$) on laser fluence for number pulses 2000–8000

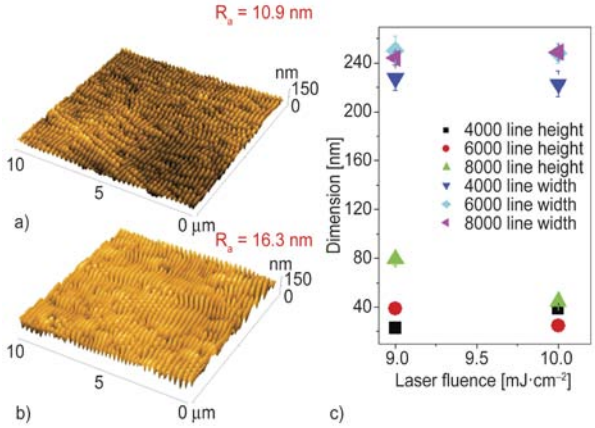


**Figure 3.** The surface morphology of PS treated with 12 mJ·cm$^{-2}$ and number of pulses 2000 (a) and 4000 (b). The dependence of the width and height of PS prepared structure on the laser fluence and by number of pulses 4000, 6000 and 8000 is introduced in (c).

was (24.8±0.7) nm and ripple width (247.8±7.8) nm. The results of pattern depth are with excellent agreement with those obtained [21]. The width periodicity is slightly higher, may be due to higher thickness of applied polymer foil (25 vs. 50 μm [21]). The thickness of polymer foil may influence the thermal flux, which can further lead to the slightly different results in comparison to [21].

Consequently, the whole experiment was repeated in the range of laser fluence 6–12 mJ·cm$^{-2}$ for 2000, 4000 and 8000 pulses (Figure 2). It was found, that for 2000 and 4000 pulses the mild roughness increase occurs. A rapid increase of surface roughness with increasing laser fluence was observed at 8000 pulses. If the laser fluence 6 mJ·cm$^{-2}$ is applied the $R_a$ does not change with the increasing number of pulses significantly, while for laser fluence 12 mJ·cm$^{-2}$ a rapid increase of $R_a$ is observed for 6000 pulses and above (Figure 2). It appears that if the higher laser fluence is applied (9–12 mJ·cm$^{-2}$, in combination with lower number of laser pulses), the homogeneous ripple pattern is also constructed on the PS surface (Figure 3). As expected, the number of pulses and laser fluence have a strong effect on ripple pattern formation [23, 24], the combination of high laser fluence and low number of laser pulses can lead to the homogeneous ripple nanopattern on PS, which as a consequence lead to the surface roughness increase (Figure 2 and Figure 3c).

### 3.2. Surface wettability and aging

The consequent metallization or cell adhesion and proliferation can be significantly enhanced or suppressed by the wettability (surface polarity) of the modified surface. Therefore we studied the surface contact angle of selected samples treated with laser fluence 6, 9, and 12 mJ·cm$^{-2}$ with laser pulses in the interval 200–6000 immediately after the exposure. It was observed, that with increasing number of laser pulses as a consequence the contact angle decreases (Figure 4a) in comparison to pristine PS, which confirms the increase of wettability after laser exposure and it is also with an agreement with work [21]. The contact angle decreases with the number of pulses up to certain value. After that a saturation value is reached and the contact angle is slightly increased with the number of pulses for some fluence (laser fluence 12 mJ·cm$^{-2}$). The hydrophilicity is increased due to formation of surface radicals after polymer bonds breakage caused by the impact and absorption of laser beam and consequent creation of new oxygen (polar) groups [28]. The application of laser fluence 12 mJ·cm$^{-2}$ leads to the minimum of contact angle for 3000 pulses, after which the slight increase of contact angle is observed again. The same trend was observed for laser fluence 9 mJ·cm$^{-2}$ and 5000 pulses. Also the possible ablation effects may have an influence of the amount of oxygen groups on the modified surface [28].

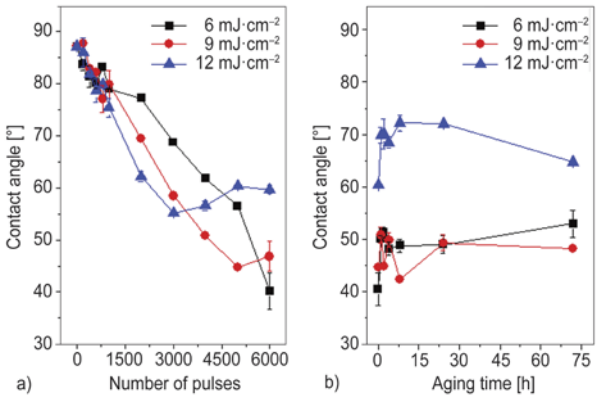


**Figure 4.** Dependence of contact angle of laser treated PS on number of laser pulses treated with fluences 6–12 mJ·cm$^{-2}$ (a). The graph (b) represents dependence of contact angle on time from the laser treatment (aging time) for samples exposured with 6000 pulses and laser fluence 6, 9 and 12 mJ·cm$^{-2}$

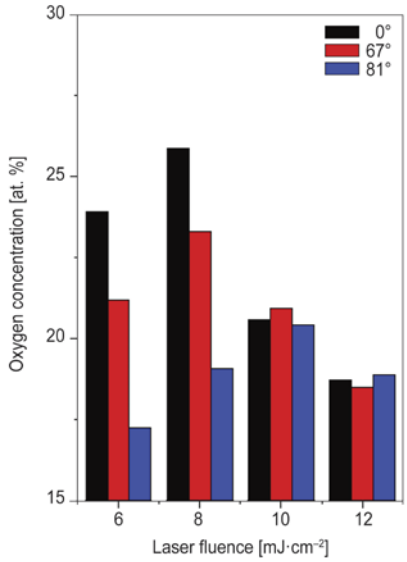


**Figure 5.** The dependence of oxygen concentration for treated PS on laser fluence (6000 pulses). The detection angles of photoelectrons by ARXPS were 0, 67 and 81°.

Consequently the samples were treated with 6–12 mJ·cm$^{-2}$ and 6000 pulses at ambient atmosphere, and the ageing procedure was followed in the interval 1–72 hours (Figure 4b). If the laser fluence 6 mJ·cm$^{-2}$ was applied, the mild increase of contact angle up to 50° was observed. The treatment with fluence 9 mJ·cm$^{-2}$ induced the fluctuation in contact angle during the early stages of aging. After 24 hours of consequent aging the mild constant decrease was determined. A different situation was observed if the fluence 12 mJ·cm$^{-2}$ was applied. At this laser fluence firstly a sharp increase up to 70° was observed, after achieving its maximum the following slow decrease was detected. After 72 hours the polymer surfaces can be signed as 'aged', i.e. with no further significant changes. The phenomenon of aging is connected with the amount of oxygenated groups and radicals on the modified surface and more importantly with the amount of oxygenated groups which rotated during the aging process into the polymer bulk. Also the ablation of surface modified layer may influence the different surface contact angle and its changes during the aging process. The knowledge of the aging process is of great importance, since together with the surface chemistry and morphology play an important role in biocompatibility applications [21].

### 3.3. Surface chemistry

The surface chemistry was evaluated by the surface oxygen concentration determined with ARXPS. The samples treated with 6–12 mJ·cm$^{-2}$ with 6000 pulses were determined (Figure 5). It was confirmed earlier, that excimer laser exposure may lead to a significant changes in in surface chemistry of biopolymer [12, 28]. It was found, that maximum oxygen concentration was detected under perpendicular position of the sample to the detector (i.e. 0°), which means, that the data are observed mostly from the whole plane of the sample. By changing the detection angle also a penetration depth of photoelectrons changes. With increasing angle of photoelectrons detection the oxygen concentration mostly decreased. Also the difference between the particular oxygen concentrations collected for the different detection angles decreases with the increasing laser fluence. The oxygen concentration and its distribution can have a significant influence on the consequent growth of the metal structures and may also influence cell growth and proliferation positively [21].

Zeta potential diagram can describe the surface charge and surface chemistry as a function of surface morphology due to inhomogeneity of created electrical double layer when the surface is rough. The zeta-potential determination is closely related to the oxygen concentration, wettability and ability to catch and release ions, which may have a significant influence on consequent biocompatibility applications and potentially can also influence the metal layer growth. The influence of ripple pattern on zeta potential determined by streaming current method is introduced in Figure 6. Apparently the

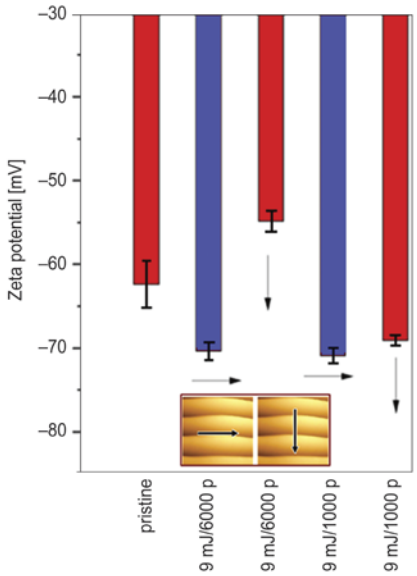


**Figure 6.** Zeta potential of pristine PS, PS treated with 9 mJ·cm$^{-2}$ and 6000 resp. 1000 pulses with perpendicular flow (to the ripple pattern) in the chamber (↑) and parallel flow (→) of the electrolyte

zeta potential depends strongly on surface roughness and morphology that means on the electrolyte flow through the surface in parallel or perpendicular position to the surface ripple pattern. It is evident, that the zeta potential values of PS treated with 9 mJ·cm$^{-2}$ (both 1000 and 6000 pulses) are almost similar, if the direction of the electrolyte flow applied on the PS surface is in parallel with the surface pattern structure. Rather different situation is observed, when the electrolyte is applied perpendicularly to the ripple pattern. The big difference of zeta potential evolution was achieved for 6000 pulses, when the difference in zeta potential was over 15 mV. The influence of ripple pattern on the ability of ion capturing and release was confirmed, since the PS surface treated with only 1000 pulses exhibited significantly lower difference if compared the perpendicular and parallel electrolyte flow. These differences can be caused by the amount of oxygen groups on surface. While the electrolyte flows parallel to the ripples, majority of oxygen groups created during laser treatment on surface (either on the 'hills' or in the 'valleys' of the surface) is in contact with electrolyte and electrical double layer is created homogenously on the whole surface. If the electrolyte flows perpendicularly to the ripples, the situation is different, due to the higher surface roughness electrical double layer is created only on the 'hills'. As it was proved previously, amount of oxygen groups created by laser treatment on the surface is different on the 'hills' and in the 'valleys' significantly [29].

### 3.4. Gold nanolayers deposition

The polystyrene exposed with laser fluence 6–12 mJ·cm$^{-2}$ and 6000 pulses was consequently metallized with 100 nm of Au layer so that the influence of input surface morphology and chemistry on consequent metallization could be studied. The gold sputtering increases the surface roughness in the interval of laser fluences 6–10 mJ·cm$^{-2}$ significantly, however on samples with no regular structure the sputtering has no such dramatic effect (Figure 7). The effect of roughness change is opposite to those obtained on PEN [30]. This difference is probably caused by the lower homogeneity of ripple pattern, which together with differences in surface chemistry can cause different gold nanocluster formation on the PS surface. However, the ripple pattern structure created in interval 8–10 mJ·cm$^{-2}$ is maintained also after gold sputtering process (Figure 8). For lower laser fluences the globular structure is preserved after Au metallization. On the contrary, the gold metallization does not have any significant influence on the surface roughness or pattern formation for higher laser fluences 11–12 mJ·cm$^{-2}$ (Figure 8c), because of higher ripple pattern roughness. It was also observed, that the width of the ripple pattern remains similar to that without metallization. The pattern of Au deposited foils was proved to be electrically continuous. The height of the ripple pattern increases or remains similar after Au metallization.

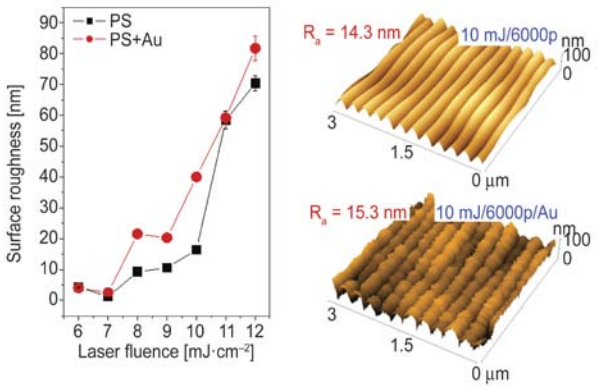


**Figure 7.** Dependence of PS surface roughness (10×10 µm$^2$) on laser fluence in the interval 6–12 mJ·cm$^{-2}$ (treated by 6000 pulses) and the same set of samples consequently metallized with 100 nm of Au. The AFM detail structure of laser treated PS (10 mJ·cm$^{-2}$ and 6000 pulses) and the same sample metallized with 100 nm of Au is also introduced.

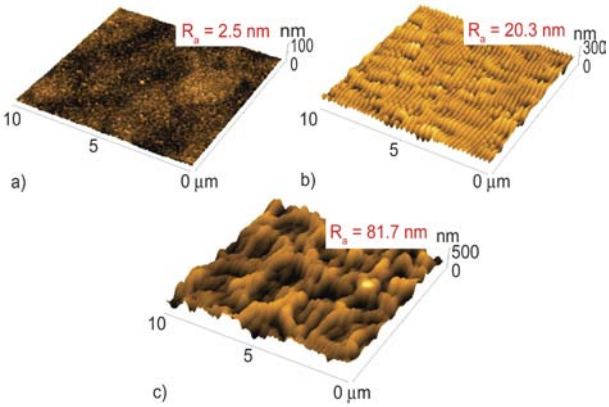


**Figure 8.** The surface morphology of PS laser treated (6000 pulses) by 7 (a), 9 (b) and 12 mJ·cm$^{-2}$ (c) and consequently metallized with 100 nm of Au. The $R_a$ represents the average surface roughness in nm.

## 4. Conclusions

A study of KrF laser treatment on PS foil surface was performed. The influence of number of laser pulses and laser fluence on surface properties (morphology, wettability and chemistry) of PS was investigated. The optimal input parameters for ripple nano-patterning with high regularity were determined. The input parameters for construction of ripple-like surface with extremely high roughness were determined. It was found that the surface roughness of PS is strongly dependent on number of pulses. The surface chemistry of exposed PS was studied with ARXPS and zeta potential measurements. It was proved, that the oxygen concentration is significantly influenced by the KrF laser exposure. The wettability strongly increases with number of pulses in comparison to the pristine PS. The aging study revealed that the higher contact angle achieves the samples treated with higher laser fluence. The PS ripple nano-pattern has a strong influence on the zeta potential of studied surface, i.e. it has the capability to influence the electrolyte flow (parallel vs. perpendicular position). The deposition of gold nano-layer increases the surface roughness of nano-patterned surface. As previously confirmed the applications of nano-patterned PS surface are promising as tissue carriers, metallized pattern can find application in construction of SERS.

## Acknowledgements

This work was supported by the Grant Agency of the CR under the project No. 13-06609S.

## References

[1] Bagheri-Khoulenjani S., Mirzadeh H.: Polystyrene surface modification using excimer laser and radio-frequency plasma: Blood compatibility evaluations. Progress in Biomaterials, **1**, 4/1–4/8 (2012). DOI: 10.1186/2194-0517-1-4

[2] Sanz M., Rebollar E., Ganeev R. A., Castillejo M.: Nanosecond laser-induced periodic surface structures on wide band-gap semiconductors. Applied Surface Science **278**, 325–329 (2013). DOI: 10.1016/j.apsusc.2012.11.137

[3] Zheng H. Y., Tan T. T., Zhou W.: Studies of KrF laser-induced long periodic structures on polyimide. Optics and Lasers in Engineering, **47**, 180–185 (2009). DOI: 10.1016/j.optlaseng.2008.06.015

[4] Xu F., Zhu Y.: Highly conductive and stretchable silver nanowire conductors. Advanced Materials, **24**, 5117–5122 (2012). DOI: 10.1002/adma.201201886

[5] Liu S., Chen N., Li L., Pang F., Chen Z., Wang T.: Fabrication of Ag/Au core-shell nanowire as a SERS substrate. Optical Materials, **35**, 690–692 (2013). DOI: 10.1016/j.optmat.2012.10.033

[6] Phillips H. M., Smayling M. C., Sauerbrey R.: Modification of electrical conductivity and surface structure in polymers using ultraviolet laser radiation. Microelectronic Engineering, **20**, 73–88 (1993). DOI: 10.1016/0167-9317(93)90208-M

[7] Phillips H. M., Callahan D. L., Sauerbrey R., Szabó G., Bor Z.: Sub-100 nm lines produced by direct laser ablation in polyimide. Applied Physics Letters, **58**, 2761–2763 (1991). DOI: 10.1063/1.104778

[8] Korn M., Körfer T., Forchel A., Roentgen P.: First order distributed feedback gratings (92.5–105 nm period) for GaInP/AlGaInP lasers emitting in the visible range. Journal of Vacuum Science and Technology B, **8**, 1404–1407 (1990). DOI: 10.1116/1.585086

[9] Le Q. T., Pireaux J. J., Verbist J. J.: Surface modification of PET films with RF plasma and adhesion of in situ evaporated Al on PET. Surface and Interface Analysis, **22**, 224–229 (2004). DOI: 10.1002/sia.740220150

[10] Slepička P., Trostová S., Slepičková Kasálková N., Kolská Z., Sajdl P., Švorčík V.: Surface modification of biopolymers by argon plasma and thermal treatment. Plasma Processes and Polymers, **9**, 197–206 (2012). DOI: 10.1002/ppap.201100126

[11] Slepička P., Fidler T., Vasina A., Švorčík V.: Ripple-like structure on PLLA induced by gold deposition and thermal treatment. Materials Letters **79**, 4–6 (2012). DOI: 10.1016/j.matlet.2012.03.070

[12] Slepička P., Michaljaničová I., Švorčík V.: Controlled biopolymer roughness induced by plasma and excimer laser treatment. Express Polymers Letters, **7**, 950–959 (2013). DOI: 10.3144/expresspolymlett.2013.92

[13] Malmsten M.: Biopolymers at interfaces. Mercel Dekker, New York (2003).
[14] Brostow W., Hagg Lobland H. E., Narkis M.: Sliding wear, viscoelasticity, and brittleness of polymers. Journal of Materials Research, **21**, 2422–2428 (2006). DOI: 10.1557/jmr.2006.0300
[15] Pfleging W., Torge M., Bruns M., Trouillet V., Welle A., Wilson S.: Laser- and UV-assisted modification of polystyrene surfaces for control of protein adsorption and cell adhesion. Applied Surface Science, **255**, 5453–5757 (2009). DOI: 10.1016/j.apsusc.2008.08.053
[16] Brostow W., Cassidy P. E., Macossay J., Pietkiewicz D., Venumbaka S.: Connection of surface tension with multiple tribological properties in epoxy + fluoropolymer systems. Polymer International, **52**, 1498–1505 (2003). DOI: 10.1002/pi.1283
[17] Bäuerle D., Denk R., Pedarning J. D., Piglmayer K., Heitz J., Schrems G.: Perspectives of laser processing and chemistry. Applied Physics A, **77**, 203–207 (2003). DOI: 10.1007/s00339-003-2155-z
[18] Rytlewski P., Zenkiewicz M.: Laser modification of polymeric materials. Part 2. Chemical reactions induced by laser beam. International Polymer Science and Technology, **34**, T/59–T/66 (2007).
[19] Oehr C.: Plasma surface modification of polymers for biomedical use. Nuclear Instruments and Methods in Physics Research Section B: Beam Interactions with Materials and Atoms, **208**, 40–47 (2003). DOI: 10.1016/S0168-583X(03)00650-5
[20] Wochnowski C., Shams Eldin M. A., Metev S.: UV-laser-assisted degradation of poly(methyl methacrylate). Polymer Degradation and Stability, **89**, 252–264 (2005). DOI: 10.1016/j.polymdegradstab.2004.11.024
[21] Rebollar E., Frischauf I., Olbrich M., Peterbauer T., Hering S., Preiner J., Hinterdorfer P., Romanin C., Heitz J.: Proliferation of aligned mammalian cells on laser-nanostructured polystyrene. Biomaterials, **29**, 1796–1806 (2008). DOI: 10.1016/j.biomaterials.2007.12.039
[22] Mirzadeh H., Bagheri Sh.: Comparison of the effect of excimer laser irradiation and RF plasma treatment on polystyrene surface. Radiation Physics and Chemistry, **76**, 1435–1440 (2007). DOI: 10.1016/j.radphyschem.2007.02.079
[23] Slepička P., Rebollar E., Heitz J., Švorčík V.: Gold coatings on polyethyleneterephthalate nano-patterned by F2 laser irradiation. Applied Surface Science, **254**, 3585–3590 (2008). DOI: 10.1016/j.apsusc.2007.11.045
[24] Slepička P., Chaloupka A., Sajdl P., Heitz J., Hnatowicz V., Švorčík V.: Angle dependent laser nanopatterning of poly(ethylene terephthalate) surfaces. Applied Surface Science, **257**, 6021–6025 (2011). DOI: 10.1016/j.apsusc.2011.01.107
[25] Lazare S., Bolle M., Cros A., Bellard L.: Periodic structuration of polymer surfaces with the excimer laser radiation. Nuclear Instruments and Methods in Physics Research Section B: Beam Interactions with Materials and Atoms, **105**, 159–163 (1995). DOI: 10.1016/0168-583X(95)00630-3
[26] Rytlewski P., Żenkiewicz M.: Laser-induced surface modification of polystyrene. Applied Surface Science, **256**, 857–861 (2009). DOI: 10.1016/j.apsusc.2009.08.075
[27] Pfleging W., Bruns M., Welle A., Wilson S.: Laser-assisted modification of polystyrene surfaces for cell culture applications. Applied Surface Science, **253**, 9177–9184 (2007). DOI: 10.1016/j.apsusc.2007.05.047
[28] Slepička P., Michaljaničová I., Sajdl P., Fitl P., Švorčík V.: Surface ablation of PLLA induced by KrF excimer laser. Applied Surface Science, **283**, 438–444 (2013). DOI: 10.1016/j.apsusc.2013.06.127
[29] Siegel J., Slepička P., Heitz J., Kolská Z., Sajdl P., Švorčík V.: Gold nano-wires and nano-layers at laser-induced nano-ripples on PET. Applied Surface Science, **256**, 2205–2209 (2010). DOI: 10.1016/j.apsusc.2009.09.074
[30] Slepička P., Neděla O., Sajdl P., Kolská Z., Švorčík V.: Polyethylene naphthalate as an excellent candidate for ripple nanopatterning. Applied Surface Science, **285**, 885–892 (2013). DOI: 10.1016/j.apsusc.2013.09.007

*eXPRESS Polymer Letters Vol.8, No.7 (2014) 467–479*
*Available online at www.expresspolymlett.com*
*DOI: 10.3144/expresspolymlett.2014.51*

# Enhanced thermal and mechanical properties of epoxy composites by mixing thermotropic liquid crystalline epoxy grafted graphene oxide

*B. Qi, S. R. Lu*, X. E. Xiao, L. L. Pan, F. Z. Tan, J. H. Yu*

Key Laboratory of New Processing Technology for Nonferrous Metals and Materials, Ministry of Education, School of Material Science and Engineering, Guilin University of Technology, 541004 Guilin, China

*Received 13 December 2013; accepted in revised form 8 March 2014*

**Abstract.** Graphene oxide (GO) sheets were chemically grafted with thermotropic liquid crystalline epoxy (TLCP). Then we fabricated composites using TLCP-g-GO as reinforcing filler. The mechanical properties and thermal properties of composites were systematically investigated. It is found that the thermal and mechanical properties of the composites are enhanced effectively by the addition of fillers. For instance, the composites containing 1.0 wt% of TLCP-g-GO present impact strength of 51.43 kJ/m$^2$, the tensile strength of composites increase from 55.43 to 80.85 MPa, the flexural modulus of the composites increase by more than 48%. Furthermore, the incorporation of fillers is effective to improve the glass transition temperature and thermal stability of the composites. Therefore, the presence of the TLCP-g-GO in the epoxy matrix could make epoxy not only stronger but also tougher.

***Keywords:*** *nanocomposites, thermotropic liquid crystalline epoxy, graphene oxide, mechanical properties, thermal properties*

## 1. Introduction

Epoxy resins are presently important organic matrices in composite industry. They are frequently used in demanding applications due to their excellent mechanical properties, thermal stability and chemical resistance. Furthermore, they also have good resistance to moisture, solvents and chemical attacks [1, 2]. However, their brittleness, poor resistance to crack propagation and poor wear resistance [3, 4] limit their applications. Numerous studies have been conducted to explore the toughness of epoxy composites [5, 6]. Addition of thermoplastic polymers can improve fracture toughness, but it is always at the expense of the glass transition temperature ($T_g$) and modulus or high cost [7]. Inorganic additives, such as silica and alumina have been used to increase the toughness of epoxies without sacrificing their basic properties, but the presence of numerous inorganic particles increase the viscosity leading to poor dispersion and processing difficulty [8–10].

In recent years, graphene oxide (GO) has attracted significant interest for the preparation of polymer composites due to its excellent mechanical [11], electrical and thermal properties, simple preparation technique and low cost [12]. GO can be regarded as graphene sheets derivatized with carboxylic groups at the edges and phenol, hydroxyl and epoxide groups on the basal planes [13–15]. These abundant oxygen-containing functional groups enable graphene to be further modified by chemical reactions, and thus many different functional groups can be introduced onto the graphene sheets. Accordingly, we can easily to prepare a variety of excellent functional composites.

Liquid crystalline epoxies (LCE) form a unique class of thermosetting materials, which combine the

*Corresponding author, e-mail: lushaor@163.com

properties of both liquid crystal and conventional thermosets, as shown by their anisotropic mechanical properties, excellent thermal stability and chemical resistance [16–18].Curing of low molecular weight, rigid rod, and multifunctional monomers result in the retention of a liquid crystalline phase by the three dimensional crosslinking networks [19, 20]. Hence, it can be used to improve toughness of composites. Unlike other additive such as rubber particles, the presence of liquid crystalline domains will not sacrifice $T_g$ or modulus of the material. These outstanding properties make LCE as good candidates for a wide range of potential applications, such as optical switches, electronic packaging, and matrices for high performance composites [21–23]. In this report, we firstly prepared GO by a modified Hummers method, then the GO was grafted by thermotropic liquid crystalline epoxy (TLCP-g-GO). The GO and grafted GO were characterized by Fourier-transform infrared spectra (FT-IR), wide angle X-ray diffraction (WAXD) and so on. Meanwhile, the epoxy composites were prepared by casting with the addition of 0.5, 1.0, 1.5, 2.0 and 3.0 wt% TLCP-g-GO. Finally, we studied the effect of the TLCP-g-GO on mechanical and thermal properties of the epoxy composites.

## 2. Experimental section

### 2.1. Materials

Nature flake graphite (325 mesh, 99%) was provided by Hengrui Graphite Co., Ltd. (Qingdao, China). Phydroxybenzoic acid and paraphthaloyl chloride were obtained from Xiya Chemical Reagent Company (Chengdu, China). Thionyl chloride ($SOCl_2$) and glycidol were purchased from Aladdin Chemistry Co., Ltd. (Shanghai, China). $H_2SO_4$ (98%), HCl (36%), $H_2O_2$ (30%), $KMnO_4$, $P_2O_5$ and $K_2S_2O_8$ were purchased from Sinopharm Chemical Reagent Co., Ltd. (Shanghai, China) and used without purification. N, N′-dimethylformamide (DMF) and pyridine were obtained from Xiya Chemical Reagent Company (Chengdu, China) and first refluxed over calcium hydride and then distilled under a reduced pressure prior to use. The epoxy resin used in this study is diglycidylether of bisphenol A (DGEBA, E-51, epoxy value = 0.51 and viscosity value = 12 Pa·s at 25°C) supplied by Yueyang Chemical Plant (Yueyang, China). 4, 4′-diaminodiphenylsulphone (DDS) purchased from Sinopharm Chemical Reagent Co., Ltd. (Shanghai, China), with a molecular mass of 248.31 and purity >96% according to the supplier. Deionized (DI) water was used in all the process of aqueous solution preparation and washing.

### 2.2. Preparation of graphene oxide (GO)

The modified Hummers method [24–26] was utilized to oxidize nature flake graphite for the synthesis of GO. The detailed processing is described as following: in a pretreatment step, $K_2S_2O_8$ (10 g) and $P_2O_5$ (10 g) were mixed with $H_2SO_4$ (98%, 80 mL) in a 500 mL beaker placed in water bath. The solution was stirred and heated to 90°C until the reactants were completely dissolved. Graphite powder (3 g) was then introduced into the acid. The mixture was kept at 90°C for 4.5 h under intensive stirring. Then the mixture was cooled to room temperature and diluted with DI water (1000 mL) and then filtered and washed to remove the residual acid. The product was dried under ambient conditions overnight.

In the second oxidation step, the pretreated graphite powder was put into 150 mL 98% $H_2SO_4$ at 0°C. Then $KMnO_4$ (10 g) was added slowly under stirring, and the temperature of the mixture was kept below 10°C by cooling. After that, the mixture was allowed to react at 35±3°C for 2 h. As the reaction progressed, the mixture gradually became pasty. The next step was to cool the suspension temperature to 20°C, and DI water (500 mL) was added with vigorous agitation. The mixture was stirred for 6 h, and then additional DI (700 mL) water was added. 30% $H_2O_2$ was added to the mixture until the color of the suspension changed to brilliant yellow. For purification, the mixture was rinsed and centrifuged with 5% HCl and DI water for several times. The collected graphite oxide was dispersed in DI water by ultrasonication to exfoliate the graphite oxide to GO, the suspension was dried by freeze-drying machine. Finally, GO obtained 1s a spongy solid.

### 2.3. Synthesis of the liquid crystalline epoxy grafted graphene oxide (TLCP-g-GO)

Typical procedure of preparing TLCP-g-GO is described as Figure 1. To functionalize GO, the as-prepared GO (0.1 g) was placed in a 250 mL dried three-necked flask with 100 mL DMF/pyridine (10:1) mixing solvent and dispersed through sonication for 30 min. Then 15 mL DMF containing 28 mmol paraphthaloyl chloride was slowly dropped into the GO suspension at 0~5°C, and the mixture was stirred at

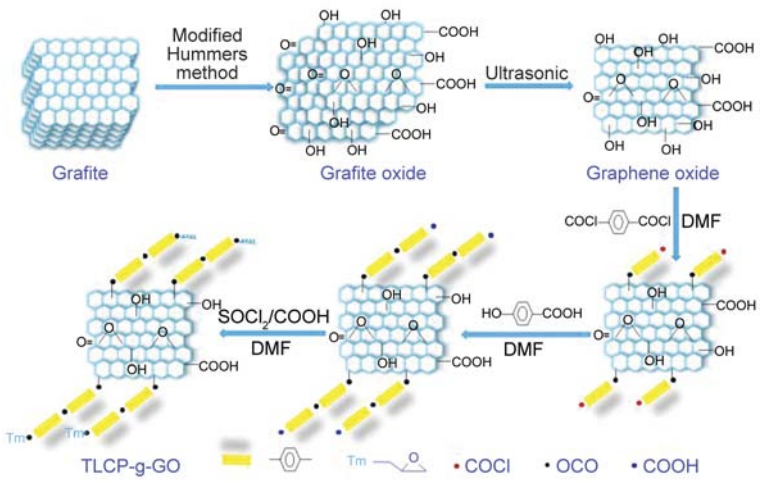


**Figure 1.** The synthetic routes of TLCP grafted GO

60°C for 12 h. After the reaction finished, 10 mL $SOCl_2$ was loaded in the flask at ambient temperature. The mixture was kept at 65°C under stirring, using a $CaC_{12}$ guard tube. After 24 h, the excess $SOCl_2$ was removed by distillation, and the product was allowed to react with 5 mL glycidol at 60°C for 12 h. After cooling, the solution was poured into plenty of DI water. The precipitate was collected by filtration and washed with a mixture water/ethanol several times. The solid was vacuum dried at 60°C for overnight. The last, TLCP-g-GO was obtained.

## 2.4. Preparation of TLCP-g-GO/epoxy composites

Composition of epoxy composites was as follows. The required amount of filler was first dispersed in acetone by sonication for 30 min. This dispersion was then mixed with epoxy resin to give concentrations of 0.5, 1.0, 1.5, 2.0 and 3.0 wt% grafted GO as compared to the weight of the epoxy resin. The mixture was stirred under high-speed for 0.5 h for homogenization. In order to evaporate the acetone, the mixture was degassed for at 120°C for 2 h. After that, epoxy resin was mixed with stoichiometric amounts of DDS (30 g/100 g of epoxy resin) at 150°C for 30 min. The resulting mixture was then cast into a preheated mould coated with silicone resin. The residual solvent and bubbles in the mixture were removed by placing the mold in a vacuum oven for 30 min at 120°C. Finally, the mold was placed in a convection oven to cure at 120°C for 2 h, 160° C for 2 h and 180°C for 2 h. The details of the process of epoxy composites are shown as Figure 2.

## 2.5. Characterization

Fourier-transform infrared spectra (FT-IR) were recorded on a Perkin-Elmer 1710 spectrophotometer. The frequency range of FT-IR was 4000–500 $cm^{-1}$, using KBr pellets at room temperature.

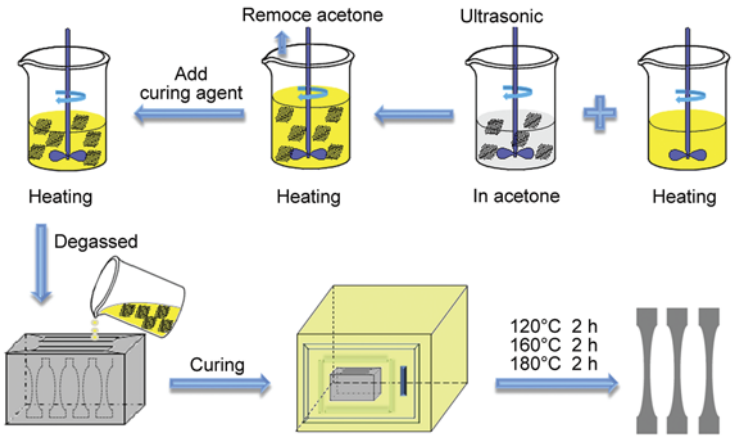


**Figure 2.** Preparation process of the epoxy composites

The wide angle X-ray diffraction (WAXD) measurements were carried out on a D8 ADVANCE X-ray diffractometer equipped with a computer controller. The scanning was performed from 5 to 50° with a speed of 2°/min.

The fracture surfaces of the specimens were investigated using field emission scanning electron microscopy (FE-SEM, JSM-6701F, Japan) at an accelerating voltage of 20 kV, and the fracture surfaces were coated with sputter-gold to improve the conductivity.

The liquid crystalline transitions and optical textures were made using a Leica DMxRP polarizing microscope with an INSTEC STC-200 hot stage. Small amounts of samples (2–3 mg) were pre-melted on a microscope slide then covered with a piece of cover glass to form a uniform thin film. The formation and development of the LC phase were examined under polarized light.

The surface functionalization of the GO was analyzed qualitatively by X-ray photoelectron spectroscopy (XPS) using a VG-microtech ESCA2000 spectrometer equipped with a hemispherical electron analyzer and a MgJa (hm = 1.2536 keV) X-ray source.

Thermogravimetric analysis (TGA) of the samples with 2~3 mg was conducted on NETZSCH STA-449 from 50 to 700°C at a heating rate of 10°C/min under $N_2$.

Differential scanning calorimetry (DSC-204, NETZSCH, Germany) was performed at temperature from 30 to 250°C at heating rate of 10°C/min. All tests were performed in a nitrogen atmosphere with a sample weight of about 8 mg.

Dynamic mechanical analysis (DMA) was performed on a DMA Q800 dynamic mechanical analyzer (TA Instruments, USA) to determine modulus and glass transition temperature ($T_g$). The tests were carried out in the single cantilever mode at a frequency of 1.0 Hz from 40 to 250°C at a heating rate of 3°C/min.

Mechanical properties of the composites were evaluated by impact, tensile and flexural measurements. Izod impact strength was measured on a tester of type XJJ-5, which is with no notch in the specimen according to National Standard of China (GB1043-79). The experiments were carried out on cubic samples (80 mm×10 mm×4 mm). The tensile strength was examined on a universal tensile tester of type RGT-5 according to National Standard of China (GB1040-92). The tensile rate was 2 mm/min. Flexural tests were performed according to WDW-20 (Shenzhen Jun Red Instrument Equipment Co., Ltd, China) using a three-point bending mode of the universal testing machine with a crosshead speed of 2 mm/min. The conditions of the tests and the specimens conformed to GB1449-2005. All the presented results are the average value of five specimens.

## 3. Results and discussion

In order to prove the grafting of TLCP on the surface of GO, FT-IR measurement was conducted. The FT-IR spectra of GO and TLCP-g-GO are presented in Figure 3. GO depicts a strong OH peak at 3406 $cm^{-1}$ [5, 24].The characteristic adsorption band corresponding to the C=O carbonyl stretching is 1732 $cm^{-1}$, and the C-O band is presented at 1053 $cm^{-1}$.The spectrum also shows a C=C peak at 1619 $cm^{-1}$ corresponding to the remaining $sp^2$ character [27, 28]. Comparing the spectra of TLCP-g-GO with that of GO, several new peaks are observed. Upon grafting, remarkably reduced hydroxyl absorption (3406 $cm^{-1}$) indicates a shielding effect of TLCP chains, and a sharp absorption peak appears at 1690 $cm^{-1}$ that can be attributed to the carbonyl stretching vibration of the esters in TLCP. The bands of 1255 and 1070 $cm^{-1}$ can be explained owing to the C–O–C symmetric and asymmetric stretching vibration. The band of 1160 $cm^{-1}$ is due to the C–O stretching vibration of the ester group in TLCP [29, 30]. The FT-IR curve affords support for covalent bonding at the interface.

TGA is a complementary technique that can reveal the composition and changes in thermal stability of the samples. As shown in Figure 4a, the samples

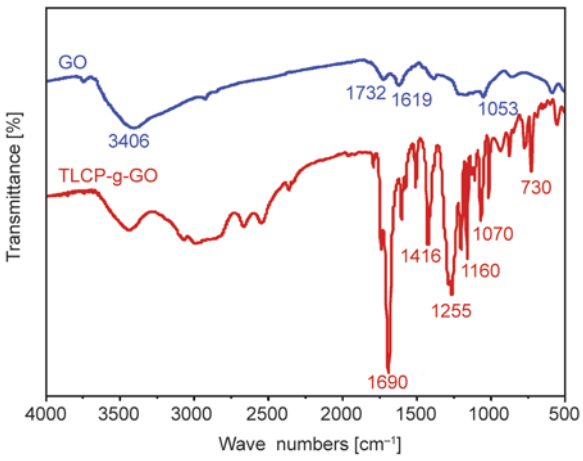


**Figure 3.** FT-IR spectra of GO and TLCP-g-GO

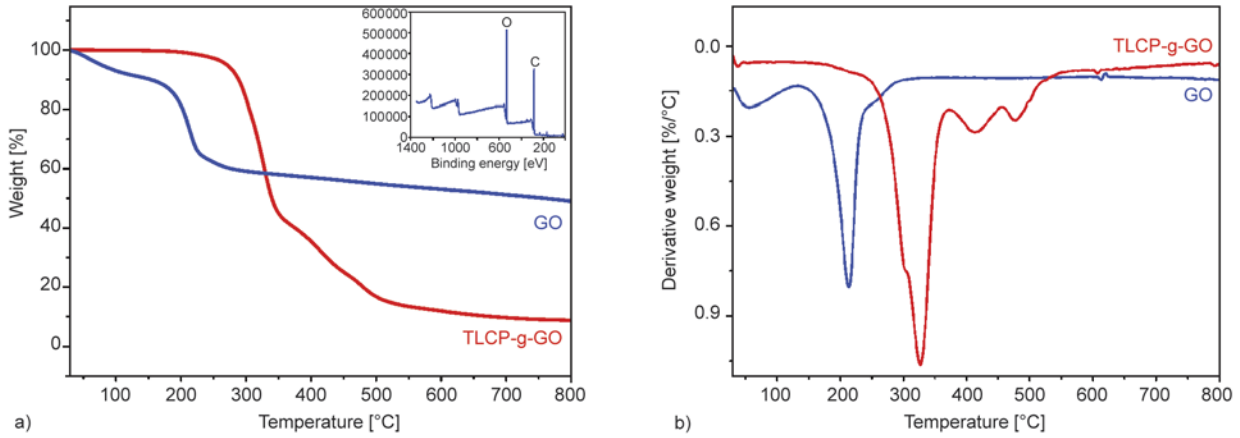


**Figure 4.** (a) TGA curves of GO and TLCP-g-GO, inset: XPS survey spectra of GO, (b) DTG curves of the GO and TLCP-g-GO

exhibit different thermal behavior. And the XPS survey spectra of GO was inserted in Figure 4a. As shown in the illustration, there are two peaks at 529 and 285 eV corresponding to the $O_{1s}$ and $C_{ls}$ binding energy of GO. The existence of O element is due to the oxygen-containing functional groups, which is in good agreement with FT-IR analysis. So pristine GO is not thermally stable, and mass loss starts even below 100°C and is rapidly at 150°C [13, 31], which are respectively attributed to evaporation of the remaining water and the decomposition of labile oxygen groups [32]. In contrast, the weight loss of TLCP-g-GO starts at 280°C, which is roughly 130°C higher than that of GO. And the weight retention at 800°C for TLCP-g-GO is about 10%. In addition, as can be seen from the DTG curves in Figure 4b, the maximum degradation temperature ($T_{max}$) of the GO also is slightly improved by grafting TLCP. The Tmax is observed at about 213°C for GO, and the GO-g-TLCP shifts the corresponding value to about 326°C, i.e. an evident increase of about 107°C. All of these indicate that the polymer is indeed attached onto the surface of GO sheets, and the polymer can improve the thermal stability of the GO.

The study by DSC and POM enables us to determine the transition temperatures. The DSC thermograms of TLCP-g-GO are shown in Figure 5. The DSC curves of TLCP-g-GO show a melting transition at 149°C and a nematic–isotropic phase transition at 248°C on heating, as well as displays an isotropic–nematic phase transition at 237°C and a crystallization process at 135°C on cooling. The POM results show that TLCP-g-GO exhibits liquid crystalline phase in the heating and cooling cycle. Furthermore, the phase transition temperatures observed by POM are consistent with the DSC

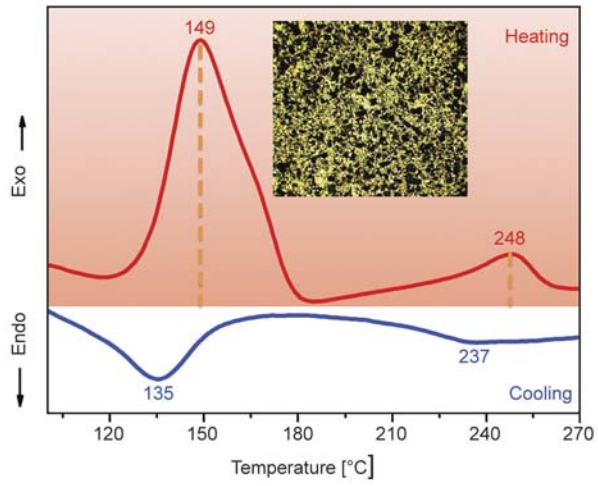


**Figure 5.** DSC curves of TLCP-g-GO, inset: POM figure of TLCP-g-GO at 200°C

determination results. The typical optical texture of TLCP-g-GO is shown in inset of Figure 5. It can be seen that the marbled texture of the nematic phase is found to appear between the two peaks in each process.

The wide-angle X-ray scattering patterns of TLCP-g-GO and GO are shown in Figure 6. It can be seen that GO spectra shows a strong peak at 9.14° and a weak, broad peak at 18.60°. However, the strong peak at 9.14° in the GO pattern is not present in the TLCP-g-GO pattern, indicating that TLCP cause the GO sheets to stack more loosely. At the same time, the curve for TLCP-g-GO shows a group of sharp diffraction peaks in the 2θ region of 15~30°, but no sharp peaks in the small-angle region appeared, suggesting no smectic layers [33]. All these results indicate that the TLCP-g-GO displays nematic mesophase. Meanwhile, the optical photographs of GO and TLCP-g-GO solution are shown in the inset of Figure 6. GO can be dispersed well in water due to

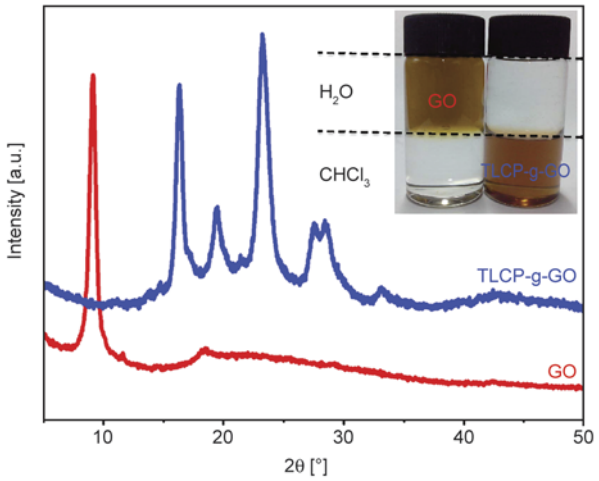


**Figure 6.** WAXD patterns of GO and TLCP-g-GO, inset: photographs of GO and TLCP-g-GO

the hydroxyl, carboxyl and epoxide groups on its surface. However the TLCP-g-GO only dispersed well in $CHCl_3$ solvent. The optical photographs provide more direct evidence to prove that thermotropic liquid crystalline epoxy is successfully grafted onto the surface of GO.

### 3.1. Morphological analysis of the composites

The morphologies of the fracture surfaces of the neat epoxy and its composites are presented in Figure 7. For each specimen, two types of micrographs are presented, one at a relatively low magnification (Figure 7a, 7c and 7e) and the other at a higher magnification (Figure 7b, 7d and 7f). As shown in Figure 7a and 7b, the fracture surface of the neat epoxy exhibits river patterns and very smooth. In addition, the cracks spread freely and randomly, revealing its nature of weak resistance to crack initiation and propagation [8, 34, 35]. Accordingly, the fracture process of neat epoxy is a typical brittle fracture pattern. On the contrary, the composites with TLCP-g-GO exhibit a rougher fracture surface (Figure 7c and 7e), and numerous tortuous and indentations and deep cracks can be observed. The large surface area and liquid crystalline groups significantly improve the interfacial adhesion between the filler and matrix, leading to plastic deformation when impacted. Figure 7d reveals that the filler randomly dispersed as a three dimension network through the polymer matrix rather than simply aligning parallel to the surface of the sample. Meanwhile, high embedding and tight binding with epoxy matrix, these further confirm that strong interfacial interaction between filler and epoxy resins. However, with the filler loading increasing, nanosheets exist in the form of agglomerates, as shown in Figure 7e and 7f. The agglomerates usually delaminate or slip by each other during the fracture process due to the weak adhesion between both the sheet/sheet and sheet/matrix [36].

### 3.2. Thermal properties

Figure 8 shows the change in $T_g$ for the neat epoxy and epoxy composites. Here the intermediate temperature is denoted as the glass transition temperature. It can be observed that the $T_g$ of neat epoxy is 174.9°C. Meanwhile, the $T_g$s shift to higher values with the addition of nanosheets into the epoxy matrix and the $T_g$ of composites increases by 15°C when TLCP-g-GO content is 1.5 wt%. This phenomenon is attributed to the following two factors. First, nanosheets confine polymer chains and reduce the chains mobility after introducing nanosheets into the matrix. It is believed that nanosheets can act as physical interlock points in the cured organic matrix, which generally not only provides a sterically hindered environment for curing reactions of composites, but also restrains the chain mobility [37]. Second, the matrix and chemical groups on the filler surface may participate in the curing reaction, leading to the higher crosslinking density.

Figure 9 shows the TGA and DTG curves for all the samples. It is apparently seen that all samples exhibit similar thermal behavior and only one-step decomposition, suggesting that the existence of nanosheets did not significantly alter the degradation mechanism of the epoxy matrix. The composites show a high thermal stability with decomposition temperatures ($T_d$) at 5% weight loss occurred greater than 345°C. The $T_d$ of epoxy increases from 345.4 to 381.2°C by addition of 1.0 wt% TLCP-g-GO. It is also noted the char yields of all composites are increased as compared to neat epoxy. Moreover, as can be seen from the DTG curves, the maximum degradation temperature ($T_{max}$) of the materials also is slightly improved by addition of the nanosheets. The $T_{max}$ is 18°C higher than that of the neat epoxy resin when filler content is 1.0 wt%, and the specific data of thermal decomposition are summarized in Table 1.The significant improvement of thermal stabilities can be attributed to the layered structure of the composite, which causes tortuous pathway for the volatile degradation products, thus delays the decomposition rate of the whole composites

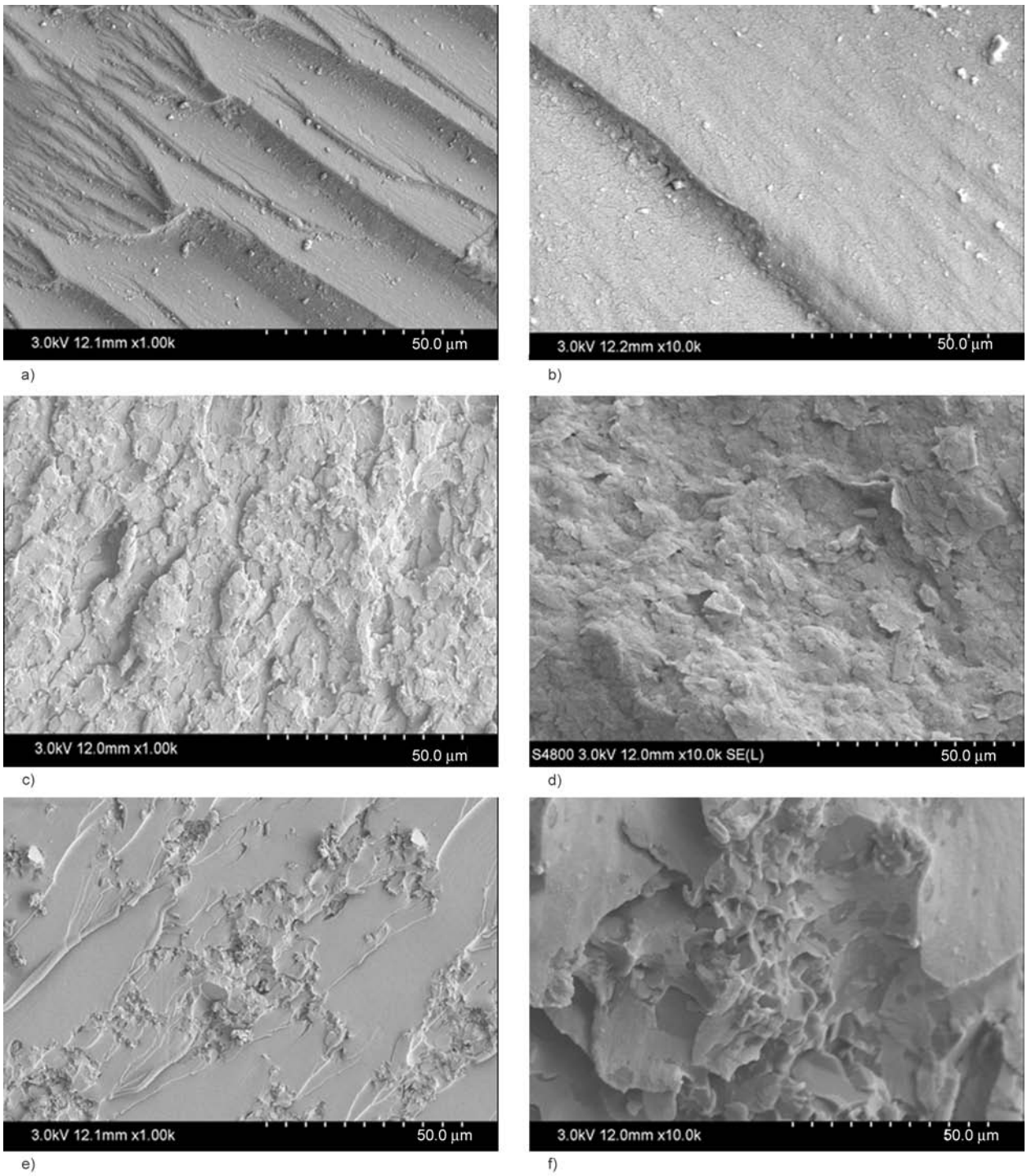


**Figure 7.** FE-SEM images of fracture surfaces of (a), (b) neat epoxy; (c), (d) 1.5 wt% epoxy; (e), (f) 3.0 wt% epoxy

**Table 1.** The initial decomposition temperatures (IDTs) and maximum degradation temperatures ($T_{max}$s) of composites

| TLCP-g-GO content [wt%] | Initialde composition temperatures (IDTs) [°C] | Maximum degradation temperatures ($T_{max}$s) [°C] |
|---|---|---|
| 0.0 | 345.4 | 400.1 |
| 0.5 | 371.5 | 407.7 |
| 1.0 | 381.2 | 418.1 |
| 1.5 | 376.9 | 415.5 |
| 2.0 | 376.0 | 412.8 |
| 3.0 | 372.3 | 408.6 |

[38, 39]. At the same time, the filler surface and the matrix take place crosslinking by curing reaction, which restrict thermal motion of the polymer molecular and also improve the thermal stability of the polymer.

Figure 10 shows the variations in storage modulus and tan δ as a function of temperature from below the glassy state temperature range to the rubbery plateau of neat epoxy and its composites. As shown in Figure 10a, the storage modulus of the materials

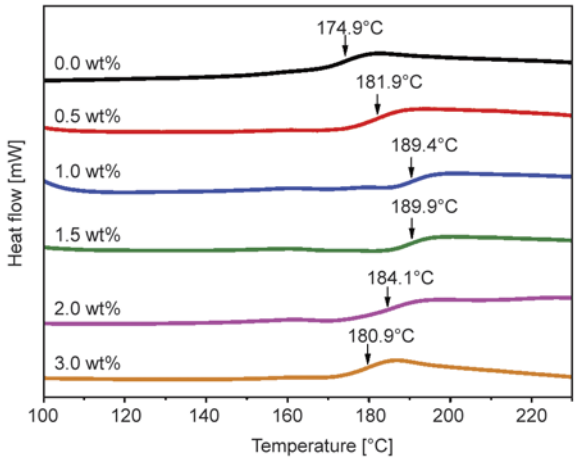


**Figure 8.** DSC curves of the cured neat epoxy and epoxy composites

was significantly increased by the addition of TLCP-g-GO fillers. It can be seen that below 150°C, the storage modulus of the composites is approximate to the neat epoxy. But in rubbery region, the storage moduli of the composites appears much higher than that of the neat epoxy. For instance, at 165°C the storage modulus was about 36% higher than neat epoxy resin when filler content is 1.5 wt%. This can be attributed to two reasons. Firstly, the filler effect mentioned earlier, namely filler can act as physical interlock points, which confine polymer chains and reduce the chains mobility [40]. Secondly, the LC domains also act as crosslink, tying segments of the polymer chain together [19]. They do not relax or become soft at higher temperature, and therefore the movements of the polymer chains are restricted by these rigid LC domains. Upon the incorporation of 2.0 wt% of TLCP-g-GO, however, the storage modulus decreases, probably because the particle loading exceeds the critical level. The excess TLCP-g-GO particles form agglomerates in the polymer matrix. The agglomerates affect the homogeneous dispersion of filler in polymer matrix, and reduce the crosslinking of composites.

The $T_g$ measured from the peak of the tan δ curve also shows that composites have higher $T_g$ compared to that of neat epoxy. As shown in Figure 10b, the $T_g$ of neat epoxy polymer was about 184.4°C. With the addition of 1.5 wt% TLCP-g-GO, the $T_g$ value increased to 198.9°C. Both of the filler effect and the crosslink effect are responsible for the high

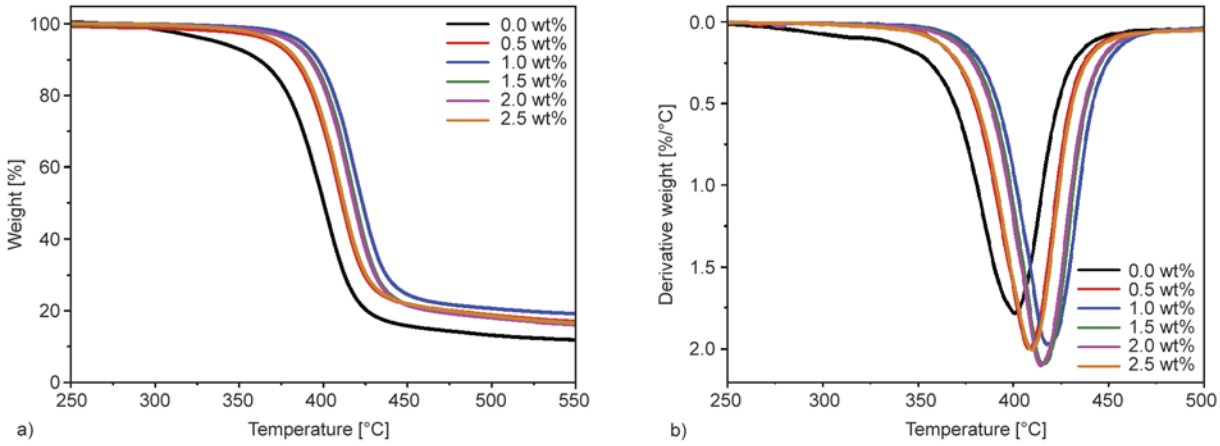


**Figure 9.** (a) TGA and (b) DTG curves of the neat epoxy and its composites

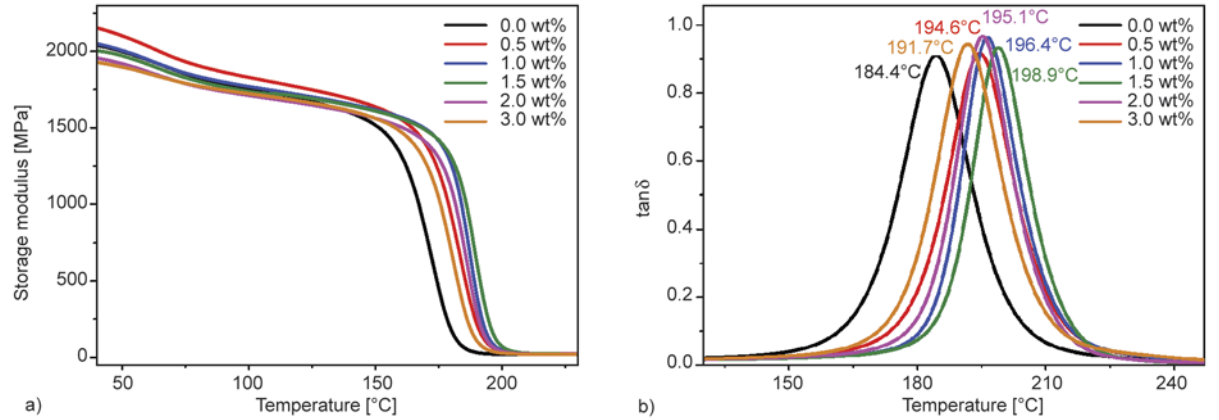


**Figure 10.** (a) Storage moduli and (b) tan δ as a function of temperature of the neat epoxy and its composites

$T_g$ observed in composites. The free volume of the composites is significantly reduced due to the presence of fillers, thereby decreasing the mobility of the segments in response to an applied thermal energy. While the dramatic drop in the $T_g$ at 2.0 wt% loading, which can be due to increased agglomeration sites within the composites. The agglomerates are physical imperfections in the epoxy composites, which hinder the curing of resin and lead to the low crosslinking density. The $T_g$ of the polymer was measured using DSC, which is in agreement with the DMA results. Although measured through different experimental technique, the composites always show higher $T_g$ than neat epoxy.

### 3.3. Mechanical properties of nanocomposites

Typical stress–strain curves of the epoxy composites obtained during tensile testing are shown in Figure 11. The tensile strength and elongation at break were varied with the filler contents [41]. As shown in Figure 11, the composites exhibit linear stress–strain character up to failure, without plastic deformation, and every specimen shows a similar curve shape [42]. The results also show an improvement in tensile strength and modulus of composites compared to neat epoxy for all concentrations of the filler. That is to say, the mechanical properties of composites get a high reinforcement by the dispersion of TLCP-g-GO in polymer matrix.

The variations of impact strength and tensile strength according to the filler contents are shown in Figure 12. Obviously, the impact strength and tensile strength of the composites are enhanced effectively with the addition of fillers. As seen in Figure 12, for neat epoxy impact strength and tensile strength are 26.25 kJ/m$^2$ and 55.43 MPa, respectively. With increasing concentration of TLCP-g-GO in the composite, impact strength and tensile strength first increase steeply, reach a plateau and decrease again at higher TLCP-g-GO loadings. The most significant improvement is obtained at a loading with 1.0 and 1.5 wt% TLCP-g-GO reaching 51.43 kJ/m$^2$ and 80.85 MPa, for impact strength and tensile strength respectively, which are increase of 96 and 46% compared to neat epoxy. This is attributed to the large surface area and multiple interactions between the functional groups of the filler and matrix in the composites [43, 44].

Figure 13 shows the flexural properties of the neat epoxy and its composites. The results show an improvement in strength and modulus of the composites compared to neat epoxy for all concentrations of TLCP-g-GO. A similar increasing tendency with TLCP-g-GO content is also found for the flexural strength. The composites with the flexural strength values ranging from 97.8 to 110.1 MPa, which are much higher than that of neat epoxy

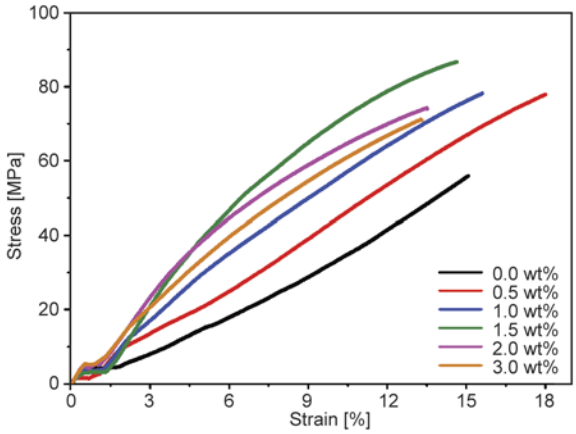


**Figure 11.** Typical stress-strain curves for the neat epoxy and its composites

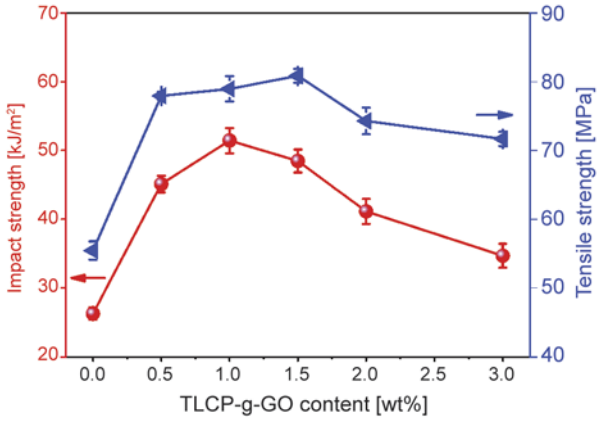


**Figure 12.** Impact strength and tensile strength of neat epoxy and epoxy composites

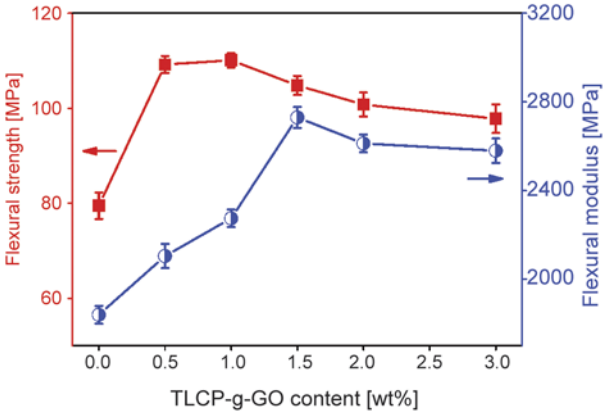


**Figure 13.** Flexural strength and modulus of neat epoxy and its composites

**Table 2.** The mechanical properties of neat epoxy and its composites

| TLCP-g-GO content [wt%] | Impact strength [kJ/m$^2$] | Tensile strength [MPa] | Flexural strength [MPa] | Flexural modulus [MPa] |
|---|---|---|---|---|
| 0.0 | 26.25±0.90 | 55.43±1.33 | 79.5±2.8 | 1840±40 |
| 0.5 | 45.12±1.21 | 77.95±0.55 | 109.2±1.8 | 2105±55 |
| 1.0 | 51.43±1.85 | 78.96±0.86 | 110.1±1.5 | 2275±41 |
| 1.5 | 48.46±1.67 | 80.85±1.01 | 104.8±2.0 | 2730±48 |
| 2.0 | 41.12±1.82 | 74.29±1.95 | 100.8±2.5 | 2613±40 |
| 3.0 | 34.67±1.74 | 71.76±1.04 | 97.8±3.0 | 2580±55 |

(79.5 MPa).The maximum improvement in flexural strength is observed at the 1.0 wt% filler content. The improved flexural strength is attributed to following reasons. Graphene oxide has large surface area, which can serve as connecting bridges to prevent the matrix from fracturing upon mechanical deformation. In addition, liquid crystalline groups have certain rigidity, and it can also improve the properties of epoxy composites. However, as the filler concentration exceeded 1.0 wt%, the flexural strength of the composites decreased suddenly, probably because the particle loading exceeds the critical level, called mechanical percolation [45]. The excess particles may form agglomerates in the polymer matrix, and lead to cracks to initiate and propagate easily, consequently, produce the reduced strength of the composites [36].The modulus of the composites increases steadily with the incorporation of the fillers to 1.5 wt% of TLCP-g-GO, the maximum improvement is 890 MPa. Beyond this concentration, the modulus decreased. Nevertheless, it remained still above that of the neat epoxy. This phenomenon is possibly because the addition of TLCP-g-GO caused a dilution effect in the matrix, i.e. the volume fraction of epoxy resin matrix decreased with increasing filler loading, which would lead to a decrease of crosslinking of composites. In addition, the filler agglomerates in the epoxy composites can delaminate or slip by each other during the external role process due to the weak adhesion between both the sheet/sheet and sheet/matrix.

In general, a significant improvement in the mechanical properties is attributed to the strong interaction between TLCP-g-GO and epoxy matrix, so that the efficient load transfer between nanosheets and the epoxy matrix [46, 47]. Moreover, the nanosheets may serve as connecting bridges to prevent the matrix from fracturing upon mechanical deformation, thus enhancing the mechanical properties of epoxy. Another reason may be that, during the casting process, the nanosheets are inclined to lay flat and oriented along the flow of epoxy resin direction, which is beneficial for the efficient stress transfer and thus reinforcing the mechanical properties of composites [48, 49]. Table 2 summarizes the mechanical properties data.

## 4. Conclusions

In this paper, we prepared high performance TLCP-g-GO/epoxy composites with good thermal properties, high strength and high modulus. By thermotropic liquid crystalline epoxy modified GO ensured excellent dispersity and good compatibility in the polymer matrix. The composites showed a high reinforcing efficiency, which attributed to the special two dimensional morphology of GO and the functionalized surface of GO providing well dispersion, high contact area in matrix. The composites exhibit around a 96% increase in impact strength, 46% improvement in tensile strength, and 48% reinforce in flexural modulus for a low filler content (1.0 or 1.5 wt%). Meanwhile, with the incorporation of 1.5 wt% of TLCP-g-GO, the $T_g$ of composites increases by 15°C. The decomposition temperature ($T_d$) at 5% weight loss is 35.8°C higher than that of the neat epoxy resin. In short, we provide a promising approach to prepare graphene based composites with enhanced performances.

## Acknowledgements

The authors gratefully acknowledge the financial support by National Natural Science Foundation of China (51163004 and 51303034), the Natural Science Foundation of Guangxi Province, China (No.2013GXNSFAA019308), the Opening Funding of Guangxi Key Laboratory for Advance Materials and New Preparation Technology (12KF-8), Innovation Team of Guangxi Universities' Talent Highland and Guangxi Funds for Specially-appointed Expert.

## References


[1] Kim J., Yim B-S., Kim J-M., Kim J.: The effects of functionalized graphene nanosheets on the thermal and mechanical properties of epoxy composites for anisotropic conductive adhesives (ACAs). Microelectronics Reliability, **52**, 595–602 (2012). DOI: 10.1016/j.microrel.2011.11.002

[2] Jiao J., Sun X., Pinnavaia T. J.: Mesostructured silica for the reinforcement and toughening of rubbery and glassy epoxy polymers. Polymer, **50**, 983–989 (2009). DOI: 10.1016/j.polymer.2008.12.042

[3] Shen X-J., Pei X-Q., Fu S-Y., Friedrich K.: Significantly modified tribological performance of epoxy nanocomposites at very low graphene oxide content. Polymer, **54**, 1234–1242 (2013). DOI: 10.1016/j.polymer.2012.12.064

[4] Shen X-J., Pei X-Q., Liu Y., Fu S-Y.: Tribological performance of carbon nanotube–graphene oxide hybrid/epoxy composites. Composites Part B: Engineering, **57**, 120–125 (2014). DOI: 10.1016/j.compositesb.2013.09.050

[5] Jiang T., Kuila T., Kim N. H., Ku B-C., Lee J. H.: Enhanced mechanical properties of silanized silica nanoparticle attached graphene oxide/epoxy composites. Composites Science and Technology, **79**, 115–125 (2013). DOI: 10.1016/j.compscitech.2013.02.018

[6] Deng S. H., Zhou X. D., Zhu M. Q., Fan C. J., Lin Q. F.: Interfacial toughening and consequent improvement in fracture toughness of carbon fiber reinforced epoxy resin composites: Induced by diblock copolymers. Express Polymer Letters, **7**, 925–935 (2013). DOI: 10.3144/expresspolymlett.2013.90

[7] Chen J., Taylor A. C.: Epoxy modified with triblock copolymers: Morphology, mechanical properties and fracture mechanisms. Journal of Materials Science, **47**, 4546–4560 (2012). DOI: 10.1007/s10853-012-6313-6

[8] Tang L-C., Zhang H., Sprenger S., Ye L., Zhang Z.: Fracture mechanisms of epoxy-based ternary composites filled with rigid-soft particles. Composites Science and Technology, **72**, 558–565 (2012). DOI: 10.1016/j.compscitech.2011.12.015

[9] Lu S-R., Jiang Y-M., Wei C.: Preparation and characterization of EP/$SiO_2$ hybrid materials containing PEG flexible chain. Journal of Materials Science, **44**, 4047–4055 (2009). DOI: 10.1007/s10853-009-3584-7

[10] Johnsen B. B., Kinloch A. J., Mohammed R. D., Taylor A. C., Sprenger S.: Toughening mechanisms of nanoparticle-modified epoxy polymers. Polymer, **48**, 530–541 (2007). DOI: 10.1016/j.polymer.2006.11.038

[11] Shen X-J., Liu Y., Xiao H-M., Feng Q-P., Yu Z-Z., Fu S-Y.: The reinforcing effect of graphene nanosheets on the cryogenic mechanical properties of epoxy resins. Composites Science and Technology, **72**, 1581–1587 (2012). DOI: 10.1016/j.compscitech.2012.06.021

[12] Hou S., Su S., Kasner M. L., Shah P., Patel K., Madarang C. J.: Formation of highly stable dispersions of silane-functionalized reduced graphene oxide. Chemical Physics Letters, **501**, 68–74 (2010). DOI: 10.1016/j.cplett.2010.10.051

[13] Yang Y., Wang J., Zhang J., Liu J., Yang X., Zhao H.: Exfoliated graphite oxide decorated by PDMAEMA chains and polymer particles. Langmuir, **25**, 11808–11814 (2009). DOI: 10.1021/la901441p

[14] Shen J., Hu Y., Li C., Qin C., Ye M.: Synthesis of amphiphilic graphene nanoplatelets. Small, **5**, 82–85 (2009). DOI: 10.1002/smll.200800988

[15] Chen G., Zhai S., Zhai Y., Zhang K., Yue Q., Wang L., Zhao J., Wang H., Liu J., Jia J.: Preparation of sulfonic-functionalized graphene oxide as ion-exchange material and its application into electrochemiluminescence analysis. Biosensors and Bioelectronics, **26**, 3136–3141 (2011). DOI: 10.1016/j.bios.2010.12.015

[16] Meng F-B., Cui Y., Chen H-B., Zhang B-Y., Jia C.: Phase behaviors of comb-like liquid crystalline polysiloxanes containing fluorinated mesogenic units. Polymer, **50**, 1187–1196 (2009). DOI: 10.1016/j.polymer.2009.01.005

[17] Jannesari A., Ghaffarian S. R., Mohammadi N., Taromi F. A., Molaei A.: Liquid crystalline thermosets as binder for powder coatings: Thermoanalytical study of the cure characteristics of a carboxylated main chain liquid crystalline oligoester. Progress in Organic Coatings, **50**, 213–223 (2004). DOI: 10.1016/j.porgcoat.2004.02.006

[18] Mija A., Navard P., Peiti C., Babor D., Guigo N.: Shear induced structuration of liquid crystalline epoxy thermosets. European Polymer Journal, **46**, 1380–1387 (2010). DOI: 10.1016/j.eurpolymj.2010.04.001

[19] Li Y., Badrinarayanan P., Kessler M. R.: Liquid crystalline epoxy resin based on biphenyl mesogen: Thermal characterization. Polymer, **54**, 3017–3025 (2013). DOI: 10.1016/j.polymer.2013.03.043

[20] Mormann W., Bröcher M.: Liquid crystalline thermosets by polymerization of mesogenic azomethine based diepoxides-influence of reaction rate on phase behaviour. Polymer, **40**, 193–198 (1999). DOI: 10.1016/s0032-3861(98)00211-0

[21] Jaisankar S. N., Nelson D. J., Brammer C. N.: New synthesis and characterization of ionic polyurethane-urea liquid crystals. Polymer, **50**, 4775–4780 (2009).
DOI: 10.1016/j.polymer.2009.07.049

[22] Hsu S-H., Wu M-C., Chen S., Chuang C-M., Lin S-H., Su W-F.: Synthesis, morphology and physical properties of multi-walled carbon nanotube/biphenyl liquid crystalline epoxy composites. Carbon, **50**, 896–905 (2012).
DOI: 10.1016/j.carbon.2011.09.051

[23] Iqbal M., Dingemans J. T.: High $T_g$ nematic thermosets: Synthesis, characterization and thermo-mechanical properties. European Polymer Journal, **46**, 2174–2180 (2010).
DOI: 10.1016/j.eurpolymj.2010.08.010

[24] Ren L., Wang X., Guo S., Liu T.: Functionalization of thermally reduced graphene by *in situ* atom transfer radical polymerization. Journal of Nanoparticle Research, **13**, 6389–6396 (2011).
DOI: 10.1007/s11051-011-0391-2

[25] Guo J., Zhu S., Chen Z., Li Y., Yu Z., Liu Q., Li J., Feng C., Zhang D.: Sonochemical synthesis of $TiO_2$ nanoparticles on graphene for use as photocatalyst. Ultrasonics Sonochemistry, **18**, 1082–1090 (2011).
DOI: 10.1016/j.ultsonch.2011.03.021

[26] Akhavan O.: The effect of heat treatment on formation of graphene thin films from graphene oxide nanosheets. Carbon, **48**, 509–519 (2010).
DOI: 10.1016/j.carbon.2009.09.069

[27] Song S. H., Park K. H., Kim B. H., Choi Y. W., Jun G. H., Lee D. J., Kong B-S., Paik K-W., Jeon S.: Enhanced thermal conductivity of epoxy–graphene composites by using non-oxidized graphene flakes with non-covalent functionalization. Advanced Materials, **25**, 732–737 (2013).
DOI: 10.1002/adma.201202736

[28] Gudarzi M. M., Sharif F.: Enhancement of dispersion and bonding of graphene-polymer through wet transfer of functionalized graphene oxide. Express Polymer Letters, **6**, 1017–1031 (2012).
DOI: 10.3144/expresspolymlett.2012.107

[29] Wang J-W., Zhang B-Y.: Effect of fluorinated nematic mesogens on phase behaviors and optical properties of chiral liquid crystalline polysiloxanes. Colloid and Polymer Science, **291**, 2917–2925 (2013).
DOI: 10.1007/s00396-013-3049-z

[30] Meng F-B., Zhou N-Y., Du C., Gao H-M., He X-Z.: Synthesis, characterization and electrorheological effect of sulfosalt-type liquid-crystalline ionomers containing polyaniline units. Journal of Applied Polymer Science, **130**, 3395–3403 (2013).
DOI: 10.1002/app.39593

[31] Qiu S. L., Wang C. S., Wang Y. T., Liu C. G., Chen X. Y., Xie H. F., Huang Y. A., Cheng R. S.: Effects of graphene oxides on the cure behaviors of a tetrafunctional epoxy resin. Express Polymer Letters, **5**, 809–818 (2011).
DOI: 10.3144/expresspolymlett.2011.79

[32] Fang M., Wang K., Lu H., Yang Y., Nutt S.: Covalent polymer functionalization of graphene nanosheets and mechanical properties of composites. Journal of Materials Chemistry, **19**, 7098–7105 (2009).
DOI: 10.1039/b908220d

[33] Liu J-H., Hsieh F-M.: Synthesis and characterization of novel liquid crystalline polymers containing cholesteryl pendant groups. Materials Chemistry and Physics, **118**, 506–512 (2009).
DOI: 10.1016/j.matchemphys.2009.08.031

[34] Ai L., Zhang C., Chen Z.: Removal of methylene blue from aqueous solution by a solvothermal-synthesized graphene/magnetite composite. Journal of Hazardous Materials, **192**, 1515–1524 (2011).
DOI: 10.1016/j.jhazmat.2011.06.068

[35] Wang S., Tambraparni M., Qiu J., Tipton J., Dean D.: Thermal expansion of graphene composites. Macromolecules, **42**, 5251–5255 (2009).
DOI: 10.1021/ma900631c

[36] Tang L-C., Wan Y-J., Yan D., Pei Y-B., Zhao L., Li Y-B., Wu L-B., Jiang J-X., Lai G-Q.: The effect of graphene dispersion on the mechanical properties of graphene/epoxy composites. Carbon, **60**, 16–27 (2013).
DOI: 10.1016/j.carbon.2013.03.050

[37] Yu J., Huang X., Wu C., Wu X., Wang G., Jiang P.: Interfacial modification of boron nitride nanoplatelets for epoxy composites with improved thermal properties. Polymer, **53**, 471–480 (2012).
DOI: 10.1016/j.polymer.2011.12.040

[38] Wu X., Wang Y., Xie L., Yu J., Liu F., Jiang P.: Thermal and electrical properties of epoxy composites at high alumina loadings and various temperatures. Iranian Polymer Journal, **22**, 61–73 (2013).
DOI: 10.1007/s13726-012-0104-4

[39] Lu S., Li S., Yu J., Yuan Z., Qi B.: Epoxy nanocomposites filled with thermotropic liquid crystalline epoxy grafted graphene oxide. RSC Advances, **3**, 8915–8923 (2013).
DOI: 10.1039/c3ra40404h

[40] Sridhar V., Lee I., Chun H. H., Park H.: Graphene reinforced biodegradable poly(3-hydroxybutyrate-*co*-4-hydroxybutyrate) nano-composites. Express Polymer Letters, **7**, 320–328 (2013).
DOI: 10.3144/expresspolymlett.2013.29

[41] Feng Q-P., Shen X-J., Yang J-P., Fu S-Y., Mai Y-W., Friedrich K.: Synthesis of epoxy composites with high carbon nanotube loading and effects of tubular and wavy morphology on composite strength and modulus. Polymer, **52**, 6037–6045 (2011).
DOI: 10.1016/j.polymer.2011.10.049

[42] Yuan X. Y., Zou L. L., Liao C. C., Dai J. W.: Improved properties of chemically modified graphene/poly(methyl methacrylate) nanocomposites *via* a facile *in-situ* bulk polymerization. Express Polymer Letters, **6**, 847–858 (2012).
DOI: 10.3144/expresspolymlett.2012.90

[43] Zhao Y., Chen Z-K., Liu Y., Xiao H-M., Feng Q-P., Fu S-Y.: Simultaneously enhanced cryogenic tensile strength and fracture toughness of epoxy resins by carboxylic nitrile-butadiene nano-rubber. Composites Part A: Applied Science and Manufacturing, **55**, 178–187 (2013).
DOI: 10.1016/j.compositesa.2013.09.005

[44] Chatterjee S., Wang J. W., Kuo W. S., Tai N. H., Salzmann C., Li W. L., Hollertz R., Nüesch F. A., Chu B. T. T.: Mechanical reinforcement and thermal conductivity in expanded graphene nanoplatelets reinforced epoxy composites. Chemical Physics Letters, **531**, 6–10 (2012).
DOI: 10.1016/j.cplett.2012.02.006

[45] Dong J., Yin C., Zhao X., Li Y., Zhang Q.: High strength polyimide fibers with functionalized graphene. Polymer, **54**, 6415–6424 (2013).
DOI: 10.1016/j.polymer.2013.09.035

[46] Li Y., Umer R., Samad Y. A., Zheng L., Liao K.: The effect of the ultrasonication pre-treatment of graphene oxide (GO) on the mechanical properties of GO/polyvinyl alcohol composites. Carbon, **55**, 321–327 (2013).
DOI: 10.1016/j.carbon.2012.12.071

[47] Li Y., Pan D., Chen S., Wang Q., Pan G., Wang T.: *In situ* polymerization and mechanical, thermal properties of polyurethane/graphene oxide/epoxy nanocomposites. Materials and Design, **47**, 850–856 (2013).
DOI: 10.1016/j.matdes.2012.12.077

[48] Lv S. H., Ma Y. J., Qiu C. C., Sun T., Liu J. J., Zhou Q. F.: Effect of graphene oxide nanosheets of microstructure and mechanical properties of cement composites. Construction and Building Materials, **49**, 121–127 (2013).
DOI: 10.1016/j.conbuildmat.2013.08.022

[49] Satti A., Larpent P., Gun'ko Y.: Improvement of mechanical properties of graphene oxide/poly(allylamine) composites by chemical crosslinking. Carbon, **48**, 3376–3381 (2010).
DOI: 10.1016/j.carbon.2010.05.030

*eXPRESS Polymer Letters Vol.8, No.7 (2014) 480–490*
*Available online at www.expresspolymlett.com*
*DOI: 10.3144/expresspolymlett.2014.52*

# A novel synthesis of 4-toluene 9*H*-carbazole-9-carbodithioate, electropolymerization and impedance study

*M. Ates*[1*], *N. Uludag*[1], *T. Karazehir*[1,2], *F. Arican*[1]

[1]Department of Chemistry, Faculty of Arts and Sciences, Namik Kemal University, Degirmenalti Campus, 59030 Tekirdag, Turkey
[2]Department of Chemistry, Faculty of Arts and Sciences, Istanbul Technical University, Maslak, Istanbul, Turkey

*Received 5 January 2014; accepted in revised form 8 March 2014*

**Abstract.** A novel synthesis of 4-toluene 9*H*-carbazole-9-carbodithioate (TCzC) was chemically synthesized and characterized by Fourier Transform Infrared (FTIR), proton nuclear magnetic resonance ($^1$H-NMR), and carbon nuclear magnetic resonance ($^{13}$C-NMR) spectroscopies. Specific ($C_{sp}$) and double layer capacitances ($C_{dl}$) of the electro-coated poly(carbazole) and poly(TCzC) films were obtained on glassy carbon electrode (GCE) by impedimetric method with DC potential from –0.1 to +1.0 V by increasing potential of 0.2 V. The polymers were characterized by Cyclic voltammetry (CV), Fourier transform infrared reflectance-attenuated total reflection spectroscopy (FTIR-ATR), Atomic force microscopy (AFM), and Electrochemical impedance spectroscopy (EIS). The use of additional variable (DC potential) helped to disambiguate the equivalent circuit model of $R(C(R(Q(RW))))(CR)$. Simulation results were compared with experimental data. In this study, substituted group effects of $CS_2$ and tosyl on carbazole polymer were investigated by EIS technique. $CS_2$ group together with tosyl group in the structure of carbazole decreased the specific capacitance value ($C_{sp}$ = 0.43 mF·cm$^{-2}$) compared to PCz ($C_{sp}$ = 1.44 mF·cm$^{-2}$). Electropolymerization formation was seriously affected by substituted groups of $CS_2$ and tosyl on conjugation system because of the electron donor and acceptor ability.

***Keywords:*** *coatings, functional polymer, electrochemical impedance spectroscopy, electropolymerization, conducting polymer*

## 1. Introduction

Among conducting polymers, polycarbazoles are known for their good electro-activity [1, 2] and thermal [3–5], electrical [6], photo-physical [7], and electrochromic properties [8]. They have been suggested for a number of applications, such as electroluminescent devices [9], sensors [10, 11], redox catalysts [12], and electrochromic displays [13]. The functional groups, such as amino, imino and sulfonic groups have been performed for achieving new polymers which meet the criteria of commercial applications [14–16]. There are many novel syntheses of functional polycarbazole papers. 3,6-bis (2,3-dihydrothieno [3,4-b][1,4] dioxin-5-yl)-9-tosyl-9*H*-carbazole [17], 5-(3,6-Dibromo-9*H*-carbazole-9-yl)-pentane nitrile [18], 9-tosyl-9*H*-carbazole [19], 9-tosyl-9*H*-carbazole-co-pyrrole [20], *N*-(1,4-Dimethyl-9*H*-carbazole-3-ylmethyl)-*N*-tosyl aminoacetaldehyde diethyl acetal [21], ethyl 4-hydroxy-9-tosyl-9*H*-carbazole-3-carboxylate [22], 4-[2-carbazole-3-yl) vinyl] pyridium tosylate [23], *N*-(o-ethynyl)phenylynamides and arylynamides [24] and 9-(4-nitrophenylsulfonyl)-9*H*-carbazole [25] were given in literature. The synthesis was per-

*Corresponding author, e-mail: mates@nku.edu.tr

formed especially with donor-acceptor group, which supported electron rich and poor region on the polymer skeleton [26].

Electrochemical impedance spectroscopy (EIS) is one of the most frequently used analytical tools for the characterization of capacitors or supercapacitors [27]. EIS is used to explain behavior of modified electrodes explaining two models, which are known as uniform [28] and porous medium [29]. In this study, porous medium was evaluated by EIS. At present, the electrode materials for supercapacitors have been widely investigated especially for carbon materials such as activated carbons, the mostly widely used electrode materials due to their large surface area, relatively good electrical properties and moderate cost [30–32]. Among the carbon materials, carbon nanotubes (CNT) are considered to be potential candidates as the electrodes in supercapacitor, due to their high accessible surface, chemical stability, excellent mechanical properties, good electrical conductivity, and unique pore structure [33, 34]. The other electrode materials such as transition metal oxides and conducting polymer [35, 36] are being widely investigated to improve the specific capacitance and the energy density of supercapacitor [37, 38].

Herein, in this study, we principally synthesized $CS_2$ and tosyl group of substituent of carbazole monomer and compare the effects of these functional groups on EIS properties. Also we investigated the equivalent circuit model of $R(C(R(Q(RW))))(CR)$ with Kramers-Kronig transform to fit the experimental and theoretical data. As a result, this paper presents a new approach of circuit Modeling and capacitive behavior of a novel polymer synthesis by using EIS technique.

## 2. Experimental

### 2.1. Materials

Carbazole (Alfa Aesar, USA), sodium hydroxide (NaOH), carbon disulfide (Aldrich, USA), p-toluensulfonyl chloride (Aldrich, USA) were received without further purification. Dichloromethane ($CH_2Cl_2$), dimethylsulfoxide (DMSO), diethyl ether, acetonitrile ($CH_3CN$), tetraethylammonium tetrafluoroborate ($TEABF_4$) were supplied from Merck Chemical Co. (Germany) and they were used as received. Silica gel, used for synthesis experiments, was described as an efficient and reusable catalyst.

### 2.2. Electrochemical tests

Cyclic voltammetry (CV) was performed by using PARSTAT 2273, USA (software: powersuit and Faraday cage: BASI Cell Stand C3, West Lafayette, Indiana, USA) in a three electrode configuration, which employed glassy carbon electrode (GCE) (area: 0.07 $cm^2$) as the working electrode, platinum wire as the counter electrode and Ag/AgCl (3.5 M) as the reference electrode. All electrochemical experiments were carried out at 20±1°C.

### 2.3. Structure characterization

Modified carbon fiber microelectrode (CFME) was characterized by Fourier transform infrared- attenuated total reflection (FTIR-ATR) spectroscopy (Perkin Elmer, Spectrum One B, with an universal ATR sampling accessory (4000–550 $cm^{-1}$) with a diamond and ZnSe crystal, USA). The Atomic force microscopy (AFM) images were obtained with Park System XE100 Suwon, Korea. In all AFM analysis, the non-contact mode was employed by using Al coated high resonance frequency silicon tips (265–400 kHz) with 4 μm thickness, 35 μm mean width, 125 μm length and 20–75 N/m force constant. High resolution images (1024×1024 pixels) and the raw data were collected by the XEI image. Melting point was determined in a capillary tube on Electro thermal IA 9000 apparatus and uncorrected (Stone Staffordshire, UK). Mass spectra were determined by means of Agilent 5973 model of GC-MS (Santa Clara, CA, USA).

### 2.4. Electrochemical impedance spectroscopy and modeling

Electrochemical impedance spectroscopic (EIS) measurements were performed for Cz and TCzC in the initial molar concentration of 3.0 mM in 0.1 M tetraethylammonium tetrafluoroborate ($TEABF_4$)/ dichloromethane ($CH_2Cl_2$) – acetonitrile ($CH_3CN$) volume ratio of (8:2). EIS measurements were done in monomer-free electrolyte solution with perturbation amplitude of 10 mV and DC potential from –0.1 to +1.0 V on glassy carbon electrode (GCE) over a frequency range of 0.01 Hz to 100 kHz with PARSTAT 2273 model Potansiostat/galvanostat. All measurements began at the open circuit potential, modified polymer films were allowed to equilibrate for ~10 min at each potential before being measured. The equivalent circuit model of $R(C(R(Q(RW))))(CR)$

was taken by Kramers-Kronig Transform (ZSimpwin programme).

## 3. Results and discussion

### 3.1. Synthesis procedure

A suspension of NaOH (1.2 g, 30 mmoles) in dimethylsulfoxide (DMSO, 150 mmoles) was prepared. Afterwards, carbazole (5 g, 29.9 mmoles) was added under vigorous stirring. The reaction mixture was stirred for 2 hours at room temperature. Carbondisulfide (2.2 g, 30 mmoles) was added dropwise into the mixture, and the resultant reddish solution was stirred for 4 hours at room temperature, and then by adding slowly p-toluensulfonylchloride (5.7 g, 30 mmoles) in DMSO (30 mL). The final mixture was stirred for a night. The resultant reaction mixture which was poured into large amount of water and yellow solid was obtained by filtration. The crude product was purified by silica gel chromatography and crystallised from diethyl ether. The resultant mass was 6.5 g. 4-toluene 9*H*-carbazole-9-carbodithioate (yield: 59%) was obtained at the melting temperature of 194°C and molecular weight of 337.53 g/mol obtained by coupled gas chromatorgpahy and mass spectrometry (GC-MS) (Figure 1).

As a basis for the synthetic approaches to 4-toluene-9*H*-carbazole-9-carbodithioate was synthesized from carbazole by using similar methods given in the literatures [39, 40]. The spectra of dithiocarbamates obtained were identical to those of the produced in the above literatures.

C=S bond on $CS_2$ group connected with carbazole and electron pair on nitrogen atom showed a resonance structure and formed an active side with positive (+) charges on the carbazole structure of 3 and 6 position. An easy polymer formation was supplied by cationic polymerization with conjugation system. Polymerization formation was crucially affected by substituted groups on conjugation system due to electron donor and acceptor groups as shown in Figure 2.

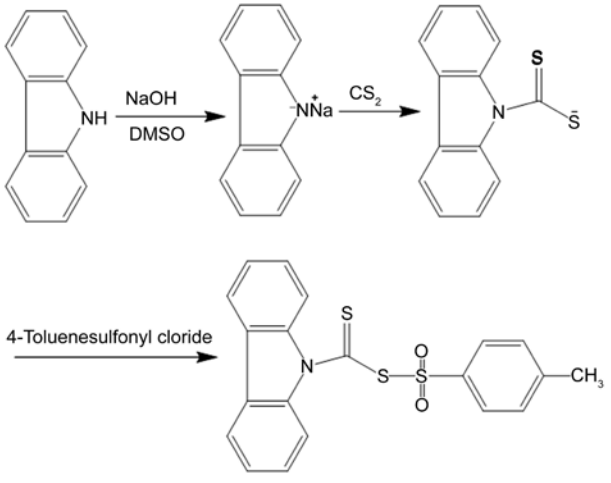


**Figure 1.** Synthesis procedure of 4-toluene 9*H*-carbazole-9-carbodithioate

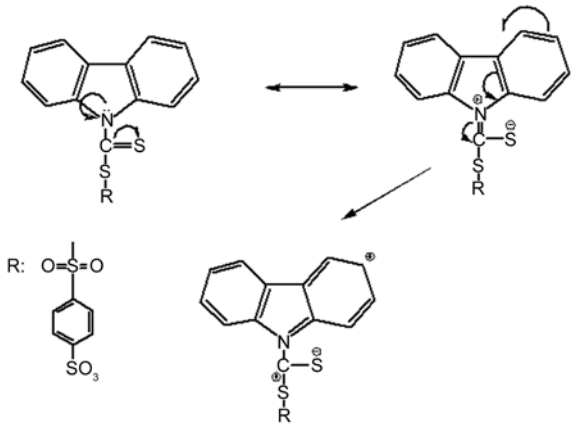


**Figure 2.** Resonance formation of 4-toluene 9*H*-carbazole-9-carbodithioate

Carbazole was treated with NaOH and carbondisulfide in the presence of DMSO then added 4-methyl benzene-1-sulfonylchloride to obtain 4-toluene-9*H*-carbazole-9-carbodithioate (59% yield). 4-toluene-9*H*-carbazole-9-carbodithioate was determined by FTIR, $^{1}$NMR, and $^{13}$C-NMR.

### 3.2. Characterisation of 4-toluene 9*H*-carbazole-9-carbodithioate monomer

FT-IR analysis (potassium bromide): ν3058 $cm^{-1}$ (aromatic C–H), 1593 $cm^{-1}$ (aromatic C=C), 1487 $cm^{-1}$ (aromatic C=C), 1435 $cm^{-1}$ (aromatic C=C). The peak of N–H at 3000–3500 $cm^{-1}$ was not observed in the FTIR spectrum. It proved the insertion of the $CS_2$ group into the carbazole structure as shown in Figure 3.

$^{1}$H-NMR (deuterochloroform) spectrum of TCzC: δ 2.31 (s, $CH_3$), 7.07–7.12 (d, 2H, aromatic C–H), 7.25–7.33 (d, 2H, aromatic C–H ), 7.35–7.41 (m, 2H, aromatic C–H ), 7.46–7.90 (m, 2H, aromatic C–H), 8.31–8.34 (d, 2H, aromatic C;H). 4-toluene-9*H*-carbazole-9-carbodithioate was determined by NMR experiments and FT-IR spectroscopy. The most characteristic value of it $^{1}$H-NMR spectrum was a singlet of methyl proton peaks at 2.31 ppm, as well as between 7.07–7.90 ppm aromatic protons.

$^{1}$H-NMR (deuterochloroform) spectrum of Cz: δ 7.21–7.25 (m, 4H, aromatic CH), 7.39–7.51 (m, 4H,

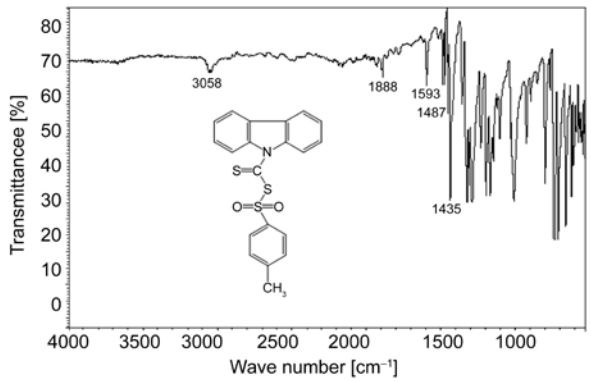


**Figure 3.** FTIR spectrum of 4-toluene 9*H*-carbazole-9-carbodithioate

aromatic CH), 8.09 (s, 1H, NH). $^1$H-NMR peak difference between Cz and TCzC can be easily obtained as shown in Figure 4.

$^{13}$C NMR (deuterochloroform): δ 194.85; 139.85; 127.11; 126.14; 124.27; 120.37; 115.38; 77.34; 77.22; 77.02; 76.70. Analytically calculated for $C_{20}H_{15}NO_2S_3$ (397.53 g/mol) : C (71.01); H (4.72); N (4.72); O (4.36). Found: C (71.04); H (4.76); N (4.32) (Figure 5).

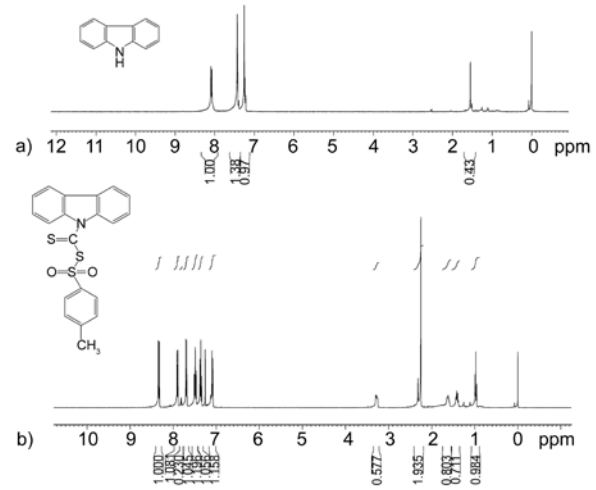


**Figure 4.** $^1$H-NMR spectra of a) Cz and b) TCzC

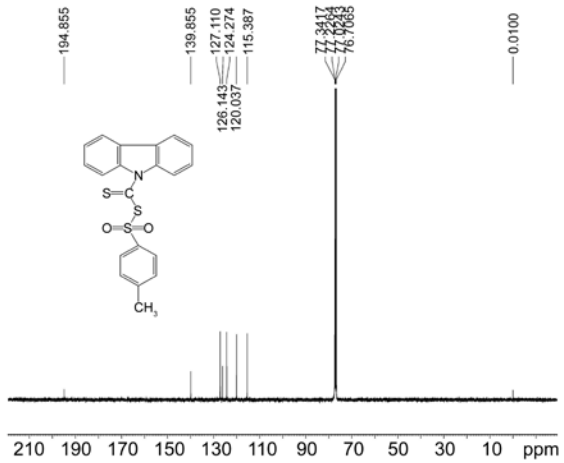


**Figure 5.** $^{13}$C-NMR spectrum of TCzC

## 3.3. Electropolymerization of poly(4-toluene 9*H*-carbazole-9-carbodithioate)

In our previous study [41], electrogrowth of 9-tosyl-9*H*-carbazole on the carbon fiber microelectrode (CFME) was studied by CV at a scan rate of 100 mV·s$^{-1}$ at different initial monomer concentrations (1.0, 3.0, 5.0 and 10.0 mM) in 0.1 M $NaClO_4$/ACN. The anodic peak potential appeared at 0.78 V in the initial monomer concentration of 3.0 mM, which was a reversible process. When $CS_2$ group included into 9-tosyl-9*H*-carbazole structure, anodic peak potential was increased from 0.78 to 1.30 V. The peak at 0.97 V can only be attributed to the redox properties of the polymer P(Cz), not to carbazole, the monomer as shown in Figure 6. The total charge of PCz was obtained as 6.128 mC for 8$^{th}$ cycle during electrogrowth process. When tosyl functional group was added to the Cz structure, it increased the

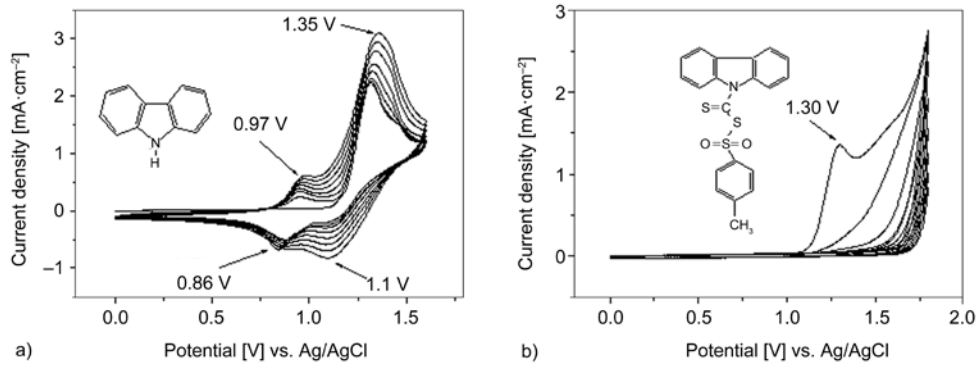


**Figure 6.** Cyclic voltammetry of a) Cz, $[Cz]_0$ = 3.0 mM ($Q$ = 6.128 mC), b) TCzC, $[TCzC]_0$ = 3.0 mM ($Q$ = 5.550 mC) on glassy carbon electrode (GCE) in 0.1 M $TEABF_4/CH_2Cl_2$–$CH_3CN$ (8:2), 8 cycle, scan rate: 50 mV·s$^{-1}$, potential range: 0.0– 1.8 V

$Q$ = 9.15 mC. However, after addition of $CS_2$ group into the functional tosyl carbazole structure, the total charge decreased to $Q$ = 5.55 mC during electrogrowth process. The main reason of this decrease may be increasing of the length of the carbazole structure. Another important effect of the diffusion and migration of tetrafluoroborate and alkylammonium ions, which has important influence on the EIS. Therefore, P(TCzC) was difficult to electropolymerize compared to PCz on GCE.

### 3.4. Effect of scan rate in monomer-free solution

P(Cz) and P(TCzC) were immersed into a monomer-free electrolyte solution to check their redox behaviours. Scan rate was an important factor on the polymerization behavior. Modified polymer films were measured at the scan rate of 50, 100, 250, 500 and 1000 mV·s$^{-1}$ in monomer-free solution. The CVs peak potentials were similar for all scan rates with a small increase in current, which showed the doping and de-doping process of the polymer-coated GCE [41]. The peak current density ($i_p$) for a reversible voltammogram at 25°C is given by the following equation: $i_p = (2.69 \cdot 10^5) \cdot A \cdot D^{1/2} \cdot C_o \cdot v^{1/2}$ where $v$ is the scan rate. $A$ is the electrode area, $D$ is the diffusion coefficient of electro-active species in the solution [42]. Peak current density is proportional $v^{1/2}$ in the range of scan rates (Regression fit ($R_{An}$ = 0.99069 and $R_{Cat}$ = –0.98381) for P(Cz) and (Regression fit ($R_{An}$ = 0.9982 and $R_{Cat}$ = –0.9972) for P(TCzC)/GCE where diffusion control applies [43], respectively as given in Figures 7 and 8.

### 3.5. FTIR-ATR measurements

In FTIR-ATR spectrum of PCz and P(TCzC) were given in Figures 9 and 10. A significant band at 1090 cm$^{-1}$ has been attributed to $BF_4^-$ ion for P(Cz), which is due to the electrolytes in $TEABF_4$. For the polymer, the band at 1600 cm$^{-1}$ could be assigned to the anti-symmetric and symmetric C–C stretching deformation. The peak at 3400 cm$^{-1}$ was obtained N–H stretching. The peak at 1230 and 720 cm$^{-1}$ corresponding to stretching of aromatic C–N bonds or vibration of disubstituted benzene ring and –C–H (out of plane deformation of C–H bond in benzene ring. P(TCzC) corresponds to peak at 3473 cm$^{-1}$ for C–H stretching, at 1626 cm$^{-1}$ for C=C stretching, at 1483 cm$^{-1}$ for $CH_3$, at 1046 cm$^{-1}$ for dopant ion ($BF_4^-$) and at 762 cm$^{-1}$ for C–S stretching (Figure 10). The peak at 1156 cm$^{-1}$ was the bond of S=O bond in carbazole structure [44]. In our previous paper, PCz was electropolymerized on CFME in 0.1 M $NaClO_4$/PC. A significant band at 1093 cm$^{-1}$ was attributed to $ClO_4^-$ ion. Other characteristic peaks at 3559, 1626, 1233 and 681–728 cm$^{-1}$ refer

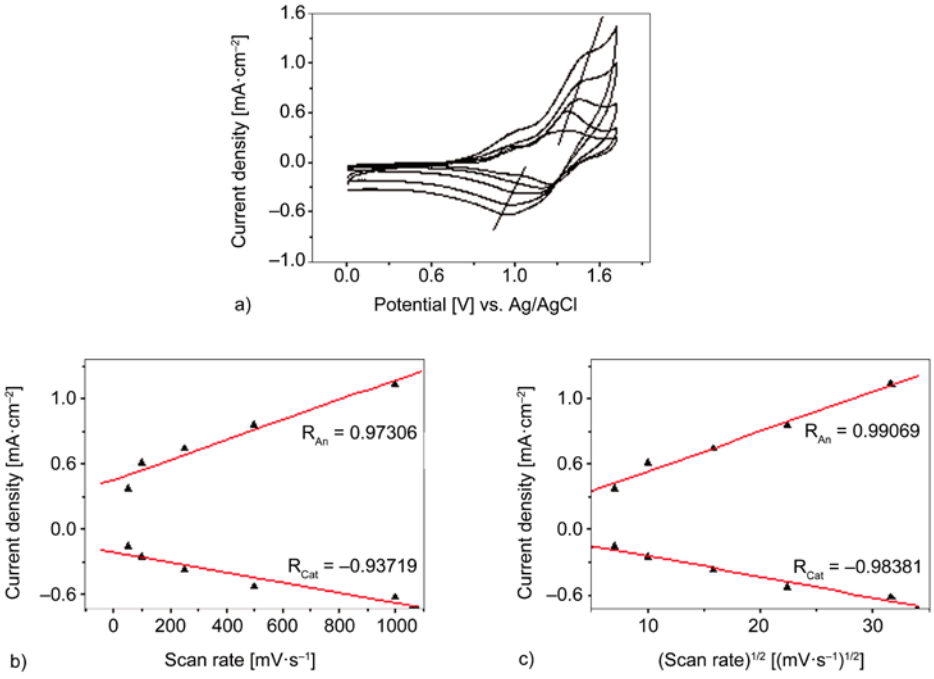


**Figure 7.** a) CV of PCz was obtained at different scan rates in monomer-free solution, b) scan rate vs. Current density, c) square root of scan rate vs. current density plots, CV was taken as 8 cycle, scan rate: 50–1000 mV·s$^{-1}$, potential range: 0–1.8 V in 0.1 M $TEABF_4/CH_2Cl_2$–$CH_3CN$ (8:2), $[Cz]_0$ = 3.0 mM.

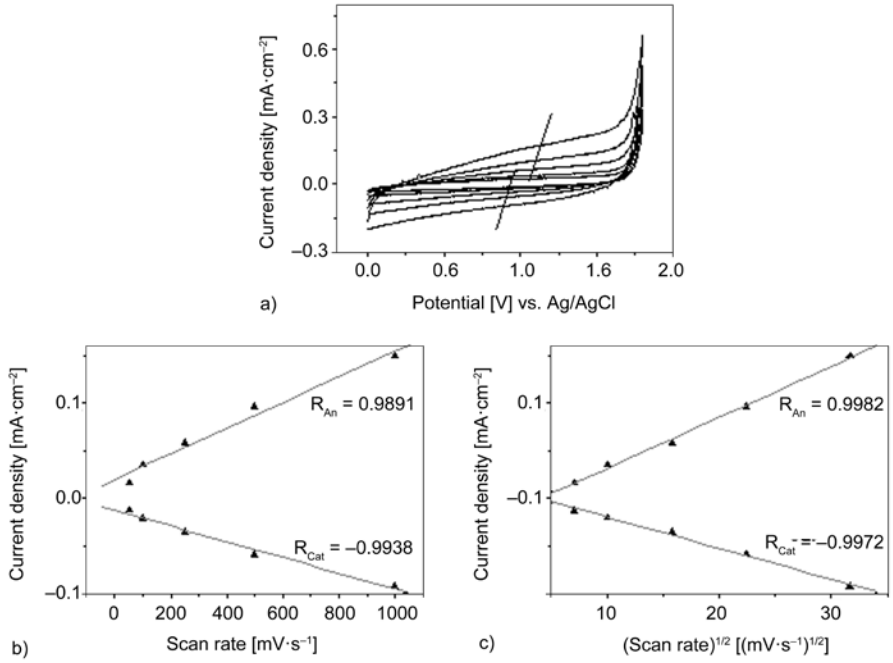


**Figure 8.** a) CV of P(TCzC) was obtained at different scan rates in monomer-free solution, b) scan rate vs. current density, c) square root of scan rate vs. current density plots, 8 cycle, scan rate: 50–1000 $mV \cdot s^{-1}$, potential range: 0–1.8 V in 0.1 M $TEABF_4/CH_2Cl_2$–$CH_3CN$ (8:2), $[TCzC]_0$ = 3.0 mM

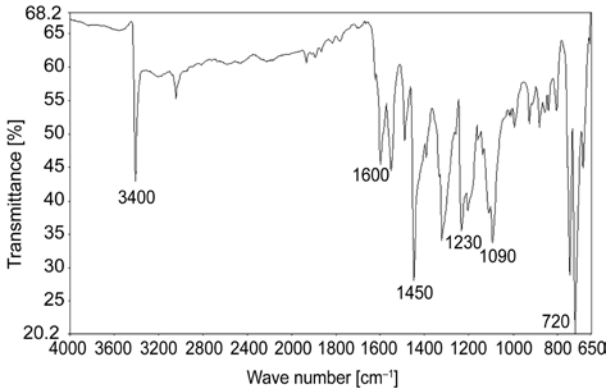


**Figure 9.** FTIR-ATR spectrum of P(Cz)/CFME in 0.1 M $TEABF_4/CH_2Cl_2$–$CH_3CN$ (8:2)

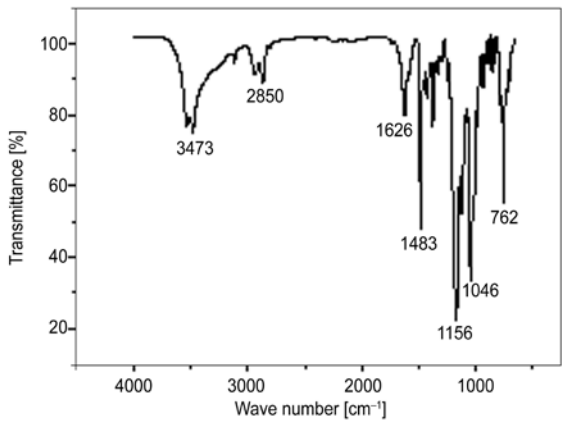


**Figure 10.** FTIR-ATR spectrum of P(TCzC)/CFME in 0.1 M $TEABF_4/CH_2Cl_2$–$CH_3CN$ (8:2)

to $–CH_3$ ($sp^3$ CH str.), the anti-symmetric and symmetric C=C str. Deformation, –C–N (str. of aromatic C–N bonds or vibrational of disubstituted benzene ring) and C–H (out of plane deformation of C–H bond in benzene ring) [45], respectively. PCz and P(TCzC) have different characteristic peaks to differentiate the functionality of polycarbazole.

### 3.6. SEM and AFM measurements

SEM micrograph of P(TCzC)/CFME was shown in Figure 11. Polymerization was performed on a single CFME (with diameter approximately 0.022 $cm^2$). Some pores of granules were shown on the CFME.

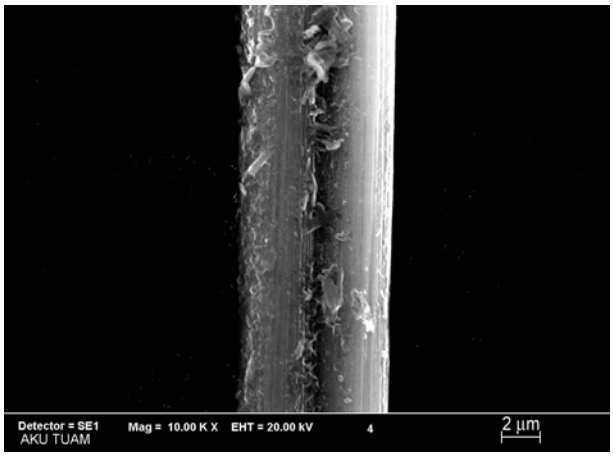


**Figure 11.** SEM images of P(TCzC)/CFME was performed in 0.1 M $TEABF_4/CH_2Cl_2$–$CH_3CN$ (8:2) while the electropolymerization was carried out

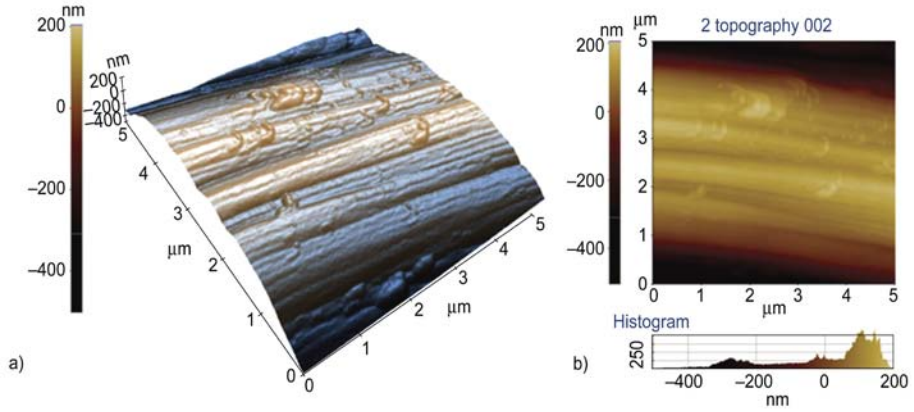


**Figure 12.** AFM analysis of P(TCzC)/CFME was performed in 0.1 M $TEABF_4/CH_2Cl_2$–$CH_3CN$(8:2) while the electropolymerization was carried out

AFM images of P(TCzC)/CFME were obtained by fixing the fiber on a piece of silicon wafer with resin as shown in Figure 12. The AFM average roughness ($R_q$) value was obtained as 248.6 nm. AFM images of P(TCzC) was given in Figure 12. The electro-coating of modified electrodes was observed with granules on CFME. It was found in our previous study [46] from the cross-sectional analyses that striations of uncoated CFME with approximately 1 µm depth started disappearing and lower a thickness value of 50 nm. There is no doubt that average roughness value of uncoated CFME was increased ~5 times by electro-coating process. It is strong evidence of successful polymer formation provided by AFM analysis.

### 3.7. Electrochemical impedance spectroscopic study

Among electrochemical characterization techniques EIS represented useful results for the investigation of conducting polymers due to the small perturbations involved in the operative conditions for the impedance measurements [47, 48]. The impedance measurements, resistance was the real part and capacitance was calculated as $C = -1/(2\pi fZ'')$, where $\pi = 3.14$, $f$ was frequency in Hz, and $Z''$ was the imaginary part of the impedance [49]. The low frequency capacitances (10 mHz) of P(Cz) ($C_{LF} = 1.44$ mF·cm$^{-2}$) and P(TCzC)/GCE ($C_{LF} = 0.43$ mF·cm$^{-2}$) were taken to identify the specific capacitance of polymer modified films. For lower frequencies, the spectra approached a nearly vertical line in the complex plane, which was typical of an ideal capacitor behavior. $C_{LF}$ value decreased of 3.34 times by addition of $CS_2$ and tosyl group into the carbazole monomer (Figure 13a). In the Bode-phase plot, the maximum phase angle was obtained as ~65° at the frequency of ~5 Hz as given in Figure 13b. The maximum capacitance value of P(TCzC)/GCE was obtained as ~37 µF as shown in Figure 13c.

The model circuit comprised of eight elements, the solution resistance ($R_s$) was in series with the electrical double layer capacitance ($C_{dl}$) at the electrode and electrolyte. $C_{dl}$ was in parallel with $R_1$ and ($R_2$, $W$, and $Q$). The Warburg impedance was associated with the semi-infinite diffusion of ions in the electrode [50, 51]. The values of circuit parameters were estimated qualitatively from the fittings of experimental impedance spectra and presented for PCz/GCE in Table 1 and P(TCzC)/GCE in Table 2. The mean error of the modulus was ~10%. The chi-squared ($\chi^2$) was obtained as $10^{-3}$ and $10^{-4}$ for the circuit evaluations. $\chi^2$ was the function defined as the sum of the squares of the residuals.

In literature, capacitors and supercapacitors are modeled by using many simple *RC* circuits. However, these models cannot accurately describe the voltage behavior of the modified polymer film and elec-

**Table 1.** Electrical equivalent circuit model of $R(C(R(Q(RW))))(CR)$, which is obtained for PCz/GCE

| Circuit components | DC potential for PCz/GCE | | | |
|---|---|---|---|---|
| | **–0.1 V** | **0.1 V** | **0.5 V** | **1.0 V** |
| $R_s$ [Ω] | 360.7 | 313.0 | 300.3 | 313.2 |
| $C_{dl}$ [µF] | 2.24 | 1.61 | $4.54\cdot10^{-2}$ | $6.21\cdot10^{-2}$ |
| $R_1$ [Ω] | 560.4 | 142.9 | 40.3 | 5.29 |
| $Q$ [µS·s$^n$] | 12.6 | 16.0 | 18.8 | 12.4 |
| $n$ | 0.76 | 0.80 | 0.71 | 0.74 |
| $R_2$ [Ω] | $1.29\cdot10^5$ | $7.08\cdot10^4$ | $3.18\cdot10^4$ | 202.3 |
| $W$ [µS·s$^{-n}$] | 18.0 | 36.8 | 144.0 | 21.7 |
| $C_{GCE}$ [µF] | 0.624 | 0.041 | 43.5 | 0.94 |
| $R_{GCE}$ [Ω] | 48.0 | 38.6 | 9924.0 | 1068.0 |
| $\chi^2$ | $5.54\cdot10^{-4}$ | $9.02\cdot10^{-4}$ | $3.28\cdot10^{-4}$ | $2.04\cdot10^{-3}$ |

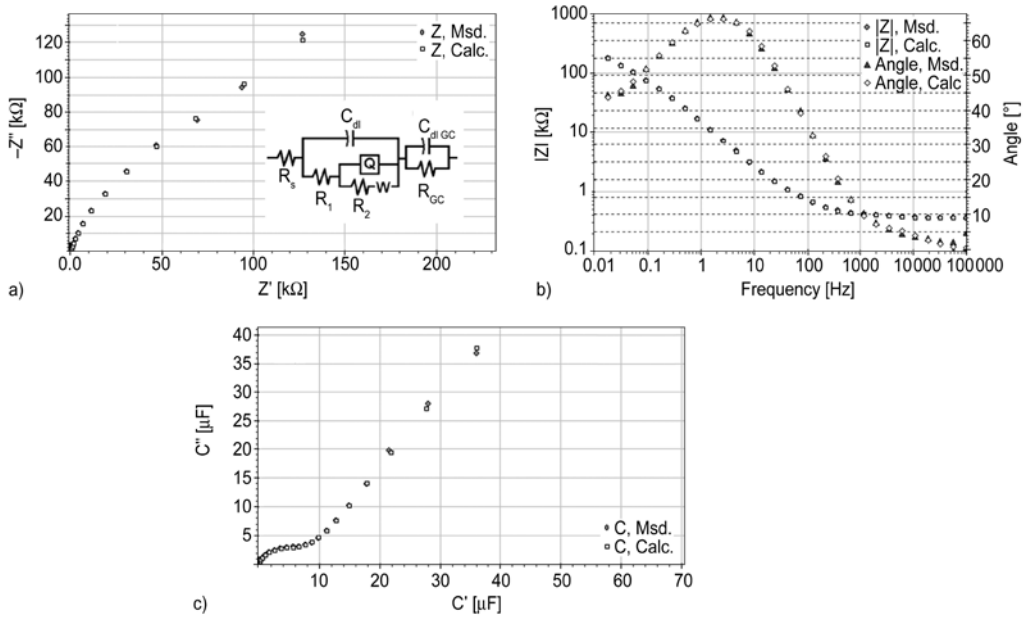


**Figure 13.** a) Nyquist graph inset: electrical equivalent circuit model of $R(C(R(Q(RW))))(CR)$, b) Bode magnitude and Bode-phase plot, c) capacitance graph of poly(TCzC) obtained by simulation ZSimpWin 3.10 program. Experiments were performed by simulation as the following conditions. $[TCzC]_0$ = 3.0 mM, 0.1 M $TEABF_4$/$CH_2Cl_2$–$CH_3CN$ (8:2). Potential range was taken from 0 to1.8 V.

**Table 2.** Electrical equivalent circuit model of $R(C(R(Q(RW))))(CR)$, which is obtained for P(TCzC)/GCE

| Circuit components | DC Potential for P(TCzC)/GCE | | | |
|---|---|---|---|---|
| | **–0.1 V** | **0.1 V** | **0.5 V** | **1.0 V** |
| $R_s$ [Ω] | 381.8 | 216.0 | 342.2 | 330.8 |
| $C_{dl}$ [μF] | 0.87 | 0.46 | 0.67 | 0.69 |
| $R_1$ [Ω] | 0.01 | 144.5 | 62.4 | 0.09 |
| $Q$ [μS·s$^n$] | 4.39 | 1.75 | 5.80 | 18.9 |
| $n$ | 0.48 | 0.82 | 0.79 | 0.89 |
| $R_2$ [Ω] | $3.82\cdot10^6$ | $7.53\cdot10^4$ | $1.47\cdot10^5$ | 0.037 |
| $W$ [μS·s$^{-n}$] | 252.0 | 5.48 | 18.2 | 34.7 |
| $C_{GCE}$ [μF] | 1.41 | 1.35 | 19.1 | 8.75 |
| $R_{GCE}$ [Ω] | 67.4 | 147.0 | 3734.0 | 1026.0 |
| $\chi^2$ | $1.06\cdot10^{-3}$ | $3.65\cdot10^{-4}$ | $3.14\cdot10^{-4}$ | $2.47\cdot10^{-3}$ |

trolyte system [52, 53]. For fitting the data all capacitances in the equivalent circuit model of $R(C(R(Q(RW))))(CR)$ had to be replaced by a constant phase element CPE or $Q$ [$Z_{CPE} = A_{CPE}(jw)^{-n}$] in order to adopt for non ideal behavior [54]. If $n$ = 1 then $1/A_{CPE} = C$ with the dimension F·cm$^{-2}$. The value of an ideal capacitance can be determined from the Bode plot of the impedance by extraploting the measured capacitance with the slope $-n$ to the frequency $f$ = 1000 Hz [55]. The highest $n$ value of PCz was obtained as 0.80 at the DC potential of 0.1 V by applying EIS measurement. However, there were values as 0.82 and 0.89 for P(TCzC)/GCE system at the potential of 0.1 and 1.0 V, respectively. The highest double layer capacitance ($C_{dl}$) was obtained as

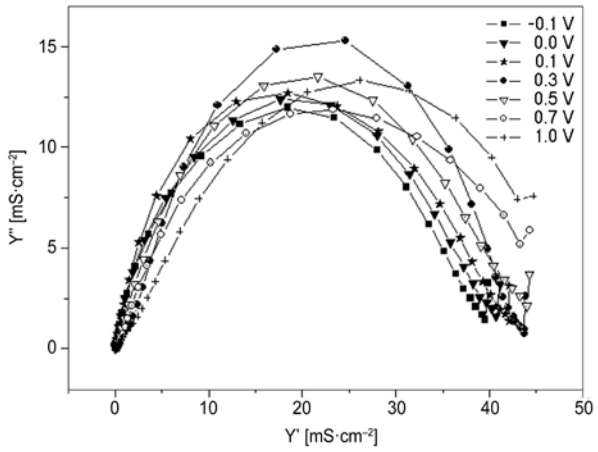


**Figure 14.** Admittance graph of P(TCzC) obtained by different DC potentials from –0.1 to 1.0 V. $[TCzC]_0$ = 3.0 mM, 0.1 M $TEABF_4$/$CH_2Cl_2$–$CH_3CN$ (8:2). Potential range was taken from 0 to1.8 V.

2.24 μF for PCz and 0.87 μF for P(TCzC)/GCE at the DC potential of –0.1 V. $R_1$ and $R_2$ values decrease by increasing of DC potential of PCz. However, there was no systematic relation of P(TCzC)/GCE. The highest $R_1$ = 144.5 Ω at the DC potential of 0.1 V. However, $R_2$ = 3.82 MΩ at the DC potential of –0.1 V.

The highest conductivity of P(TCzC)/GCE was obtained at the DC potential of 0.3 V for P(TCzC)/GCE as shown in Figure 14. There was an order from DC potential from –0.1 to 1.0 V. There was a deviation of 0.3 V for the P(TCzC)/GCE.

## 4. Conclusions

EIS was employed to characterize the capacitive behavior of electrochemically prepared novel synthesis of P(TCzC) film electrodes in organic electrolytes. The changing of polymer capacitance in dependence of the potential range from –0.1 to 1.0 V for PCz and P(TCzC)/GCE. $C_{dl}$ was obtained as 2.24 μF for PCz and 0.87 μF for P(TCzC)/GCE at the DC potential of –0.1 V. And the resistance of GCE was obtained as $R_{GCE}$ = 9924 Ω for PCz and $R_{GCE}$ = 3734 Ω for P(TCzC) at the DC potential of 0.5 V. The double layer capacitance of P(TCzC) was lower than PCz. $CS_2$ group with tosyl group into Cz monomer decreased the capacitor behavior of the polymer.

## Acknowledgements

This work was supported by The Scientific & Technological Council of Turkey (TUBITAK)-TBAG-110T791 Project. Authors also thank to Yakup Bakis (Fatih University, BINATAM, Istanbul, Turkey) for recording AFM images.

## References

[1] Gupta B., Singh A. K., Prakash R.: Electrolyte effects on various properties of polycarbazole. Thin Solid Films, **519**, 1016–1019 (2010). DOI: 10.1016/j.tsf.2010.08.034

[2] Inzelt Gy.: Formation and redox behaviour of polycarbazole prepared by electropolymerization of solid carbazole crystals immobilized on an electrode surface. Journal of Solid State Electrochemistry, **7**, 503–510 (2003). DOI: 10.1007/s10008-003-0357-0

[3] Du Y., Shen S. Z., Cai K. F., Casey P. S.: Research progress on polymer-inorganic thermoelectric nanocomposite materials. Progress in Polymer Science, **37**, 820–841 (2012). DOI: 10.1016/j.progpolymsci.2011.11.003

[4] Deng J., Guo L., Xiu Q., Zhang L., Wen G., Zhong C.: Two polymeric metal complexes based on polycarbazole containing complexes of 8-hydroxyquinoline with Zn(II) and Ni(II) in the backbone: Synthesis, characterization and photovoltaic applications. Materials Chemistry and Physics, **133**, 452–458 (2012). DOI: 10.1016/j.matchemphys.2012.01.064

[5] Bussiére P-O., Rivaton A., Thérias S., Gardette J-L.: Multiscale investigation of the poly(*N*-vinylcarbazole) photoageing mechanism. Journal of Physical Chemistry B, **116**, 802–812 (2012). DOI: 10.1021/jp211358q

[6] Ates M., Uludag N., Karazehir T.: Copolymer formation of 9-(2-(benzyloxy)ethyl)-9*H*-carbazole and 1-tosyl-1*H*-pyrrole coated on glassy carbon electrode and electrochemical impedance spectroscopy. Journal of Solid State Electrochemistry, **16**, 2639–2649 (2012). DOI: 10.1007/s10008-012-1688-5

[7] Stolar M., Baumgartner T.: Synthesis and unexpected halochromism of carbazole-functionalized dithienophospholes. New Journal of Chemistry, **36**, 1153–1160 (2012). DOI: 10.1039/c2nj40022g

[8] Gupta B., Joshi L., Prakash R.: Novel synthesis of polycarbazole–gold nanocomposite. Macromolecular Chemistry and Physics, **212**, 1692–1699 (2011). DOI: 10.1002/macp.201100262

[9] Li S., Zhuang L-Q., George T. F.: Electric field-tuned polymer amplified spontaneous emission. Journal of the Electrochemical Society, **159**, P29–P34 (2012). DOI: 10.1149/2.001203jes

[10] Pawar S. G., Chougule M. A., Sen S., Patil V. B.: Development of nanostructured polyaniline–titanium dioxide gas sensors for ammonia recognition. Journal of Applied Polymer Science, **125**, 1418–1424 (2012). DOI: 10.1002/app.35468

[11] Booth M. A., Harbison S., Travas-Sejdic J.: Effects of redox couple on the response of polypyrrole-based electrochemical DNA Sensors. Electroanalysis, **24**, 1311–1317 (2012). DOI: 10.1002/elan.201200119

[12] Drelinkiewicz A., Zięba A., Solbezak J. W., Bonarawska M., Karpiński Z., Walksmundzka-Góra A., Stejskal J.: Polyaniline stabilized highly dispersed Pt nanoparticles: Preparation, characterization and catalytic properties. Reactive and Functional Polymers, **69**, 630–642 (2009). DOI: 10.1016/j.reactfunctpolym.2009.04.007

[13] Nie G., Xu J., Zhang S., Cai T., Han X.: Electrochemical copolymerization of carbazole and 3-methylthiophene. Journal of Applied Polymer Science, **102**, 1877–1885 (2006). DOI: 10.1002/app.24157

[14] Huang M-R., Lu H-J., Li X-G.: Synthesis and strong heavy-metal ion sorption of copolymer microparticles from phenylenediamine and its sulfonate. Journal of Materials Chemistry, **22**, 17685–17699 (2012). DOI: 10.1039/c2jm32361c

[15] Li X-G., Feng H., Huang M-R., Gu G-L., Moloney M. G.: Ultrasensitive Pb(II) potentiometric sensor based on copolyaniline nanoparticles in a plasticizer-free membrane with a long lifetime. Analytical Chemistry, **84**, 134–140 (2012). DOI: 10.1021/ac2028886

[16] Li X-G., Lü Q-F., Huang M-R.: Self-stabilized nanoparticles of ıntrinsically conducting copolymers from 5-sulfonic-2-anisidine. Small, **4**, 1201–1209 (2008). DOI: 10.1002/smll.200701002

[17] Ates M., Uludag N., Karazehir T., Arican F.: A novel synthesis of 3,6-bis(2,3-dihydrothieno[3,4-b][1,4]dioxin-5-yl)-9-tosyl-9*H*-carbazole. Ovidius University Annals of Chemistry, **23**, 63–71 (2012).
DOI: 10.2478/v10310-012-0010-9

[18] Uludag N., Ates M., Tercan B., Hökelek T.: 5-(3,6-dibromo-9*H*-carbazol-9-yl)pentanenitrile. Acta Crystallographica Section E: Structure Report Online, **67**, o642 (2011).
DOI: 10.1107/S1600536811005162

[19] Ates M., Uludag N., Sarac A. S.: Synthesis and electropolymerization of 9-tosyl-9*H*-carbazole, electrochemical impedance spectroscopic study and circuit modelling. Fibers and Polymers, **12**, 8–14 (2011).
DOI: 10.1007/s12221-011-0008-5

[20] Ates M., Uludag N., Sarac A. S.: Electrochemical impedance of poly(9-tosyl-9*H*-carbazole-co-pyrrole) electrocoated carbon fiber. Materials Chemistry and Physics, **127**, 120–127 (2011).
DOI: 10.1016/j.matchemphys.2011.01.050

[21] Lee H-Y, Chen G. S., Chen C-S., Chern J-W.: Efficient microwave-assisted synthesis of ellipticine through *N*-(1,4-dimethyl-9*H*-carbazol-3-ylmethyl)-*N*-tosylaminoacetaldehyde diethyl acetal. Journal of Heterocyclic Chemistry, **47**, 454–458 (2010).
DOI: 10.1002/jhet.319

[22] Hökelek T., Dal H., Tercan B., Gülle S., Ergün Y.: Ethyl 4-hydroxy-9-tosyl-9*H*-carbazole-3-carboxylate. Acta Crystallographica Section E: Structure Reports Online, **65**, o1515–o1516 (2009).
DOI: 10.1107/S1600536809021035

[23] Gu Y., Chen W-Q., Wada T., Hashizume D., Duan X-M.: From supermolecular sheet to helix by breaking molecular symmetry: the case of 4-[2-(carbazol-3-yl) vinyl] pyridium tosylate. CrystEngComm, **9**, 541–544 (2007).
DOI: 10.1039/b701377a

[24] Martinez-Esperón M. F., Rodríquez D., Castedo L., Saá C.: Coupling and cycloaddition of ynamides: homo- and Negishi coupling of tosylynamides and intramolecular [4+2] cycloaddition of *N*-(*o*-ethynyl)phenyl ynamides and arylynamides. Tetrahedron, **62**, 3843–3855 (2006).
DOI: 10.1016/j.tet.2005.11.082

[25] Ates M., Uludag N.: Synthesis of 9-(4-nitrophenylsulfonyl)-9*H*-carbazole: Comparison of an impedance study of poly[9-(4-nitrophenylsulfonyl)-9*H*-carbazole] on gold and carbon fiber microelectrodes. Journal of Applied Polymer Science, **124**, 4655–4662 (2012).
DOI: 10.1002/app.35380

[26] Beaujuge P. M., Reynolds J. R.: Color control in π-conjugated organic polymers for use in electrochromic devices. Chemical Reviews, **110**, 268–320 (2010).
DOI: 10.1021/cr900129a

[27] Kötz R., Hahn M., Gallay R.: Temperature behavior and impedance fundamentals of supercapacitors. Journal of Power Sources, **154**, 550–555 (2006).
DOI: 10.1016/j.jpowsour.2005.10.048

[28] Vorotyntsev M. A., Daikhin L. I., Levi M. D.: Modelling the impedance properties of electrodes coated with electroactive polymer films. Journal of Electroanalytical Chemistry, **364**, 37–49 (1994).
DOI: 10.1016/0022-0728(93)02957-J

[29] Inzelt G., Pineri M., Schultze J. W., Vorotyntsev M. A.: Electron and proton conducting polymers: recent developments and prospects. Electrochimica Acta, **45**, 2403–2421 (2000).
DOI: 10.1016/S0013-4686(00)00329-7

[30] Aravinda L. S., Bhat K. U., Bhat B. R.: Nano $CeO_2$/activated carbon based composite electrodes for high performance supercapacitor. Materials Letters, **112**, 158–161 (2013).
DOI: 10.1016/j.matlet.2013.09.009

[31] Yang J. E., Jang I., Kim M., Baeck S. H., Hwang S., Shim S. E.: Electrochemically polymerized vine-like nanostructured polyaniline on activated carbon nanofibers for supercapacitor. Electrochimica Acta, **111**, 136–143 (2013).
DOI: 10.1016/j.electacta.2013.07.183

[32] Zhang L. L., Zhao X. S.: Carbon-based materials as supercapacitor electrodes. Chemical Society Reviews, **38**, 2520–2531 (2009).
DOI: 10.1039/b813846j

[33] Li C., Wang D., Liang T., Wang X., Ji L.: A study of activated carbon nanotubes as double-layer capacitors electrode materials. Materials Letters, **58**, 3774–3777 (2004).
DOI: 10.1016/j.matlet.2004.07.027

[34] Hwang S-G., Ryu S-H., Yun S-R., Ko J. M., Kim K. M., Ryu K-S.: Behavior of NiO–$MnO_2$/MWCNT composites for use in a supercapacitor. Materials Chemistry and Physics, **130**, 507–512 (2011).
DOI: 10.1016/j.matchemphys.2011.07.022

[35] Kuang H., Cao Q., Wang X., Jing B., Wang Q., Zhou L.: Influence of the reaction temperature on polyaniline morphology and evaluation of their performance as supercapacitor electrode. Journal of Applied Polymer Science, **130**, 3753–3758 (2013).
DOI: 10.1002/app.39650

[36] He X., Gao B., Wang G., Wei J., Zhao C.: A new nanocomposite: Carbon cloth based polyaniline for an electrochemical supercapacitor. Electrochimica Acta, **111**, 210–215 (2013).
DOI: 10.1016/j.electacta.2013.07.226

[37] Lu T., Zhang Y., Li H., Pan L., Li Y., Sun Z.: Electrochemical behaviors of graphene–ZnO and graphene–$SnO_2$ composite films for supercapacitors. Electrochimica Acta, **55**, 4170–4173 (2010).
DOI: 10.1016/j.electacta.2010.02.095

[38] Zhi M., Xiang C., Li J., Li M., Wu N.: Nanostructured carbon–metal oxide composite electrodes for supercapacitors: A review. Nanoscale, **5**, 72–88 (2013).
DOI: 10.1039/c2nr32040a

[39] Zhou D., Zhu X. L., Zhu J., Yin H. S.: Influence of the chemical structure of dithiocarbamates with different *N*-groups on the reversible addition–fragmentation chain transfer polymerization of styrene. Journal of Polymer Science Part A: Polymer Chemistry, **43**, 4849–4856 (2005).
DOI: 10.1002/pola.20947

[40] Xue X., Zhu J., Zhang Z., Cheng Z., Tu Y., Zhu X.: Synthesis and characterization of azobenzene-functionalized poly(styrene)-*b*-poly(vinyl acetate) via the combination of RAFT and 'click' chemistry. Polymer, **51**, 3083–3090 (2010).
DOI: 10.1016/j.polymer.2010.04.052

[41] Sarac A. S., Evans U., Serantoni M., Cunnane V. J.: Electrochemical and morphological study of the effect of polymerization conditions on poly(tetrathiophene) with emphasis on carbon fiber microelectrodes: A cyclic voltammetry and atomic force microscopy study. Carbon, **41**, 2725–2730 (2003).
DOI: 10.1016/S0008-6223(03)00331-2

[42] Sarac A. S., Ates M., Parlak E. A.: Electrolyte and solvent effects of electrocoated polycarbazole thin films on carbon fiber microelectrodes. Journal of Applied Electrochemistry, **36**, 889–898 (2006).
DOI: 10.1007/s10800-006-9145-8

[43] Rusling J. F., Suib S. L.: Characterizing materials with cyclic voltammetry. Advanced Materials, **6**, 922–930 (1994).
DOI: 10.1002/adma.19940061204

[44] Sarac A. S., Sezgin S., Ates M., Turhan C. M.: Electrochemical impedance spectroscopy and morphological analyses of pyrrole, phenylpyrrole and methoxyphenylpyrrole on carbon fiber microelectrodes. Surface and Coatings Technology, **202**, 3997–4005 (2008).
DOI: 10.1016/j.surfcoat.2008.02.007

[45] Papež V., Inganäs O., Cimrová V., Nešpůrek S.: Electrochemical preparation and study of thin poly(*N*-vinylcarbazole) layers. Journal of Electroanalytical Chemistry and Interfacial Electrochemistry, **282**, 123–139 (1990).
DOI: 10.1016/0022-0728(91)85093-5

[46] Sarac A. S., Sezgin S., Ates M., Turhan M. C.: Monomer concentration effect on electrochemically modified carbon fiber with poly[1-(4-methoxyphenyl)-1*H*-pyrrole] as microcapacitor electrode. Advances in Polymer Technology, **28**, 120–130 (2009).
DOI: 10.1002/adv.20152

[47] Musiani M. M.: Characterization of electroactive polymer layers by electrochemical impedance spectroscopy (EIS). Electrochimica Acta, **35**, 1665–1670 (1990).
DOI: 10.1016/0013-4686(90)80023-H

[48] Tarola A., Dini D., Salatelli E., Andreani F., Decker F.: Electrochemical impedance spectroscopy of polyalkylterthiophenes. Electrochimica Acta, **44**, 4189–4193 (1999).
DOI: 10.1016/S0013-4686(99)00133-4

[49] Miller J. R., Outlaw R. A., Holloway B. C.: Graphene electric double layer capacitor with ultra-high-power performance. Electrochimica Acta, **56**, 10443–10449 (2011).
DOI: 10.1016/j.electacta.2011.05.122

[50] Sen P., De A.: Electrochemical performances of poly(3,4-ethylenedioxythiophene)–$NiFe_2O_4$ nanocomposite as electrode for supercapacitor. Electrochimica Acta, **55**, 4677–4684 (2010).
DOI: 10.1016/j.electacta.2010.03.077

[51] Conway B. E.: Electrochemical supercapacitors, scientific fundamantals and technological applications. Kluwer Academic/Plenum Publishers, New York (1999).

[52] Mahon P. J, Paul G. L., Keshishian S. M., Vassallo A. M.: Measurement and modelling of the high-power performance of carbon-based supercapacitors. Journal of Power Sources, **91**, 68–76 (2000).
DOI: 10.1016/S0378-7753(00)00488-2

[53] Buller S., Karden E., Kok D., De Donker R. W.: Modeling the dynamic behavior of supercapacitors using impedance spectroscopy. IEEE Transactions on Industry Applications, **38**, 1622–1626 (2002).
DOI: 10.1109/TIA.2002.804762

[54] Rammelt U., Reinhard G.: On the applicability of a constant phase element (CPE) to the estimation of roughness of solid metal electrodes. Electrochimica Acta, **35**, 1045–1049 (1990).
DOI: 10.1016/0013-4686(90)90040-7

[55] Fikus A., Rammelt U., Plieth W.: Characterization of semiconductor properties of polybithiophene film electrodes in contact with aqueous electrolytes. A combination of electrochemical impedance spectroscopy and photocurrent measurements. Electrochimica Acta, **44**, 2025–2035 (1999).
DOI: 10.1016/S0013-4686(98)00311-9

*eXPRESS Polymer Letters Vol.8, No.7 (2014) 491–504*
*Available online at www.expresspolymlett.com*
*DOI: 10.3144/expresspolymlett.2014.53*

# Improving the bonding between henequen fibers and high density polyethylene using atmospheric pressure ethylene-plasma treatments

*A. Aguilar-Rios*[1], *P. J. Herrera-Franco*[1], *A. de J. Martínez-Gómez*[2], *A. Valadez-González*[1*]

[1]Centro de Investigación Científica de Yucatán, A.C. 130 No.43, Chuburná de Hidalgo, 97200 Mérida, Yucatán, México
[2]Departamento de Ingeniería Química Universidad de Guadalajara, Blvd. Marcelino García Barragán, 1421 Guadalajara Jalisco, México

*Received 17 December 2013; accepted in revised form 19 March 2014*

**Abstract.** In order to improve the bonding between henequen fibers (*Agave fourcroydes*) and High Density Polyethylene (HDPE), they were treated in an ethylene-dielectric barrier discharge (DBD) plasma operating at atmospheric pressure. A $2^3$ factorial experimental design was used to study the effects of the plasma operational parameters, namely, frequency, flow rate and exposure time, over the fiber tensile mechanical properties and its adhesion to HDPE. The fiber-matrix Interfacial Shear Strength (IFSS) was evaluated by means of the single fiber pull-out test. The fiber surface chemical changes were assessed by photoacoustic Fourier transform infrared spectroscopy (PAS-FTIR) and the changes in surface morphology with scanning electron microscopy (SEM). The results indicate that individual operational parameters in the DBD plasma treatment have different effects on the tensile properties of the henequen fibers and on its bonding to HDPE. The SEM results show that the plasma treatment increased the roughness of the fiber surface. The FTIR result seems to indicate the presence of a hydrocarbon-like polymer film, bearing some vinyl groups deposited onto the fibers. These suggests that the improvement in the henequen-HDPE bonding could be the result of the enhancement of the mechanical interlocking, due the increment in roughness, and the possible reaction of the vinyl groups on the film deposited onto the fiber with the HDPE.

***Keywords:*** *adhesion, atmospheric dielectric barrier discharge, henequen fiber, HDPE, IFSS*

## 1. Introduction

Recent environmental concerns have triggered the use of natural fibers because they fulfil the sustainability criteria for development in the third millennium, and are readily available from renewable sources at a low price. Natural fibers like henequen, sisal, jute, coir, etc. possess physical and mechanical properties that make them attractive as reinforcing materials for the substitution of engineering man-made fibers which are neither biodegradable nor renewable. Additionally, their hollow tubular structure enhances their acoustic and thermal insulating properties, which could lead to energy saving in several industrial applications [1–8].

Several studies on henequen fibers (*Agave fourcroydes*) reinforced polyolefins composites have been conducted in the last few years. The most important drawback to overcome for a more ample use of these hydrophilic natural fibers in composites is their chemical incompatibility with hydrophobic thermoplastic polyolefins. It is known that incompatibility at the fiber-matrix interface limits the stress transfer capability, meaning that the reinforcing potential of natural fibers cannot be exploited to

*Corresponding author, e-mail: avaladez60@gmail.com

their full extent, especially for short fiber composites [9–14].

Several chemical-based approaches have been used to improve the compatibility between natural fibers with different polymeric matrices, e.g. alkali treatments (mercerization), silanization, acetylation, benzoylation, maleated coupling agents, isocyanate treatments and grafting of synthetic polymers [1, 3, 7, 12, 13, 15–17]. Silanization is by far most effective fiber surface treatment, judged by the improvements in material property increases, above a 100% in the tensile and flexural strengths [11, 12]. However, even though the wet chemical treatments of fiber surfaces have been somewhat successful in improving the interfacial bonding, there are still problems related to the appropriate handling and disposal of the large amounts of hazardous chemicals that are often involved and concerned with environmental pollution problems. These problems have limited a wider industrial application of chemical fiber surface treatments [4, 16–20]. Cold plasma is a solvent-free technique with no liquid waste generated and can therefore be considered as an environmentally sound method. Also, the plasma-based surface modification is restricted to a thin depth of the material, e.g. the bulk properties of materials are retained and it uses small quantities of monomers. The surface functionalization can be carried out in one step and several functional groups, e.g. OH, COOH, $NH_2$, CNH, can be grafted on polymer surface depending on monomer selected [21–25]. de Valence *et al*. [26] studied the effect of cold air plasma treatment on the hydrophilicity of electrospun polycaprolactone scaffolds in order to improve cell-material interactions and promote better tissue regeneration for biodegradable vascular graft applications. They pointed out that the plasma treatment significantly increased the hydrophilicity of the scaffold and accelerated tissue regeneration without compromising the mechanical strength, which are valuable advantages for vascular tissue engineering. Kaklamani *et al.* [27] pointed out that the active screen plasma nitridizing (ASPN) treatment of UHMWPE enhanced cell attachment without altering the mechanical properties and topography of the polymer surface. They treated the UHMWPE with a gas mixture 80% $N_2$ and 20% $H_2$ (v/v) at 2.5 mbar pressure and 90°C followed by growth of 3T3 fibroblasts on the treated and untreated polymer surfaces. The chemical properties of the ASPN-treated UHMWPE surface were studied using X-ray photoelectron spectroscopy, revealing the presence of C–N, C=N, and C≡N chemical bonds. Parvinzadeh Gashti *et al.* [28] carried out the plasma functionalization of PET using $Ar/O_2$ (4:1) and $NH_3/C_2H_4$ (1:1) gas mixtures followed by incubation in simulated body fluids (SBF) in order to investigate the effect of the cold plasma process in the formation of bone-like hydroxyapatite (HAp). Their results suggest that $Ar/O_2$ and $NH_3/C_2H_4$ plasmas as potentially useful tools for bone tissue regeneration procedures. The use of the dielectric barrier discharge-process (DBD) to generate a reactive cold plasma to modify the surface chemistry of synthetic a natural materials has been explored by several groups [24, 25]. It is characterized by relatively low engineering costs, high speed, and simplicity compared to low-pressure (vacuum) plasma techniques. Another advantage from an industrial viewpoint is that continuous in-line processing can easily be performed. The control of external plasma operational parameters, such as frequency of discharges, exposure time and flow rate of the monomer makes this technique very promising for modifying the surface chemistry and topography of henequen fibers, which can thereby be tuned to design henequen surfaces compatible with high density polyethylene. In this work we used DBD treatments with ethylene at atmospheric pressure to modify the surface properties of henequen fibers (HF), (*Agave fourcroydes*) and the main goal was to improve their adhesion to HDPE. A $2^3$ factorial experimental design was used to study the effects of the plasma parameters, frequency, flow rate and exposure time, onto the HF tensile mechanical properties and its adhesion to High Density Polyethylene (HDPE). The chemical functionalization and topography of the surfaces were analyzed by means of PAS-FTIR and SEM to better understand the surface modification.

## 2. Experimental

### 2.1. Materials

Henequen fibers with an average diameter of 180 μm and average length of 9 cm, supplied by Desfibradora Yucateca, S.A. (DESFIYUSA Co.) of Mérida, Yucatán, México were used. High density polyethylene, HDPE (Petrothene) extrusion grade, was supplied by Quantum Chemical Inc. A melt flow index of 0.33 g/10 min was determined using ASTM standard D-1238-79 at 190°C and a weight

of 2160 g. A density of 0.96 g/cm$^3$ was determined using ASTM standard D-792-86 and benzene as an immersion liquid. The melting point (135°C) was determined in a DSC-7 Perkin Elmer calorimeter. Ethylene ($C_2H_4$) (99%, INFRA, Guadalajara, Mexico) and UHP Helium (99.99%, INFRA, Guadalajara, Mexico) were used as received without further purification.

### 2.2. Plasma treatments and design of experiments

#### 2.2.1. Dielectric barrier discharge treatments

Dielectric barrier discharges were generated in a parallel-plate reactor prototype described elsewhere [29]. In a typical treatment, once the discharge gap and the frequency had been selected, 9 cm long henequen fibers were vacuum-oven dried, (60°C, 135 Torr, 12 h) and placed on the reactor, and then, the reactor was closed. Helium was allowed to flow (2 L/min) for a period of 5 min to free the reactor chamber from air and other impurities. The ethylene reagent was then fed for 3 min and then the discharge was ignited, selecting both flow and time of discharge according to the experimental design. All the reactions were carried out at atmospheric pressure and room temperature (25°C). The reagent was allowed to flow for one more minute in order to quench the free radicals, and helium was fed again at 2 L/min for 5 min to evacuate the reaction chamber. The henequen samples were collected and stored (overnight) in plastic bags until ready for further analysis. Xylene extraction of henequen fibers in a Soxhlet apparatus for 6 h after the ethylene-plasma treatments was carried out at 120°C for 12 h in order to make sure that the deposited layers could not be easily removed by physical or chemical means.

#### 2.2.2. Statistical experimental design

A common method used to investigate the effects of the values of the operational parameters (factors) on a process is the usual approach of changing the value of one factor at a time and noting its influence on a given characteristic of the final product (response). However, this method has some disadvantages: it requires a large number of trials and it does not reveal the possible interactions between factors. In contrast, factorial experimental designs can be efficient when several factors (more than two) are under study. By factorial design, it means that in each complete trial all possible combinations of the levels of the factors are investigated. The factors are commonly used at two levels. Normally, it is assumed that the response is approximately linear over the range of the factor level chosen. In a two-level factorial design a ($2^k$ factorial design), it is understood that the measured property $y$ (the response of the system) can be related with the experimental variables through the polynomial first order regression model shown in Equation (1):

$$y = b_0 + b_1X_1 + b_2X_2 + b_3X_3 + b_{12}X_1X_2 + b_{13}X_1X_3 + b_{23}X_2X_3 + b_{123}X_1X_2X_3 + \varepsilon \quad (1)$$

where, $X_i$ is the coded values of the considered factors.

A two-level full factorial design $2^3$ with five central points was employed to investigate the effects of the external plasma operational parameters: frequency of discharges ($A$), plasma exposure time ($B$) and the flow rate of ethylene ($C$) over the tensile mechanical properties of henequen fibers and the Interfacial Shear Strength (IFSS) between henequen fibers and the HDPE. The levels of the three independent variables studied are indicated in Table I. They were selected on the basis of preliminary studies of this polymerization system [29].

For the convenience of handy data processing and to simplify calculation of the regression coefficients, the independent variables investigated were re-coded so as to give normalized variables varying within the range of [–1, 1]. Thus, if $A$ denotes the natural variable plasma frequency; $B$ the natural variable exposure time of the fiber and $C$ the ethylene flow rate, then the coded variables are calculated as Equation (2):

$$X_1 = \frac{A - 145\ \text{Hz}}{25\ \text{Hz}},\ X_2 = \frac{B - 4.5\ \text{min}}{3.5\ \text{min}},$$
$$X_3 = \frac{C - 0.604\ \text{L/min}}{0.414\ \text{L/min}} \quad (2)$$

The standard experimentation matrix is shown in Table 2. Columns 2 to 4 give the variable levels

**Table 1.** Levels of factors in experimental design

| Levels | Factor | | |
|---|---|---|---|
| | Frequency (A) [Hz] | Exposure time (B) [min] | Flow rate (C) [L/min] |
| Lower (–1) | 120 | 1.0 | 0.204 |
| Higher (+1) | 170 | 8.0 | 1.018 |

**Table 2.** Experimental variables in the factorial experimental design $2^3$ with five central points

| Run (Standard order) | $X_1$ | $X_2$ | $X_3$ | A [Hz] | B [min] | C [L/min] | Tensile strength [MPa] | Tensile modulus [MPa] | IFSS [MPa] |
|---|---|---|---|---|---|---|---|---|---|
| 1 | –1 | –1 | –1 | 120 | 1.0 | 0.204 | 350.0 | 12.3 | 2.40 |
| 2 | +1 | –1 | –1 | 170 | 1.0 | 0.204 | 340.0 | 12.0 | 3.00 |
| 3 | –1 | +1 | –1 | 120 | 8.0 | 0.204 | 345.0 | 12.6 | 2.42 |
| 4 | +1 | +1 | –1 | 170 | 8.0 | 0.204 | 335.0 | 12.4 | 2.30 |
| 5 | –1 | –1 | +1 | 120 | 1.0 | 1,018 | 400.0 | 13.0 | 2.65 |
| 6 | +1 | –1 | +1 | 170 | 1.0 | 1.018 | 380.0 | 12.7 | 2.35 |
| 7 | –1 | +1 | +1 | 120 | 8.0 | 1.018 | 320.0 | 12.5 | 3.50 |
| 8 | +1 | +1 | +1 | 170 | 8.0 | 1.018 | 310.0 | 12.7 | 2.60 |
| 9 | 0 | 0 | 0 | 145 | 4.5 | 0.611 | 365.0 | 12.8 | 2.64 |
| 10 | 0 | 0 | 0 | 145 | 4.5 | 0.611 | 367.0 | 12.7 | 2.63 |
| 11 | 0 | 0 | 0 | 145 | 4.5 | 0.611 | 362.0 | 12.7 | 2.67 |
| 12 | 0 | 0 | 0 | 145 | 4.5 | 0.611 | 364.0 | 12.1 | 2.62 |
| 13 | 0 | 0 | 0 | 145 | 4.5 | 0.611 | 363.0 | 12.7 | 2.60 |

coded in the dimensionless coordinate while as columns 5 to 7 give the natural variable levels.

A statistical analysis of the data was performed using the commercial software *Design Expert 7*, (Stat-Ease, Inc., Minneapolis, MN, USA). The analysis of variance (ANOVA) provided a study of the variation present in the results of the experiments carried out and the test of statistical significance, *p*-value, was determined according to the total error criteria considering a confidence level of 95%. The influence of a factor is considered significant if the value of the critical level ($p$) is lower than 0.05; discarding the meaningless parameters for *p*-values over 0.05 [30]. An empirical regression model encompassing all the operating variables and their binary interactions was calculated for the dependent variables, tensile strength, tensile modulus and IFSS between henequen fiber and HDPE.

## 2.3. Mechanical properties

### 2.3.1. Tensile srength test

Single-fiber tensile tests were conducted according to ASTM D3822-01 to determine the tensile strength of treated and untreated henequen fibers using a Shimadzu universal testing machine, Model AGS-X. A single fiber was selected and cut to a length of 30 mm. The diameter of each henequen fiber tested was measured at several points along its length using an optical microscope Motic Digital Microscope DMI 43 before the test. The henequen fibers were conditioned at 60% RH and a temperature of 25°C before they were tested. The gauge length was 12.5 mm and the cross-head speed was set to 1 mm/min. The results of 15 single fiber tests were evaluated in terms of tensile strength, tensile modulus and elongation at break.

### 2.3.2. Interfacial shear strength test (pull-out test)

To measure the IFSS the pull-out test was used. In this test, one end of the fiber is embedded in a block of the polymer matrix and a force is applied to the free end to pull it out of the matrix while the force is continuously monitored and recorded. The average IFSS can be calculated from the force at which the debonding occurs using Equation (3):

$$\tau = \frac{F}{\pi d l} \tag{3}$$

where $F$ is the maximum load measured prior to debonding of the fiber, $d$ is the fiber diameter and $l$ is the fiber embedded length [11, 14, 31, 32].

### 2.3.3. Preparation of the pull-out test sample

The pull-out specimens were made using the following procedure: the henequen fibers were attached to a frame using high temperature adhesive tape. Then, they were placed between two sheets of HDPE and the mold was subjected to a 1 ton constant pressure at 180°C, in a Carver laboratory press for 10 minutes and then cooled to room temperature under constant pressure. The specimens were cut in rectangles of 3 cm×1 cm in such a way that one end of the fiber was embedded along the main axis of the rectangle. The nominal fiber embedded length was produced by perforating the sample at a specified position. The actual embedded length and the apparent diameter of the fiber of each probe were recorded with a Motic Digital Microscope DMI 43 (Cole

Parmer Int., Vernon Hills, IL, USA) optical microscope. The specimens were subjected to a tensile force using a MINIMAT (Rheometric Scientific Inc., Piscataway, NJ., USA) miniature testing machine equipped with a 500 N load cell and the load-displacement curve was recorded using a cross-head speed of 1.2 mm/min. in all the experiments.

### 2.4. Surface characterization

#### 2.4.1. Infrared spectroscopy (FTIR)

The henequen fibers were cut to an average length of 1.5 mm and then a FTIR analysis was performed on a Nicolet model Protege 460 Magna IR (Nicolet Inst. Corp., Madison, WI, USA) spectrometer using a Photoacoustic attachment (MTEC Photoacoustics, Inc., Ames, IA, USA). The spectra were recorded with 60 scans, 4 $cm^{-1}$ resolution a speed of 0.15 cm/s.

#### 2.4.2. Scanning electron microscopy (SEM)

The henequen fibers were coated with gold and then analyzed using a JEOL JSM-6360LV (JEOL de Mexico, D.F, MX) scanning electron microscope operated at 20 keV.

## 3. Results and discussion

### 3.1. Surface characterization

#### 3.1.1. SEM analyses

The surface morphology of the ethylene-plasma treated henequen fibers at different conditions of external operational parameters (frequency, exposure time, flow rate) of atmospheric pressure DBD ethylene-plasma are shown in Figure 1a–1d.

As it can be seen, the untreated fiber surface is relatively more homogeneous than the ethylene-plasma treated fibers. It can also be seen that there are some changes in the fiber topography that suggest an increment in fiber roughness and the formation of tiny cracks or cavities for the plasma treated fibers at conditions (120, 1.0, 1.018), see Figure 1b, compared with the untreated ones displayed in Figure 1a. A rougher surface morphology and several defects in the form of cracks, pits and corrugations are pro-

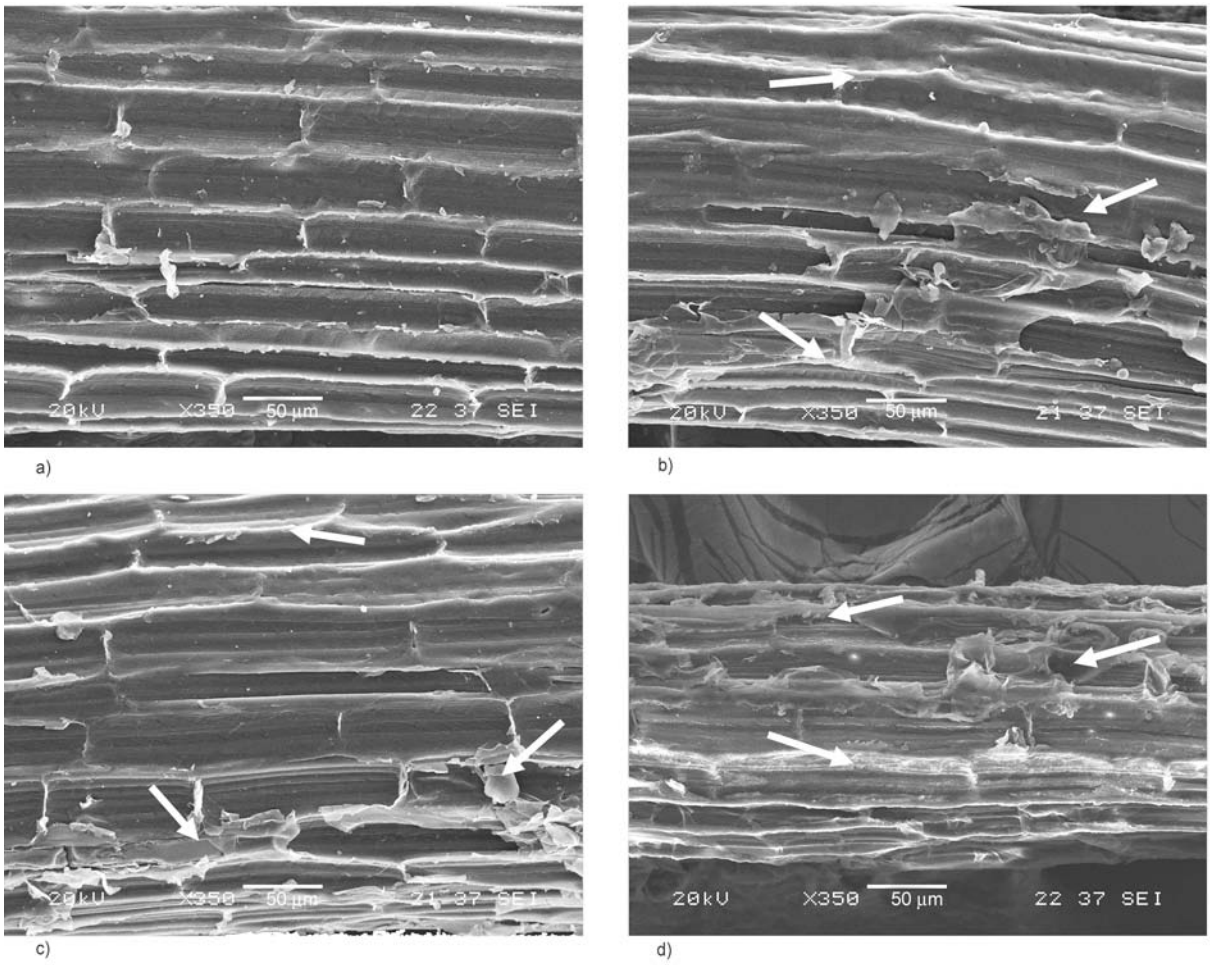


**Figure 1.** SEM micrograph (×350) showing the longitudinal section of henequen fibers (a) untreated; ethylene-plasma treated: (b) (120, 1.0, 1.018); (c) (170, 1.0, 1.018) and (d) (170, 8.0, 1.018)

duced in the fibers treated at (170, 1.0, 1.018) can be seen in Figure 1c. It is notorious that the increment in the frequency of discharges, results in an increase of the deterioration of the fiber surface because they are exposed to a greater amount of energy during its residence time on the DBD reactor. Also, the effect of exposure time on the fiber surface topography is evident in Figure 1d where it can be seen that the deterioration of the fiber surface is more severe for the fibers exposed during 8 min to the plasma discharges (170, 8, 1.018). A large amount of crevices and torn microfibrils are evident because the longer the time of treatment, the more severe is the etching of the fiber surface than that resulting from the increase in the frequency of the discharge. These surface modifications are evident if Figures 1c and 1d are compared. Furthermore, Figures 1b–1d also depict the presence of a thin layer of material (shown with arrows) indicating that exposure of the fibers to the ethylene plasma, induced the formation of a polymeric film. The amount of polymer deposited seems to be larger with the time of exposure (compare Figure 1b to Figure 1d) than with an increment in the frequency of discharge (compare Figure 1b to Figure 1c).

### 3.2. FTIR analyses

Figure 2 shows the infrared spectra of the ethylene-plasma treated curve (a); the untreated henequen fiber curve (b) and the difference between them curve (c). In Figures 2 curve (a, b) it can be seen that both spectra, the untreated and the ethylene-plasma

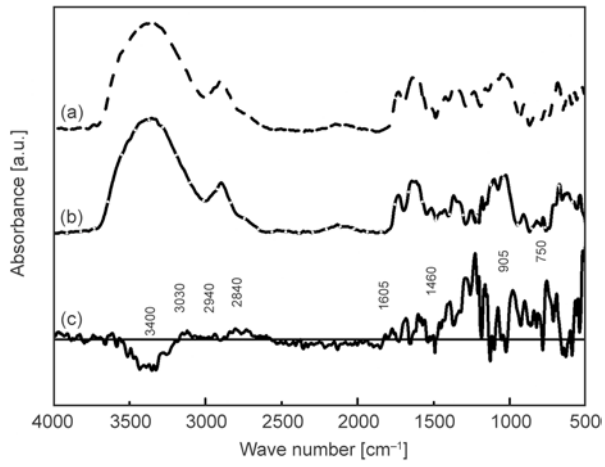


**Figure 2.** PAS-FTIR spectra of untreated and plasma treated henequen fibers. (a) Plasma treated (120, 1.0, 1.018); (b) untreated (pristine) fiber and (c) difference (a)–(b) spectrum.

treated henequen fibers, are very similar and shows the absorbance peaks related to the characteristic functional groups of a lignocellulosic fiber. The broad and intense peak at 3400 $cm^{-1}$ suggests hydrogen-bonded O–H stretching vibration from the cellulose and the lignin and to the water present on the fiber. The bands in the range 2800–3000 $cm^{-1}$ are related to C–H saturated hydrocarbon stretching. The shoulder at about 1730 is due to the carbonyl (C=O) stretching of acetyl groups of hemicellulose. The broad band around 1000–1300 $cm^{-1}$ has been attributed to the C–O–C stretching vibration of cellulose and hemicellulose. [33, 34]. A more detailed analysis shows that definitely there are some differences between the spectra of the fibers processed in the plasma reactor and the untreated ones. In order to highlight these differences the subtraction of both spectra is plotted in Figure 2 curve (c).

It can be observed that there are changes in the 3000–3500, 2800–3000 $cm^{-1}$, and around 1600, 1460, 900 and 750 $cm^{-1}$. The decrease in the 3400 peak could be attributed to the reduction of the O–H hydrogen bonds in the surface of the fiber due to an increment in its hydrophobicity, attributed to the deposition of a hydrocarbon polymeric film, formed during the exposure to the ethylene-plasma. The appearance of the peaks at 2940 $cm^{-1}$ (asymmetric stretching) and 2840 $cm^{-1}$ (symmetric stretching), the peak at 1460 $cm^{-1}$ (bending) and the peak at 750 $cm^{-1}$ (rocking deformation) of methylene group ($–CH_2–$) suggest the presence of a hydrocarbon film on the henequen fiber surface. Moreover, the peaks at 3030, 1605 and at 905 $cm^{-1}$ could be attributed to the existence of vinyl groups in the deposited film [35, 36]. Tibbit *et al*. [37], Donohoe and Wydeven [38], Oran *et al.* [39] and Swaraj *et al.* [40] have pointed out that the plasma polymerization of ethylene yields a plasma-polyethylene polymer with different structural characteristics with respect to that obtained with conventional methods. The plasma-polyethylene polymer possesses chemical crosslinks, ramifications and unsaturated vinyl groups.

### 3.3. Fiber tensile test results

The determination of tensile properties of henequen fibers is crucial because it gives a measure of how much improvement in mechanical properties can be expected when the fibers are incorporated in a polymer matrix. The sensitivity of henequen fibers to moisture content has been reported in the technical

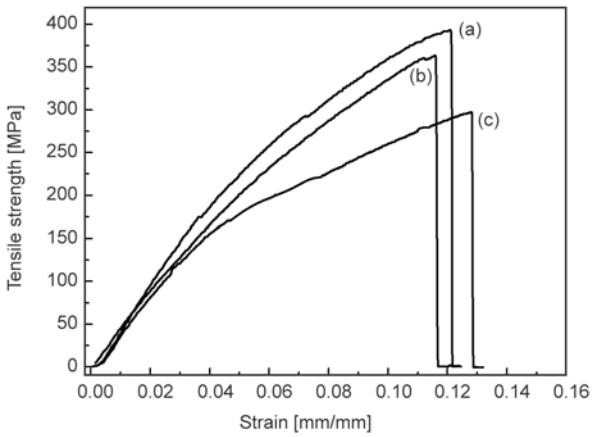


**Figure 3.** Typical stress-strain behavior of henequen fibers: (a) untreated; ethylene-plasma treated: (b) (120, 1.0, 1.018) and (c) (170, 8, 1.018)

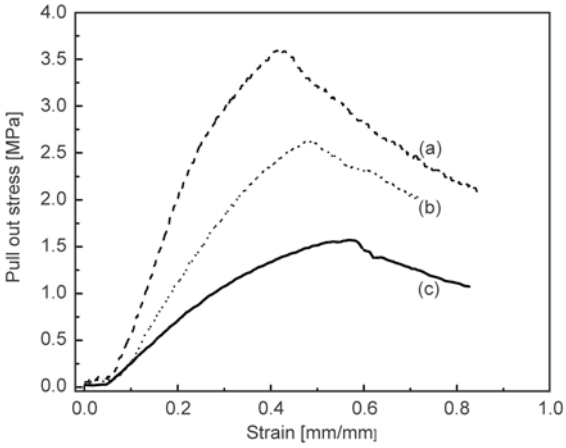


**Figure 4.** Typical average interfacial shear stress-strain behavior of henequen fibers subjected to different ethylene-plasma treatments: (a) (120, 1.0, 1.018); (b) (170, 1.0, 0.204) and (c) untreated

literature and it is known that the variation in moisture content can affect the tensile properties of fibers. Therefore, the fibers tested for tensile properties were equilibrated at 25°C and 60% relative humidity (RH) before the testing. The typical stress-strain curve of henequen fiber in tensile testing is shown in Figure 3. The curves presented a non-linear region starting at stress levels of 50 MPa or below. This non-linear region, following the initial portion of the stress–strain curve has been hypothesized to be due to a collapse of the weak primary cell walls and delamination between fiber-cells [10].

The knowledge of the internal structure of a henequen fiber [10] allows for the elaboration of an interpretation of its deformation mechanisms. The first linear zone of the stress-strain curve corresponds to a global loading of the cell walls. The curved zone can be associated to a visco-elasto-plastic deformation of the amorphous parts of the fiber together with an alignment of the cellulose microfibrils with the fiber axis. Finally, after this rearrangement, the third linear zone could be characteristic of the elastic deformation of the microfibrils. Ethylene-plasma treated fibers show a drop in the tensile strength and elongation at break that can be partially linked to the introduction of defects (e.g., cracks and pits) onto the surface of the fibers after plasma treatment, the longer the exposure to the plasma treatment the higher the flaw population.

### 3.4. Interfacial shear strength test (pull out test) results

The typical load-displacement curves for the pristine henequen fiber and subjected to two different conditions on the ethylene-plasma reactor in the pull-out test are shown in Figure 4. It can be noted that all the curves exhibit the non-linear behavior characteristic of a ductile matrix [41].

However, once the load reaches its maximum value there are clearly significant differences in the way these curves drop. For the pristine henequen it can be seen that the load increases gradually and when it reaches a maximum value there is a smooth transition and it begins to decrease in a linear fashion until the total embedded length of the fiber is pulled-out. This behavior agrees well with the behavior of a poor interphase that results because of the incompatibility between the hydrophilic fiber and the hydrophobic matrix. This behavior shows a slight change in the case of the henequen fibers treated at (170, 1.0, 0.204) because the higher the roughness of the plasma treated fiber the better the fiber-matrix mechanical interlocking, i.e., the fiber-matrix interaction is improved. For the (120, 1.0, 1.018) treated fiber, the load-displacement curve depicts better bonded interphase; after the interphase has failed, the fiber can still be extracted in a controlled way and friction was measured until the fiber was completely pulled-out. This behavior suggests a better fiber-matrix interlocking and to the possible interaction between the hydrocarbon film deposited onto the surface with the HDPE matrix [11, 14–16, 18–20].

Henequen fibers are polar hydrophilic lignocellulosic fibers because they have a chemical composition consisting of cellulose (70% w/w), hemicellulose (20% w/w), lignin (8%) and extractives (2%). Cellulose consists of long chains of anhydro-D-glu-

copyranose units each bearing three hydroxyl groups (one primary and two secondary moieties), with the exception of the terminal ones. Valadez-Gonzalez *et al.* [9] have pointed out that pristine surface henequen fibers possess both acidic and basic sites since the surface acid-base characteristics of cellulose and lignin are different. While cellulose is strongly acidic, lignin is more evenly bipolar, with a much weaker acidity and a similar basicity than cellulose. The acetyl groups in the hemicelluloses also contribute to the basic character of the henequen fibers. On the other hand, High density Polyethylene is a non-polar hydrophobic thermoplastic matrix due to the lack of reactive groups on its backbone chains and therefore only can interact by non-dispersive Van der Waals forces. Therefore, the adhesion between henequen fibers and HDPE is expected to be poor at the interface because of the different polarity. It is known that the surface treatments modify the fiber surface energy and so the nature of the fiber-matrix interphase. Several reports in the literature pointed out that the chemical surface treatment modifies the fiber surface free energy, i.e., it changes the surface dispersive and non-dispersive energies. Wettability, by a HDPE matrix, of henequen fibers can be improved by the action of ethylene plasma treatments, due to the reduction of the polar components of surface energy. The plasma-polymerized structure is usually complex but it is known that ethylene-based plasma-polymerized structures are highly branched crosslinked and that they contain some degree of unsaturation [37].

### 3.5. Factorial design analysis

The experimental values obtained for the selected responses tensile strength, tensile modulus and interfacial shear strength (IFSS) are presented in Table 2.

#### 3.5.1. Model fitting and statistical analysis

The half-normal probability plot for tensile strength and tensile modulus of henequen fibers and the related to the henequen-HDPE IFSS are shown in Figures 5a, 5b and 6 respectively.

The half-normal probability plot is a graphical tool that uses the ordered estimated effects to help assess which factors are important and which are unimportant. From the half-normal probability plot of |effects| we should be able to identify the most important factors since the estimated |effect| of an unimportant factor will typically be on or close to a near-zero line, while the estimated |effect| of an important factor will typically be displaced well off the line. As can be seen in Figures 5a and 5b the exposure time is the most important plasma operational parameter for both tensile strength and modulus. Followed by the interaction time×flow rate; the frequency of discharge and last, the ethylene flow rate.

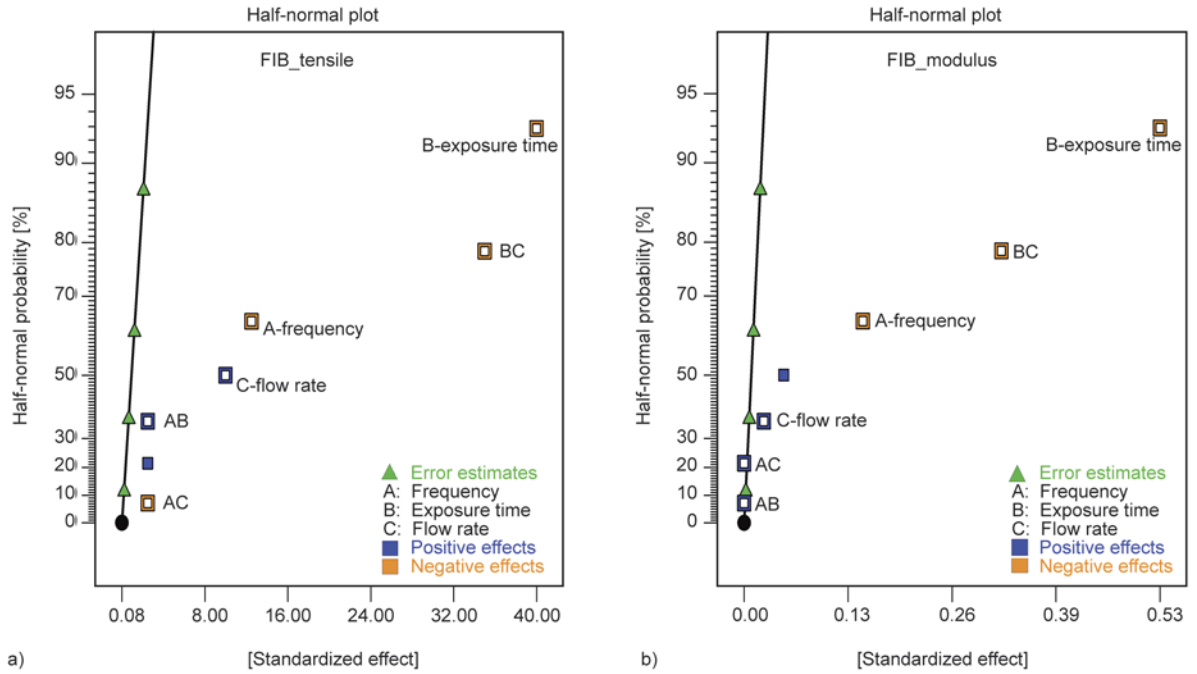


**Figure 5.** Half-normal probability plot showing the effects of plasma operational parameters on tensile properties of henequen fibers: (a) tensile strength and (b) tensile modulus

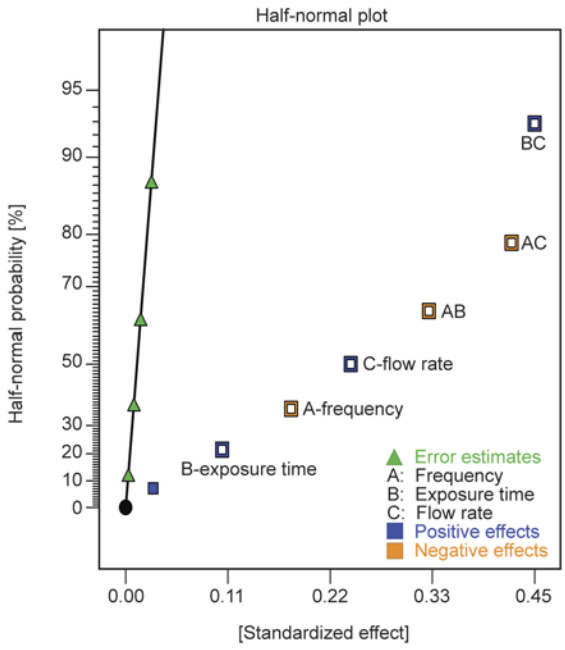


**Figure 6.** Half-normal probability plot showing the effects of plasma operational parameters on Henequen-HDPE Interfacial Shear Strength (IFSS)

In the case of the IFSS, Figure 6, the three plasma operational parameters studied are significant. However it can be seen that the interaction time×flow rate is the most important whereas the frequency of discharges is the most important among the main effects.

The empirical relationships for tensile strength and tensile modulus as determined by Design-Expert software are shown in Equations (4), (5) and (6) below after eliminating the non-significant main effects and interaction terms:

$$\text{FIB\_TENSILE} = 347.5 - 6.25A - 20.0B + 5.0C - 17.5BC \quad (4)$$

$$\text{FIB\_MODULUS} = 12.46 - 0.075A - 0.26B - 0.16BC \quad (5)$$

$$\text{IFSS\_FIBPLASMA} = 2.63 - 0.071A + 0.07B + 0.10C - 0.16AB - 0.19AC + 0.24BC \quad (6)$$

The goodness of the regression model can be assessed because the excellent agreement between the experimental values and the predicted by the model as can be observed in the Figures 7a, 7b and

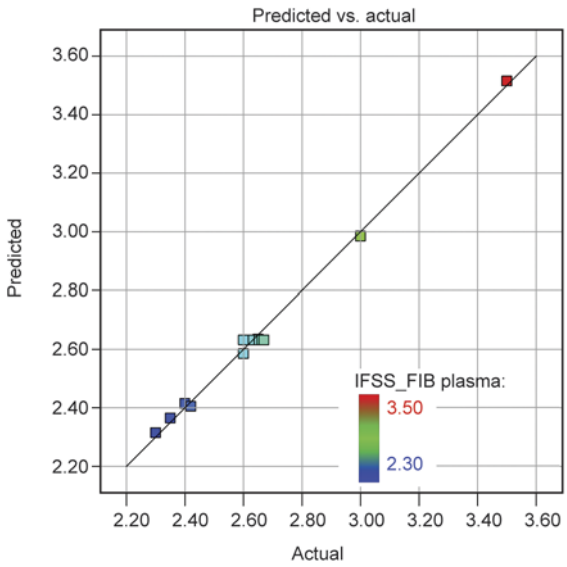


**Figure 8.** Scatter diagram of predicted response vs. actual response for interfacial shear strength of ethylene-plasma treated henequen fibers-HDPE

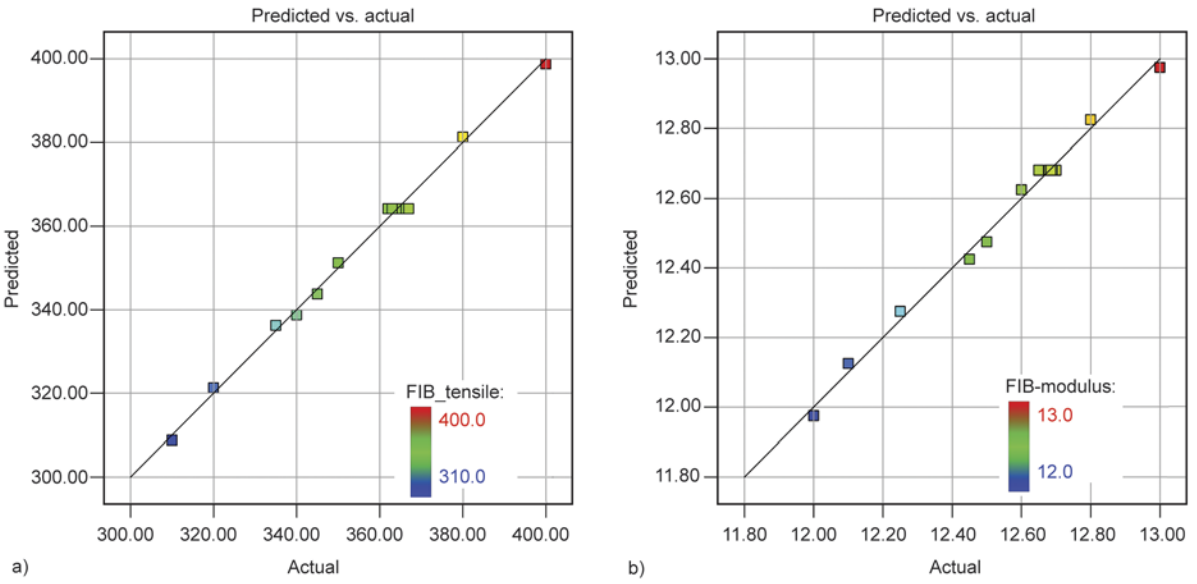


**Figure 7.** Scatter diagram of predicted response vs. actual response for (a) tensile strength and (b) tensile modulus of ethylene-plasma treated henequen fibers

for henequen fibers tensile strength and modulus respectively, and in Figure 8, for henequen-HDPE IFSS.

### 3.5.2. Response surface plot and contour plot analyses of tensile strength and modulus

The response surfaces and contour plots are the graphical representations of regression equation. They provide a method to visualize the relationship between the response and each variable, and the interactions between any two tested variables. The fitted response surface plot was generated by statistically significant above model by Design-Expert program to understand the interaction of the operational plasma parameters selected (independent variables) on the tensile mechanical properties of henequen fibers and their interfacial shear strength with HDPE. The plots are shown in Figures 9–11 and were obtained from Equations (4), (5) and (6) respectively. Two parameters of each model were plotted at any one time on the *X* and *Y* axes with the response variable (tensile strength, modulus or IFSS) in *Z* axis. The other remaining parameter was set constant. The shape of the contour plots (straight or curved) indicates whether the mutual interactions between variables are significant or not. A straight contour plot indicates that the interactions between related variables are negligible. A curved contour plot indicates that the interactions between related variables are significant. Analyses of the response surfaces and their respective contour plots allowed us to conveniently investigate the interactions between any two variables, and locate the optimum ranges of the variables efficiently such that the response was maximized. The contour plot and the corresponding surface plot for tensile strength [MPa] of ethylene-plasma treated henequen fibers, as a function of the exposure time [min] and the ethylene-flow rate [L/min] are shown in Figures 9a and 9b.

In Figure 9a it is observed that the highest fiber tensile strength was obtained at high flow rates and short exposure times. On another hand, the lowest fiber tensile strength value is found at high exposure times and high flow rates. This behavior highlights the importance of interaction between the operational parameters since the effect of flow rate depends on exposure time. At short times, (1 min), it increases the fiber strength whereas at longer times, (8 min), it decreases the fiber strength. We can observe how this strong interaction results in a 'twisting' of the surface response. Another fact that can be observed in Figure 9 is that the rate of change of the tensile strength is higher at short times compared with larger times, e.g. the sensibility of the process is greater at short times and more robust at longer ones.

The contour plot and the corresponding surface plot for tensile modulus [MPa] of ethylene-plasma treated henequen fibers, as function of exposure time [min] and ethylene-flow rate [L/min] are shown in Figures 10a and 10b. The general behavior of the tensile modulus is similar to that of tensile strength, i.e. the higher moduli were obtained at short times of exposure and high flow rates; the smaller moduli were found at longer times and high flow rates. However the interaction between both operational parameters, time of exposure and flow rate is weak as can be seen the more straight contour lines in Figure 10a. The corresponding surface plot is slightly

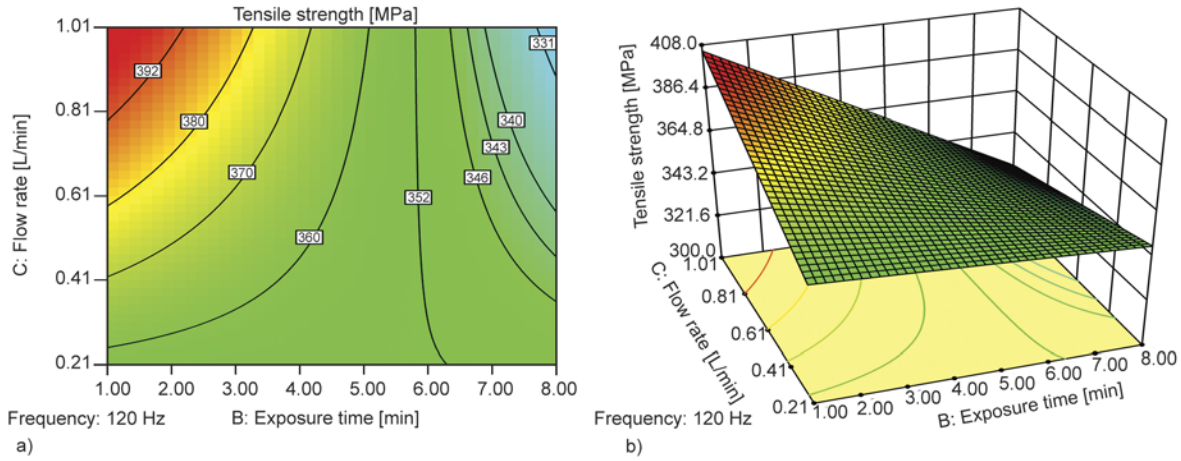


**Figure 9.** Contour plot (a) and the corresponding surface plot (b) of tensile strength of ethylene-plasma treated henequen fibers

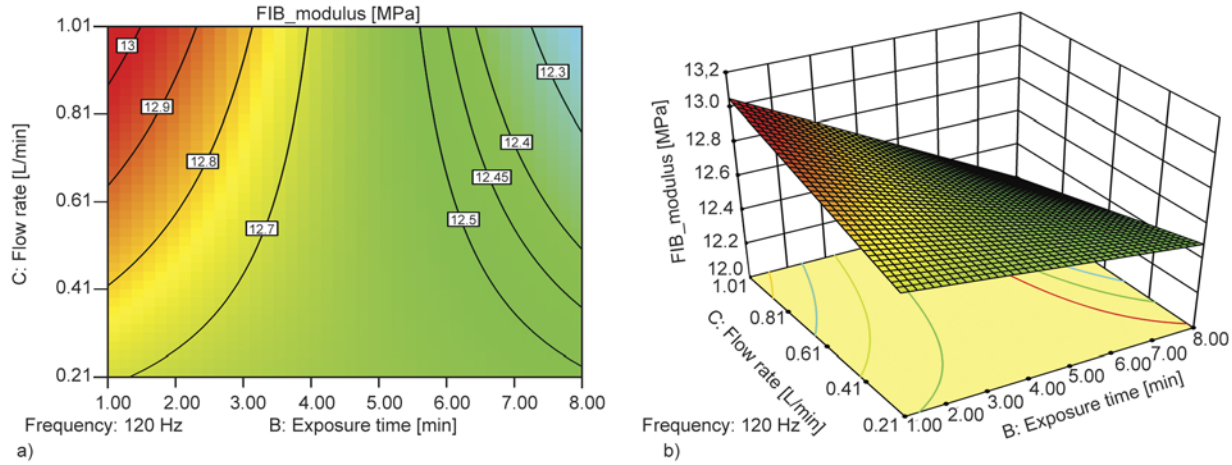


**Figure 10.** Contour plot (a) and the corresponding surface plot (b) of tensile modulus of ethylene-plasma treated henequen fibers

twisted and the rate of change of property is similar at short and high exposure times. For the tensile modulus concern, it seems that the process is robust. In other words the reactor condition for ethylene-plasma treatments slightly affects the henequen fiber modulus. The contour plot and the corresponding surface plot for interfacial shear strength [MPa] between henequen fiber and the HDPE tensile strength [MPa] of ethylene–plasma treated henequen fibers, as a function of exposure time [min] and ethylene-flow rate [L/min] are shown in Figures 11a and 11b. In Figure 11a it is observed that the higher IFSS (3.5 MPa) between the ethylene-plasma henequen fibers and HDPE is accomplished at low frequency of discharges, high flow rate of ethylene and longer exposure times. On another hand, the smaller values of IFSS (2.3 MPa) were obtained at high frequency, longer exposure times and low flow rates. From these results it can be seen that we can improve the IFSS by approximately 50% with a suitable choice of operational parameters of DBD plasma reactor. The contour lines shown in Figure 11a are curved, as can be expected, because the interaction flow rate-exposure time is statistically significant. Accordingly the surface response is twisted and shows a complex behavior at slow flow rates and short exposure times. Another fact that can be observed in Figure 11a is that the rate of change of IFSS is greater at longer exposure times than at short ones.

For example, increasing the ethylene flow rate from 0.21 to 1 L/min, it increases the IFSS from 2.4 to 2.46 MPa (2.5%) at exposure times of 1 min, whereas it increases from 2.43 to 3.4 MPa (40%) at exposures time of 8 min.

## 4. Conclusions

In order to improve the bonding between henequen fibers and High Density Polyethylene their surface modification was realized by exposing them to eth-

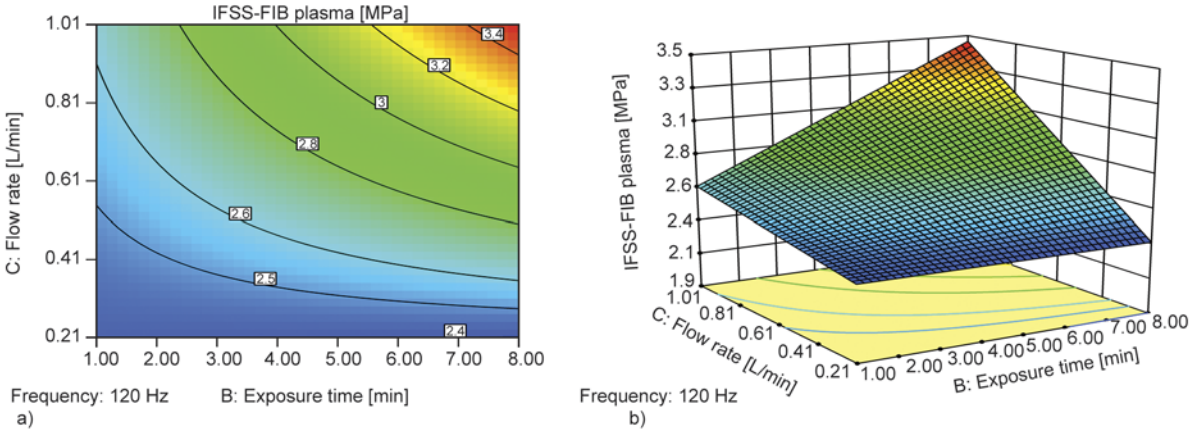


**Figure 11.** Contour plot (a) and the corresponding surface plot (b) for Interfacial shear strength of ethylene-plasma treated henequen fibers-HDPE

ylene dielectric barrier discharge (DBD) plasma operating at atmospheric pressure. The present study indicates that individual operational parameters in DBD plasma treatment have different effects on the properties of henequen fibers and on its bonding with HDPE. The statistical analysis approach used here has determined that the chosen plasma operational parameters, frequency of discharges, exposure time and ethylene flow rate, have a selective effect on the nature and scale of the polymer modification that occurs in each case. The results shows that the conditions on the plasma reactor leads to a significant change in bonding between henequen fibers and HDPE as determined by the IFSS determined by means of the pull-out test. It was also found that the interactions between, exposure time-flow rate and frequency-flow rate, have more impact on the IFSS. The processing conditions that improve the IFSS to a great extent were frequency 120 Hz, exposure time 8 min and ethylene flow rate 1.018 L/min. Also, if a frequency 170 Hz, exposure time 8 min and flow rate 0.204 L/min had been chosen, the IFSS would have dropped to its minimum value. The SEM results show that the exposure to plasma modifies the morphological properties of the fibers increasing their roughness. The FTIR results suggest the presence hydrocarbon-like polymer film, with some vinyl groups, that, it could react with the HDPE, deposited onto the fibers. These findings suggest that the improvement in the henequen-HDPE bonding could be the result of enhancing the mechanical interlocking, due the increment in roughness, and the possible reaction of the vinyl groups present in the hydrocarbon-like polymer film deposited onto the fiber.

## Acknowledgements

The authors would like to thank Ms. I.Q. Silvia Beatriz Andrade Canto for the SEM micrographs and to M. en C. Javier Iván Cauich Cupul for assistance with the pull-out testing. The authors would also like to thank the support of the Bilateral Cooperation Mexico (CONACYT) Hungary (HAS) Program through grant No. 193207.

## References

[1] Li X., Tabil L. G., Panigrahi S.: Chemical treatments of natural fiber for use in natural fiber-reinforced composites: A review. Journal of Polymers and the Environment, **15**, 25–33 (2006).
DOI: 10.1007/s10924-006-0042-3

[2] Saheb D. N., Jog J. P.: Natural fiber polymer composites: A review. Advances in Polymer Technology, **18**, 351–363 (1999).
DOI: 10.1002/(SICI)1098-2329(199924)18:4<351::AID-ADV6>3.0.CO;2-X

[3] Biagiotti J., Puglia D., Torre L., Kenny J. M., Arbelaiz A., Cantero G., Marieta C., Llano-Ponte R., Mondragon I.: A systematic investigation on the influence of the chemical treatment of natural fibers on the properties of their polymer matrix composites. Polymer Composites, **25**, 470–479 (2004).
DOI: 10.1002/pc.20040

[4] Kalia S., Thakur K., Celli A., Kiechel M. A., Schauer C. L.: Surface modification of plant fibers using environment friendly methods for their application in polymer composites, textile industry and antimicrobial activities: A review. Journal of Environmental Chemical Engineering, **1**, 97–112 (2013).
DOI: 10.1016/j.jece.2013.04.009

[5] Reddy M., Vivekanandhan S., Misra M., Bhatia S., Mohanty A. K.: Biobased plastics and bionanocomposites: Current status and future opportunities. Progress in Polymer Science, **38**, 1653–1689 (2013).
DOI: 10.1016/j.progpolymsci.2013.05.006

[6] Neves Monteiro S., Duarte Lopes F., Paula Barbosa A., Barreto Bevitori A., Da Silva I. L. A., Lopes Da Costa L.: Natural lignocellulosic fibers as engineering materials – An overview. Metallurgical and Materials Transactions A, **42**, 2011–2963 (2011).
DOI: 10.1007/s11661-011-0789-6

[7] Sobczak L., Brüggemann O., Putz R. F.: Polyolefin composites with natural fibers and wood-modification of the fiber/filler–matrix interaction. Journal of Applied Polymer Science, **127**, 1–17 (2013).
DOI: 10.1002/app.36935

[8] Ho M-P., Wang H., Lee J-H., Ho C-K., Lau K-T., Leng J., Hui D.: Critical factors on manufacturing processes of natural fibre composites. Composites Part B: Engineering, **43**, 3549–3562 (2012).
DOI: 10.1016/j.compositesb.2011.10.001

[9] Valadez-Gonzalez A., Moreno-Chulim M. V., Herrera-Franco P. J.: Modification of the fibre surface for the optimisation of mechanical properties in natural-fibre reinforced polymers. International Journal of Materials and Product Technology, **36**, 417–430 (2009).
DOI: 10.1504/IJMPT.2009.027846

[10] Cazaurang Martinez M. N., Herrera-Franco P. J., Gonzalez-Chi P. I., Aguilar-Vega M.: Physical and mechanical properties of henequen fibers. Journal of Applied Polymer Science, **43**, 749–756 (1991).
DOI: 10.1002/app.1991.070430412

[11] Valadez-González A., Cervantes-Uc J. M., Olayo R., Herrera-Franco P. J.: Effect of fiber surface treatment on the fiber–matrix bond strength of natural fiber reinforced composites. Composites Part B: Engineering, **30**, 309–320 (1999).
DOI: 10.1016/S1359-8368(98)00054-7

[12] Valadez-González A., Cervantes-Uc J. M., Olayo R., Herrera-Franco P. J.: Chemical modification of henequen fibers with an organosilane coupling agent. Composites Part B: Engineering, **30**, 321–331 (1999). DOI: 10.1016/S1359-8368(98)00055-9

[13] Khan M. A., Bhattacharia S. K., Kabir M. H., Chowdhury A. M. S. A., Rahman M. M.: Effect of mercerization on surface modification of henequen (*Agave fourcroydes*) fiber by photo-curing with 2-hydroxyethyl methacrylate (HEMA). Polymer Plastics Technology and Engineering, **44**, 1079–1093 (2005). DOI: 10.1081/PPT-200065184

[14] Herrera-Franco P. J., Valadez-González A.: A study of the mechanical properties of short natural-fiber reinforced composites. Composites Part B: Engineering, **36**, 597–608 (2005). DOI: 10.1016/j.compositesb.2005.04.001

[15] Colom X., Carrasco F., Pagès P., Cañavate J.: Effects of different treatments on the interface of HDPE/lignocellulosic fiber composites. Composites Science and Technology, **63**, 161–169 (2003). DOI: 10.1016/S0266-3538(02)00248-8

[16] George J., Sreekala M. S., Thomas S.: A review on interface modification and characterization of natural fiber reinforced plastic composites. Polymer Engineering and Science, **41**, 1471–1485 (2001). DOI: 10.1002/pen.10846

[17] Corrales F., Vilaseca F., Llop M., Gironès J., Méndez J. A., Mutjè P.: Chemical modification of jute fibers for the production of green-composites. Journal of Hazardous Materials, **144**, 730–735 (2007). DOI: 10.1016/j.jhazmat.2007.01.103

[18] Pang Y., Cho D., Han S. O., Park W. H.: Interfacial shear strength and thermal properties of electron beam-treated henequen fibers reinforced unsaturated polyester composites. Macromolecular Research, **13**, 453–459 (2005). DOI: 10.1007/BF03218480

[19] Lee H. S., Cho D., Han S. O.: Effect of natural fiber surface treatments on the interfacial and mechanical properties of henequen/polypropylene biocomposites. Macromolecular Research, **16**, 411–417 (2008). DOI: 10.1007/BF03218538

[20] Choi H. Y., Han S. O., Lee J. S.: The effects of surface and pore characteristics of natural fiber on interfacial adhesion of henequen fiber/PP biocomposites. Composite Interfaces, **16**, 359–376 (2009). DOI: 10.1163/156855409X450873

[21] Denes F. S., Manolache S.: Macromolecular plasma-chemistry: An emerging field of polymer science. Progress in Polymer Science, **29**, 815–885 (2004). DOI: 10.1016/j.progpolymsci.2004.05.001

[22] Goossens O., Dekempeneer E., Vangeneugden D., Van de Leest R., Leys C.: Application of atmospheric pressure dielectric barrier discharges in deposition, cleaning and activation. Surface and Coatings Technology, **142–144**, 474–481 (2001). DOI: 10.1016/S0257-8972(01)01140-9

[23] Lee H. U., Jeong Y. S., Koh K. N., Jeong S. Y., Kim H-G., Bae J. S., Cho C. R.: Contribution of power on cell adhesion using atmospheric dielectric barrier discharge (DBD) plasma system. Current Applied Physics, **9**, 219–223 (2009). DOI: 10.1016/j.cap.2008.01.014

[24] Fanelli F., Fracassi F., d'Agostino R.: Deposition of hydrocarbon films by means of helium-ethylene fed glow dielectric barrier discharges. Plasma Processes and Polymers, **2**, 688–694 (2005). DOI: 10.1002/ppap.200500057

[25] Heyse P., Dams R., Paulussen S., Houthoofd K., Janssen K., Jacobs P. A., Sels B. F.: Dielectric barrier discharge at atmospheric pressure as a tool to deposit versatile organic coatings at moderate power input. Plasma Processes and Polymers, **4**, 145–157 (2007). DOI: 10.1002/ppap.200600087

[26] de Valence S., Tille J-C., Chaabane C., Gurny R., Bochaton-Piallat M-L., Walpoth B. H., Möller M.: Plasma treatment for improving cell biocompatibility of a biodegradable polymer scaffold for vascular graft applications. European Journal of Pharmaceutics and Biopharmaceutics, **85**, 78–86 (2013). DOI: 10.1016/j.ejpb.2013.06.012

[27] Kaklamani G., Bowen J., Mehrban N., Dong H., Grover L. M., Stamboulis A.: Active screen plasma nitriding enhances cell attachment to polymer surfaces. Applied Surface Science, **273**, 787–798 (2013). DOI: 10.1016/j.apsusc.2013.03.001

[28] Parvinzadeh Gashti M., Hegemann D., Stir M., Hulliger J.: Thin film plasma functionalization of polyethylene terephthalate to induce bone-like hydroxyapatite nanocrystals. Plasma Processes and Polymers, **11**, 37–43 (2014). DOI: 10.1002/ppap.201300100

[29] Toriz G., Gutiérrez M. G., González-Alvarez V., Wendel A., Gatenholm P., de J. Martínez-Gómez A.: Highly hydrophobic wood surfaces prepared by treatment with atmospheric pressure dielectric barrier discharges. Journal of Adhesion Science and Technology, **22**, 2059–2078 (2008). DOI: 10.1163/156856108X332561

[30] Montgomery D. C.: Design and analysis of experiments. Wiley, New Jersey (2005).

[31] Li J-X.: Analysis of the pullout of single fibers from low-density polyethylene. Journal of Applied Polymer Science, **53**, 225–237 (1994). DOI: 10.1002/app.1994.070530211

[32] Stamboulis A., Baillie C., Schulz E.: Interfacial characterisation of flax fibre-thermoplastic polymer composites by the pull-out test. Die Angewandte Makromolekulare Chemie, **272**, 117–120 (1999). DOI: 10.1002/(SICI)1522-9505(19991201)272:1<117::AID-APMC117>3.0.CO;2-9

[33] Matuana L. M., Balatinecz J. J., Sodhi R. N. S., Park C. B.: Surface characterization of esterified cellulosic fibers by XPS and FTIR spectroscopy. Wood Science and Technology, **35**, 191–201 (2001).
DOI: 10.1007/s002260100097

[34] Baltazar-y-Jimenez A., Bistritz M., Schulz E., Bismarck A.: Atmospheric air pressure plasma treatment of lignocellulosic fibres: Impact on mechanical properties and adhesion to cellulose acetate butyrate. Composites Science and Technology, **68**, 215–227 (2008).
DOI: 10.1016/j.compscitech.2007.04.028

[35] Gulmine J. V, Janissek P. R., Heise H. M., Akcelrud L.: Polyethylene characterization by FTIR. Polymer Testing, **21**, 557–563 (2002).
DOI: 10.1016/S0142-9418(01)00124-6

[36] Morrison W. H., Himmelsbach D. S., Akin D. E., Evans J. D.: Chemical and spectroscopic analysis of lignin in isolated flax fibers. Journal of Agricultural and Food Chemistry, **51**, 2565–2568 (2003).
DOI: 10.1021/jf020885t

[37] Tibbitt J. M., Shen M., Bell A. T.: Structural characterization of plasma-polymerized hydrocarbons. Journal of Macromolecular Science: Part A Chemistry, **10**, 1623–1648 (1976).
DOI: 10.1080/00222337608060775

[38] Donohoe K. G., Wydeven T.: Plasma polymerization of ethylene in an atmospheric pressure-pulsed discharge. Journal of Applied Polymer Science, **23**, 2591–2601 (1979).
DOI: 10.1002/app.1979.070230905

[39] Oran U., Swaraj S., Friedrich J. F., Wolfgang U. E. S.: Surface analysis of plasma-deposited polymer films, 3a, in situ characterization of plasma-deposited ethylene films by ToF-SSIMS. Plasma Processes and Polymers, **1**, 141–152 (2004).
DOI: 10.1002/ppap.200400025

[40] Swaraj S., Oran U., Lippitz A., Schulze R-D., Friedrich J. F., Unger W. E. S.: Surface analysis of plasma-deposited polymer films, 4a, In situ characterization of plasma-deposited ethylene films by XPS and NEXAFS. Plasma Processes and Polymers, **2**, 310–318 (2005).
DOI: 10.1002/ppap.200400070

[41] Désarmot G., Favre J-P.: Advances in pull-out testing and data analysis. Composites Science and Technology, **42**, 151–187 (1991).
DOI: 10.1016/0266-3538(91)90016-I

*eXPRESS Polymer Letters Vol.8, No.7 (2014) 505–516*
*Available online at www.expresspolymlett.com*
*DOI: 10.3144/expresspolymlett.2014.54*

# Formation of interfacial network structure via photo-crosslinking in carbon fiber/epoxy composites

*S. H. Deng*[1], *J. J. Zhao*[1], *Q. F. Lin*[2], *C. J. Fan*[1], *X. D. Zhou*[1*]

[1]State Key Laboratory of Chemical Engineering, East China University of Science and Technology, 130 Meilong Road, 200237 Shanghai, PR China
[2]School of Material Science and Engineering, East China University of Science and Technology, 130 Meilong Road, 200237 Shanghai, PR China

*Received 12 January 2014; accepted in revised form 19 March 2014*

**Abstract.** A series of diblock copolymers (poly(n-butylacrylate)-*co*-poly(2-hydroxyethyl acrylate))-*b*-poly(glycidyl methacrylate) ((PnBA-*co*-PHEA)-*b*-PGMA), containing a random copolymer block PnBA-*co*-PHEA, were successfully synthesized by atom transfer radical polymerization (ATRP). After being chemically grafted onto carbon fibers, the photo-sensitive methacrylic groups were introduced into the random copolymer, giving a series of copolymers (poly(n-butylacrylate)-*co*-poly(2-methacryloyloxyethyl acrylate))-*b*-poly(glycidyl methacrylate)((PnBA-*co*-PMEA)-*b*-PGMA). Dynamic mechanical analysis indicated that the random copolymer block after ultraviolet (UV) irradiation was a lightly crosslinked polymer and acted as an elastomer, forming a photo-crosslinked network structure at the interface of carbon fiber/epoxy composites. Microbond test showed that such an interfacial network structure greatly improved the cohesive strength and effectively controlled the deformation ability of the flexible interlayer. Furthermore, three kinds of interfacial network structures, i) physical crosslinking by H-bonds, ii) chemical crosslinking by photopolymerization, and iii) interpenetrating crosslinked network by photopolymerization and epoxy curing reaction were received in carbon fiber/epoxy composite, depending on the various preparation processes.

***Keywords:*** *polymer composites, random copolymers, interfacial network structure, photo-crosslinking*

## 1. Introduction

Toughening of carbon fiber/epoxy composites has attracted a long-standing attention [1–4]. One of the most effective methods is by coating the carbon fibers with a ductile polymeric material to modify the mode of failure and thus the potential energy absorbing capacity of their composites [5–7]. However, many researches showed that thin coatings were finite in toughening the composites whereas thick coatings resulted in the reduction of composite strength and modulus [8, 9]. In our previous study [10–13], similar results showing that the prolongation of the flexible blocks increased the thickness of the flexible layer and as a result the interfacial shear strength decreased due to the low cohesive strength and modulus of the flexible chains, were also obtained. Therefore, achievement of a ductile interlayer that has both high cohesive strength and large deformation capacity is one of the most effective methods to toughen the CF/epoxy composites without any significant loss in strength of the composite. There are various approaches to improve the strength and modulus of polymers. For instance, as we known, the strength of polymer is mainly reflected in the chemical bond of the main chain and the intermolecular force, and thus to increase the polarity of the polymer or generate hydrogen bond may improve the strength of the polymer. Secondly, the introduc-

*Corresponding author, e-mail: xdzhou@ecust.edu.cn

tion of the rigid polymer chain groups (such as phenyl, etc.) or increasing the degree of branching of the molecular chain will increase the strength of a polymer to some extent. In addition, the polymer chains with a suitable crosslinking can effectively increase the intermolecular forces, consequently avoiding the relative slippage of the molecular chains. As the degree of crosslinking increases, the deformation of the molecular chain will be reduced. Therefore, in this way, cohesive strength and deformation ability of polymers can be effectively controlled. Among the physical and chemical crosslinking methods [14, 15], photo-crosslinking exhibits considerable advantages, including mild reaction conditions, minimum byproduct formation, absence of potential toxic catalysts and initiators and easily controlled processing [16]. Consequently, in recent years there has been an increasing interest in utilizing photo-crosslinking as a means of biomaterial preparation in the field of medicinal and biomedical science [17–21]. However, to our knowledge, introduction of photosensitive materials into the interface between carbon fibers and resin matrix has never been reported.

In our previous study [13], we designed a series of diblock copolymers poly(n-butylacrylate)-*b*-poly (glycidyl methacrylate) (PnBA-*b*-PGMA) and introduced them into the interface between carbon fibers and epoxy resin. The assembly behavior of the grafted diblock copolymers at the interface was proved to be that the flexible PnBA block, having poor compatibility with the resin matrix, forms the interfacial flexible layer on the fiber surfaces, while the other block PGMA can react with the epoxy resin and stretch into the matrix. The introduction of the flexible layer could uniformly disperse the stress at interface, decrease the stress concentration, relax the residual stress and improve the toughness of the composites. However, when the PnBA block was too long, large deformation of the flexible layer would lead to easier interfacial slippage or damages due to the low cohesive strength and modulus of the PnBA block, resulting in the decreased interfacial shear strength.

Therefore, in this paper, we aim to improve the cohesive strength and modulus of the flexible chains and consequently control the deformation ability of the flexible interlayer through the formation of the interfacial network structure via photo-crosslinking. Following our previous consideration, we design and synthesize a diblock copolymer (poly(n-butylacrylate)-*co*-poly(2-hydroxyethyl acrylate))-*b*-poly(glycidyl methacrylate) ((PnBA-*co*-PHEA)-*b*-PGMA) by atom transfer radical polymerization (ATRP). On one hand, the hydroxyl groups of the PHEA moieties in the flexible blocks can react with the functional groups on carbon fiber surfaces. On the other hand, the photo-crosslinkable groups (such as methacrylic groups, cinnamic groups, etc.) can be introduced into the flexible blocks by reacting with the hydroxyl groups. Additionally, by adjusting the molar ratio of nBA/HEA, the introduced amount of hydroxyl groups and thus the photo-crosslinkable groups can be controlled. With the introduction of such photo-crosslinkable groups into the interface, an interfacial network structure can be received under the ultraviolet (UV) irradiation. Afterwards, microbond test was employed to estimate the formation of the interfacial network structure in carbon fiber (CF)/epoxy resin composite.

## 2. Experimental section

### 2.1. Materials

The resin used in this study was the two part E-51(618)/T-31 epoxy system, provided by Shanghai Resin Factory Co. Ltd. Carbon fibers (CFs) (T700-12K) were purchased from Toray Industries, Inc. N,N,N′,N′,N″-pentamethyldiethylenetriamine (PMDETA, Aldrich, 99%), α-Bromoisobutyryl bromide (Aldrich, 98%), 2-Hydroxyethyl acrylate (HEA, Aldrich, 96%), and methacryloyl chloride (TCI Co., Ltd, 80%) were used as received. n-Butyl acrylate (n-BA Shanghai Lingfeng Chemical Reagent Co., Ltd, AR grade) and glycidyl methacrylate (GMA Shanghai Yuanji Chemical Co., Ltd, AR grade) were purified by passing through a neutral aluminum oxide column, distilling under reduced pressure and then keeping in the presence of 4 Å molecular sieve prior to use. CuBr (Sinopharm Chemical Reagent Co., Ltd, AR grade) and CuCl (Sinopharm Chemical Reagent Co., Ltd, AR grade) were purified by washing with glacial acetic acid, followed by absolute ethanol and ethyl ether and then dried under vacuum. Toluene (Aldrich, 99.8%) and triethylamine (TEA, Aldrich, 99%) were dried over calcium hydride ($CaH_2$) and then distilled under reduced pressure. Cyclohexanone (Shanghai No.1 Chemical Plant, AR grade) was also distilled under reduced pressure before use.

## 2.2. Polymerization procedures

### 2.2.1. Synthesis of diblock copolymer (PnBA-*co*-PHEA)-*b*-PGMA

The diblock copolymer (PnBA-*co*-PHEA)-*b*-PGMA was synthesized in two steps by atom transfer radical polymerization (ATRP), which depicted in Figure 1.

In a typical procedure, the random copolymer PnBA-*co*-PHEA was first synthesized. The monomers of HEA and nBA dissolved in cyclohexanone were charged in a three-neck round-bottom flask (250 mL), followed by adding the catalyst CuBr and ligand PMDETA with a ratio of 1:1. After being degassed and back-filled with nitrogen three times, the solution became a stable complex under a continuous stirring. Then the initiator EBriB was injected in it via a syringe, simultaneously immersed in a thermostated water bath of 70°C to initiate the polymerization. When the polymerization was stopped, the polymer solution was diluted with THF, passed through a column of neutral alumina to remove Cu-catalyst. After concentrated and precipitated twice in ether, and once more in methanol/water (1:1), the random copolymer Br-terminated PnBA-*co*-PHEA was dried under vacuum and then used as macroinitiator to initiate the polymerization of diblock copolymers.

Second, the diblock copolymer (PnBA-*co*-PHEA)-*b*-PGMA was synthesized in a similar manner to the polymerization of PnBA-*co*-PHEA, except Br-terminated PnBA-*co*-PHEA was used as the macroinitiator, CuCl as the catalyst, GMA as the monomer and n-hexane as precipitator. After the polymerization was conducted in a 30°C water bath for 3 h, the diblock copolymer was purified in a similar way to that described for the random copolymer Br-terminated PnBA-*co*-PHEA.

### 2.2.2. Synthesis of copolymer PnBA-*co*-PMEA

To study the ability of the copolymer PnBA-*co*-PHEA to introduce photosensitive groups and subsequent photopolymerization upon UV irradiation, copolymers poly(n-butylacrylate)-*co*-poly(2-methacryloyloxyethyl acrylate) (PnBA-*co*-PMEA) were prepared as follows: first, the as-prepared copolymers Br-terminated PnBA-*co*-PHEA, dissolved in toluene, and excess anhydrous TEA were charged into a 500 mL, three-necked, round-bottom flask, which was cooled at 0°C in ice water. Then methacryloyl chloride, diluted with dry toluene, was added dropwise under a nitrogen environment. The reaction mixture was kept stirring at room temperature for 2 days, followed by filtering carefully to remove triethylamine hydrochloride salt. After being concentrated and precipitated twice in n-hexane, the end-product was finally dried under vacuum overnight at 40°C. The synthetic illustration of PnBA-*co*-PMEA was shown in Figure 1.

## 2.3. Treatment of carbon fibers

### 2.3.1. Pre-treatment of carbon fibers

The carbon fibers as received were first extracted with acetone and petroleum ether in a Soxhlet apparatus for 24 h respectively, and then dried under vacuum at 60°C, denoted as CF0. Then, the chemical oxidation of CF0 was performed by refluxing in nitric acid ($HNO_3$) for 5 h at 100°C. The end-product was finally washed with distilled water to neutral PH, and dried under vacuum overnight at 60°C, named CF-COOH.

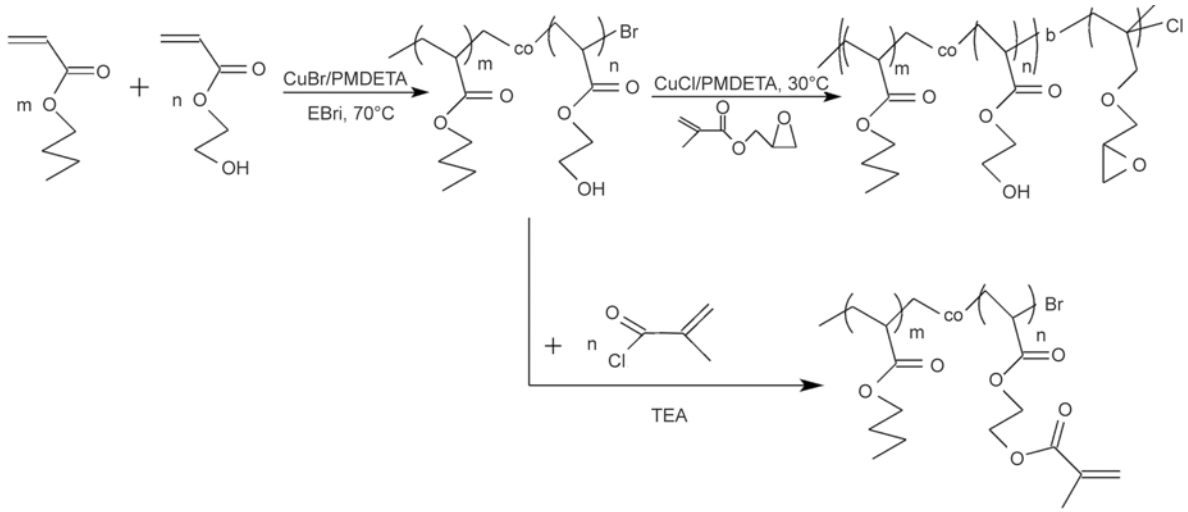


**Figure 1.** Synthetic routes of the copolymers (PnBA-*co*-PHEA)-*b*-PGMA and PnBA-*co*-PMEA

### 2.3.2. Grafting of diblock copolymers onto CFs

The as-prepared CF-COOH was immersed in thionyl chloride and stirring at 70°C for 24 h. The residual thionyl chloride was removed by reduced pressure distillation, giving acyl chloride-functionalized CF-COCl. Then, 2.4 g (PnBA-*co*-PHEA)-*b*-PGMA dissolved in 120 mL anhydrous dioxide was added immediately. The reactor was degassed under vacuum and back-filled with pure nitrogen for three times, and elevated temperature to 90°C. Finally, CFs grafted with diblock copolymer (PnBA-*co*-PHEA )-*b*-PGMA were taken out after 48 h, and extracted with acetone in a Soxhlet apparatus for 48 h to remove the physisorbed copolymers. After dried under vacuum overnight at 40°C, the grafted end-product was denoted as CF-PHEA. The typical grafting procedure was described as Figure 2.

### 2.3.3. Methacrylic functionalization of copolymers

A dried round bottom made-to-order reactor equipped with stirrer and pressure equalizing addition funnel was charged with 0.5 g CF-(PnBA-*co*-PHEA)-*b*-PGMA and 150 mL of dry toluene. After stirring for 15 min to mix uniformly under nitrogen atmosphere, 1.2 mL of triethyl amine were added in under continuous stirring. Subsequently, 0.5 mL methacryloyl chloride, diluted with 25 mL of dry toluene, were added dropwise to the reactor. After reacting at room temperature for 2 days under nitrogen atmosphere and continuous stirring, the CF-(PnBA-*co*-PMEA)-*b*-PGMA was obtained and named CF-PMEA. The schematic illustration of the preparation of CF-PMEA was shown in Figure 2. After that, the samples of CF-PMEA were extracted with THF in a Soxhlet apparatus for 24 h, and then dried under vacuum overnight at 40°C before use.

### 2.3.4. UV irradiation

The random copolymers PnBA-*co*-PMEA were first dissolved in THF and uniformly coated on glass slide. After solvent evaporation, the films of the random copolymers adhered to glass slide, were exposed to a 1000 W high-pressure mercury lamp (LT-101, Blue Sky UV and IR Techmology Development Co.) with a distance of around 10 cm for a certain time.

The carbon fibers grafted with diblock copolymers (PnBA-*co*-PMEA)-*b*-PGMA were divided into two groups to subject to UV irradiation. One was first incorporated with epoxy resin and cured, then subjected to UV irradiation, denoted as curing-crosslinking samples; the other was first subjected to UV irradiation and then incorporated with epoxy resin and cured, named as crosslinking-curing samples. The samples were subjected to UV irradiation in a similar manner with that of the random copolymers.

## 2.4. Preparation of the microbond testing samples

The detail of the preparation of CF/epoxy micro-composite for microbond test was same as that used in our previous study [22].

## 2.5. Instrument and measurements

Fourier transform infrared (FTIR) spectra of samples were recorded on a Thermo Electron Corporation

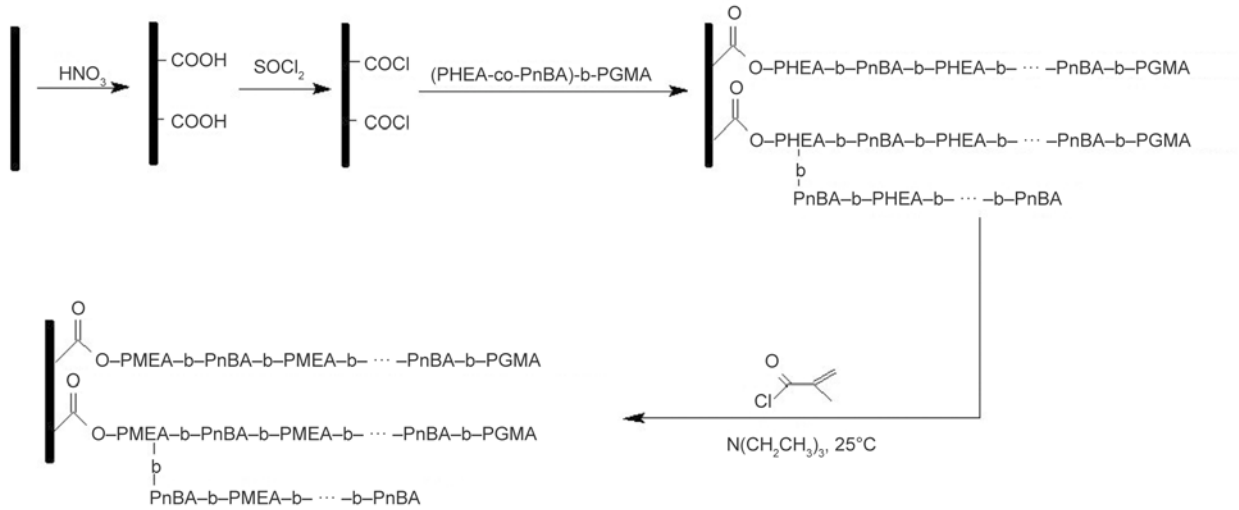


**Figure 2.** Schematic illustration of grafting block copolymer onto CF and subsequent methacrylic functionalization of the grafted copolymers

Nicolet 5700. The block copolymers were ground with potassium bromide (KBr) and pressed into pieces before FTIR test. CFs grafted with copolymers was recorded by attenuated total reflection of Fourier transform infrared spectroscopy (ATR-FTIR) using Ge crystal plate and Smart iTR accessory.

$^1$H-NMR spectra were recorded in deuterated acetone using a Bruker DSX 300 MHz spectrometer with the typical acquisition parameters.

A twice-detector gel permeation chromatography (GPC), equipped with an refractive index detector (Wyatt Technology Corp., Optilab REX) and a multi-angle static laser light scattering detector (Wyatt Technology Corp., DAWN HELEOS), was used to determine the absolute molecular weight and molecular weight distribution of diblock copolymers. The GPC was operated at a normal flow rate of 1 mL/min at 45°C, DMF with 0.05M LiBr used as eluent.

Scanning electron microscopy (SEM) was applicable to investigate the surface morphology of the carbon fibers. Samples were fixed to a platform with conductive tape, vacuum-dried and sputtered with gold. Images were taken on a HITACHI S-4800 scanning electron microscopy, operating at 15 kV.

A TA DMAQ800 dynamic mechanical thermal analyzer (USA) was employed to test the glass transition temperature of samples. The random copolymers were loaded into the lower tray of powder clamp used in conjunction with a dual cantilever clamp, and then placing the upper cover plate on top of the sample. After the filled clamp was installed, the test was performed from –60 to 80°C at 3°C/min with constant oscillation amplitude of 20 μm and frequency of 1 Hz.

The microbond test was performed on a YG004A Electronic single fiber tensile strength tester, provided by Changzhou No.2 Textile Machinery Co. Ltd. The interfacial shear strength (IFSS) was calculated as in the literature [23] and more than 30 specimens were successfully tested for each composite.

## 3. Results and discussion

### 3.1. Structure characterization of copolymers

Figure 3 shows the FTIR spectra of the obtained copolymers PnBA-*co*-PHEA and (PnBA-*co*-PHEA)-*b*-PGMA. The absorption peaks at 2960 and 2870 cm$^{-1}$ represent the alkane C–H stretching vibrations. The characteristic peak at 3430 cm$^{-1}$ is assigned to the characteristic absorption of –OH group. The strong characteristic peak at 1730 cm$^{-1}$ is attributed to the C=O stretching vibration. The absorption peaks at 1165 and 1070 cm$^{-1}$ correspond to the characteristic absorption of C–O group. These characteristic absorption peaks suggested that the monomer nBA and HEA were involved in the ATRP copolymerization. Furthermore, comparing with PnBA-*co*-PHEA, the FTIR spectrum of (PnBA-*co*-PHEA)-*b*-PGMA exhibited the characteristic peak of the epoxy ring at 909 and 841 cm$^{-1}$, indicating the successful synthesis of the block copolymer (PnBA-*co*-PHEA)-*b*-PGMA by ATRP.

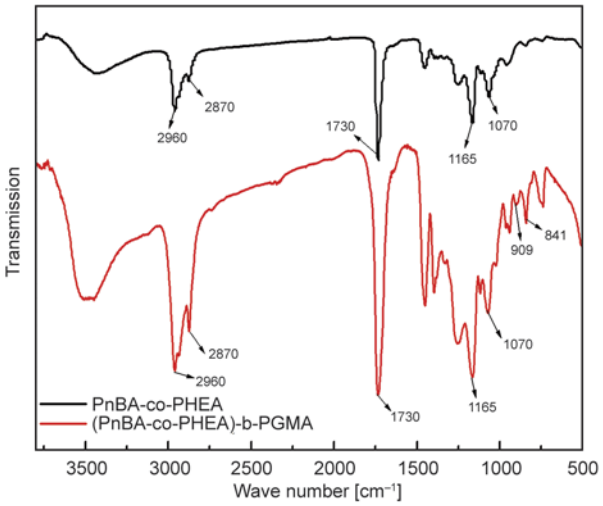


**Figure 3.** FTIR spectra of copolymers PnBA-*co*-PHEA and (PnBA-*co*-PHEA)-*b*-PGMA

The structure of the copolymer PnBA-*co*-PHEA was also characterized by $^1$H-NMR. Based on the composition of copolymers determined by $^1$H-NMR, the reactivity ratio of HEA/nBA monomer pair is estimated to be $r_{HEA}$ = 1.505 and $r_{nBA}$ = 0.894 by Kelen-Tüdős method, which has been reported in our previous paper [24], suggesting that the PnBA-*co*-PHEA was random copolymers. Therefore, there is a uniform random distribution of hydroxyl groups in PnBA-*co*-PHEA and thus the photosensitive groups in copolymer PnBA-*co*-PMEA after the esterification of hydroxyl groups with methacryloyl chloride, which may reduce the phenomenon that the local crosslinking density is too large during the formation of the interfacial crosslinking network.

The absolute molecular weights and molecular weight distributions of the synthesized copolymers were determined by GPC. The RI traces of GPC of PnBA-*co*-PHEA and (PnBA-*co*-PHEA)-*b*-PGMA

**Table 1.** Molecular weights, distributions and molar ratio of nBA/HEA of the synthesized random copolymers PnBA-*co*-PHEA

| Random copolymers | $\overline{M}_{n,GPC}$ [g/mol] | $\overline{M}_{w,GPC}$ [g/mol] | $\overline{M}_w/\overline{M}_n$ | Molar ratio of nBA/HEA |
|---|---|---|---|---|
| (PnBA-*co*-PHEA)$_{190}$ | 23 400 | 31 920 | 1.36 | 160:30 |
| (PnBA-*co*-PHEA)$_{220}$ | 28 470 | 33 940 | 1.19 | 160:60 |
| (PnBA-*co*-PHEA)$_{300}$ | 37 410 | 53 600 | 1.43 | 260:40 |
| (PnBA-*co*-PHEA)$_{310}$ | 40 910 | 53 760 | 1.31 | 210:100 |
| (PnBA-*co*-PHEA)$_{320}$ | 40 260 | 54 060 | 1.34 | 160:160 |

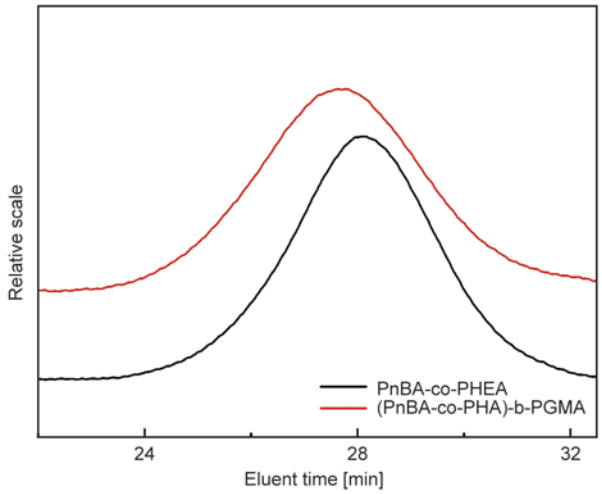


**Figure 4.** The RI traces of GPC of copolymers PnBA-*co*-PHEA and (PnBA-*co*-PHEA)-*b*-PGMA

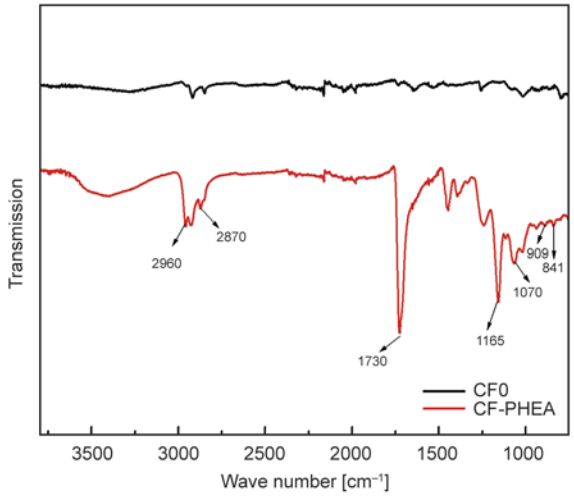


**Figure 5.** ATR-FTIR spectra of CF0 and CF-PHEA

were presented in Figure 4, and the calculated values for random copolymers PnBA-*co*-PHEA were listed in Table 1. It can be seen that both GPC traces of the random copolymer and block copolymer in Figure 4 are unimodal, and their molecular weight distributions is relatively narrow ($\overline{M}_w/\overline{M}_n$), as seen in Table 1. A series of random copolymers of various polymerization degrees and molar ratio of nBA/HEA were successfully synthesized. Besides, the eluent time for block copolymer is smaller than that of the random copolymer, and the peak of the block copolymer is shifted toward higher molecular weight position in Figure 4, indicating that the random copolymers can further initiate the polymerization of GMA monomers to prepare some kinds of block copolymers. Furthermore, the polymerization degree of GMA can be calculated from the absolute molecular weight and is about 100~110 for all the diblock copolymers.

### 3.2. Surface analysis of carbon fibers

The ATR-FTIR spectra of CF0 and CF-PHEA are shown in Figure 5. Compared to CF0, some new peaks of ester (–C=O, 1730 cm$^{-1}$), ether (–C–O–C, 1165 and 1070 cm$^{-1}$) and epoxy ring (909 and 841 cm$^{-1}$) that are all the characteristics of pure (PnBA-*co*-PHEA)-*b*-PGMA (Figure 3) appeared in ATR-FTIR spectra of CF-PHEA, indicating that (PnBA-*co*-PHEA)-*b*-PGMA chains have been successfully grafted onto CF surfaces.

It can be also seen from SEM micrographs of CFs (see Figure 6) that, the CF0 desized the commercial coatings has a relatively smooth surface (Figure 6a), whereas for the grafted CF, there are a few polymers deposited on the fiber substrate, resulting in a rough surface as shown in Figure 6b. Since the CFs were thoroughly washed by acetone to remove the physisorbed polymers after the grafting reaction, it would be reliable to conclude that the block copolymer (PnBA-*co*-PHEA)-*b*-PGMA was successfully chemically-grafted onto carbon fiber surface.

### 3.3. Photo-crosslinking of random copolymer PnBA-*co*-PMEA

To study the ability of the random copolymer PnBA-*co*-PHEA to introduce photosensitive groups and subsequent photopolymerization upon UV irradiation, the copolymer PnBA-*co*-PMEA was synthesized and initiated photopolymerization. Figure 7 shows the $^1$H-NMR and ATR-FTIR spectra of the random copolymer PnBA-*co*-PMEA.

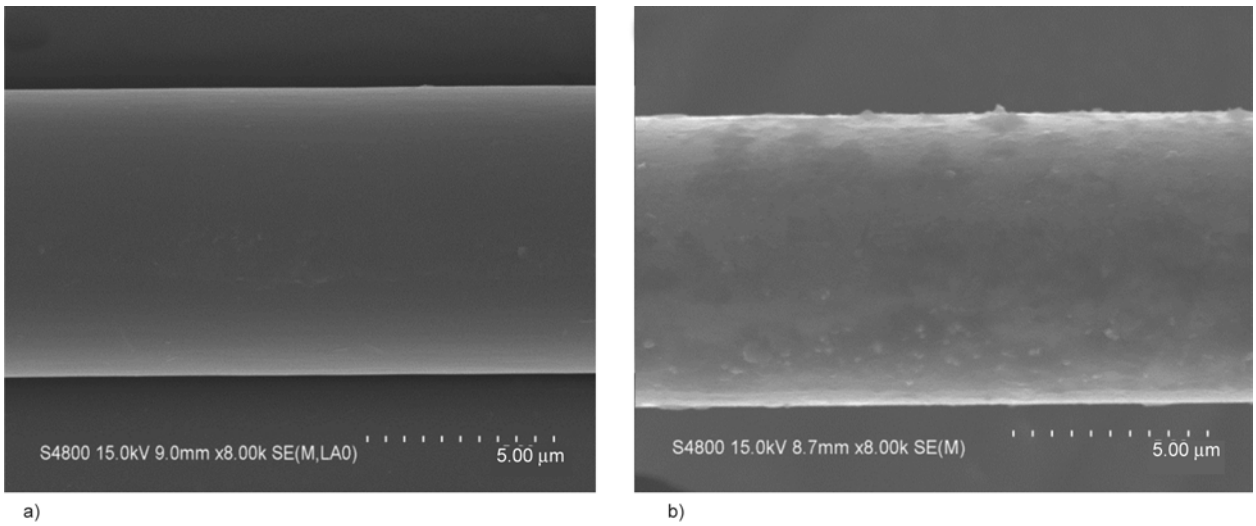


**Figure 6.** SEM micrographs of CF0 (a) and CF-PHEA (b)

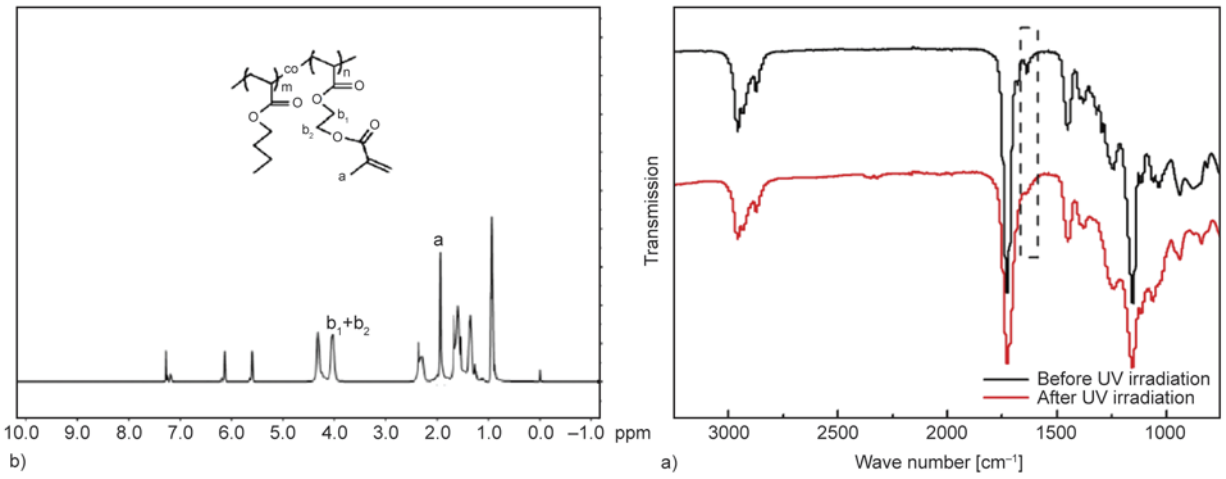


**Figure 7.** (a) $^1$H-NMR spectrum of random copolymer PnBA$_{160}$-*co*-PMEA$_{40}$; (b) ATR-FTIR spectra of copolymers PnBA-*co*-PMEA before and after UV irradiation

It can be found from Figure 7a that the peak of the methylene protons adjacent to the hydroxyl groups in random copolymer PnBA-*co*-PHEA at 3.8 ppm [24] completely disappeared. The peak (a) at 1.9 ppm is assigned to the methyl protons in methacrylic (MA) groups, while the peak ($b_1$ + $b_2$) at 4.0 ppm is due to the methylene protons adjacent to the MA groups. From the intensity of the two isolated and sharp peaks, we could accurately calculate their molar ratio to be 3/3.96, which is extremely close to that when the hydroxyl groups in PHEA moieties are totally substituted by the MA groups (3/4). Thus, it can be concluded that methacrylic functionalization of the random copolymer PnBA-*co*-PHEA, giving PnBA-*co*-PMEA, was completed under the reactive condition in this study.

The ATR-FTIR spectra of random copolymers PnBA-*co*-PMEA before and after UV irradiation are shown in Figure 7b. Compared with the FTIR spectrum of PnBA-*co*-PHEA (see Figure 3), the characteristic peak at 1636 cm$^{-1}$ attributed to stretching vibration of the double bonds in methacrylic groups was observed, indicating the successful esterification of methacryloyl chloride with hydroxyl groups of the random copolymer PnBA-*co*-PHEA. After UV irradiation, the infrared absorption intensity at 1636 cm$^{-1}$ of methacrylic double bonds in copolymer PnBA-*co*-PMEA decreased. This is attributed to the photopolymerizationof the methacrylic double bonds upon UV exposure, reported by many researchers [25–28] and schematically shown in Figure 8. Consequently, the content of methacrylic double bonds in PnBA-*co*-PMEA copolymers significantly reduced, corresponding to the decreased absorption intensity at 1636 cm$^{-1}$ as illustrated in Figure 7b.

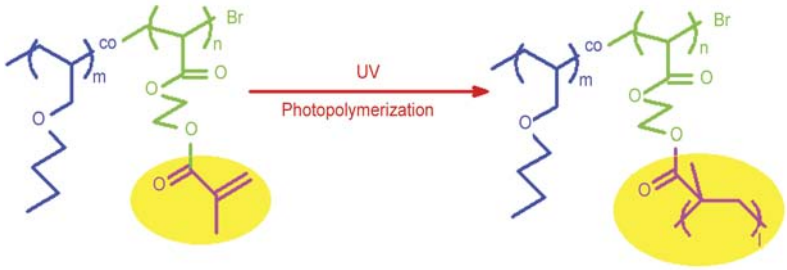


**Figure 8.** Schematic illustration of photopolymerization of copolymers PnBA-*co*-PMEA

The glass transition temperatures ($T_g$) of the copolymers PnBA160-*co*-PHEA$_{160}$ and PnBA160-*co*-PMEA$_{160}$ were evaluated by DMA and shown in Figure 9. It was found that all of the copolymers exhibited a single glass transition peak, conforming to the characteristic of the random copolymers. Compared to PnBA-*co*-PHEA, PnBA-*co*-PMEA that introduces MA groups, had no obvious increase in the glass transition temperature, only shifting from –27.7 to –26.2°C. This suggested that the photo-crosslinkable copolymer PnBA-*co*-PMEA retained the good flexibility of the random copolymer block. However, after UV irradiation, the transition loss peak decreased in intensity, broadened, and shifted to higher temperature of –16.5°C, which is the characteristic of crosslinking reaction and indicates the formation of the crosslinked network structure by the photopolymerization reaction [29]. It is noted that the glass transition temperature is still below zero temperatures, implying that the random copolymer block after UV irradiation is a lightly crosslinked polymer and acts as an elastomer.

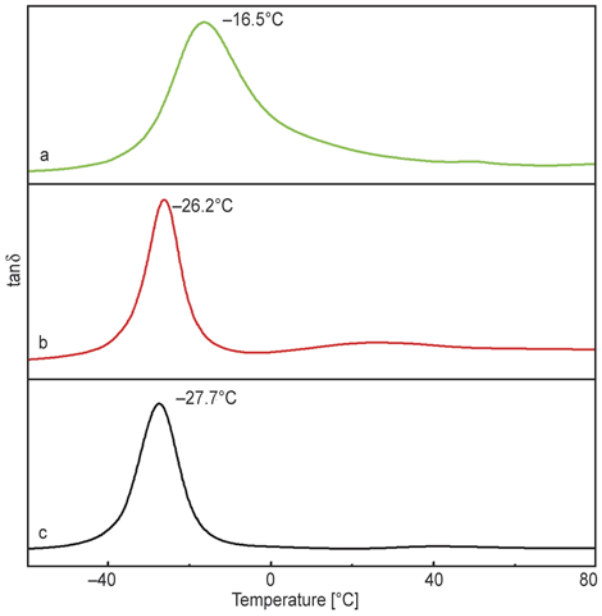


**Figure 9.** DMA curves of various copolymer samples (a) PnBA-*co*-PHEA; (b) PnBA-*co*-PMEA without UV irradiation; and (c) PnBA-*co*-PMEA after UV irradiation for 30 min

## 3.4. Formation of interfacial network structure

### 3.4.1. Physical crosslinking by H-bonds

Undoubtedly, the interfacial molecular structure can significantly determine the mechanical properties of interface region such as strength and modulus etc. and thus the bonding of fiber-interface region and interface region-matrix. Therefore, interfacial adhesion strength may be, in some cases, a response to interfacial molecular structure as matrix and fiber are fixed. In this paper, we first measured the interfacial shear strength of CF-PHEA/epoxy and CF-PMEA/epoxy micro-composites, respectively to investigate the variation of the interfacial molecular structure.

Figure 10 showed the IFSS results of epoxy resin micro-composites reinforced with different CFs. Due to the increased oxygen-containing functional groups on CF surface by oxidation, the IFSS value of CF-COOH composite increase d from 29.8±2.8

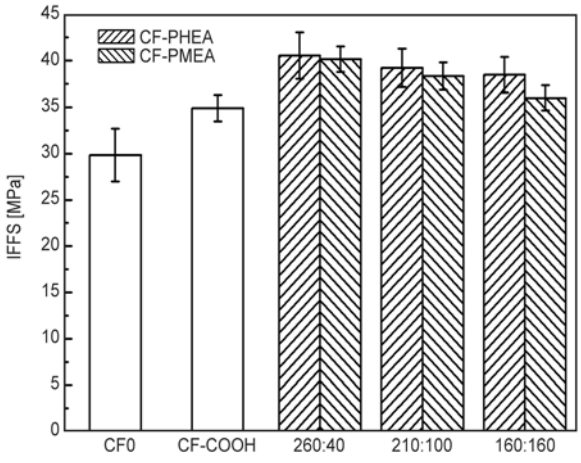


**Figure 10.** Influence of surface modification on the interfacial shear strength of CF/epoxy micro-composites (260:40, 210:100 and 160:160 are the molar ratio of nBA/HEA or nBA/MEA in the grafted copolymers with the same length of PGMA)

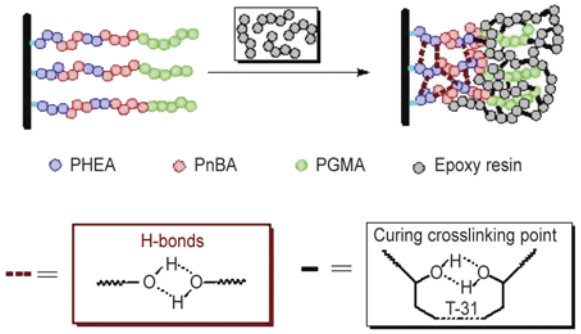


**Figure 11.** Illustration of the formation of the interfacial network structure crosslinking by H-bonds

to 34.9±1.4 MPa, in consistent with the results of our previous study [13]. Furthermore, with the introduction of diblock copolymers (PnBA-*co*-PHEA)-*b*-PGMA or (PnBA-*co*-PMEA)-*b*-PGMA into the interface, the interfacial adhesion of the composites was further improved, partly resulting from that the PGMA blocks in diblock copolymers can be involved in the curing reaction of the epoxy matrix. On the other hand, the existence of the interfacial flexible layer, forming by the other blocks PnBA-*co*-PHEA or PnBA-*co*-PMEA, can effectively transfer loads through its deformation and chain-movement, contributing to the increased IFSS values in CF-PHEA and CF-PMEA composites.

It was noted that all the IFSS values of CF-PHEA/epoxy composite are higher than those of the corresponding CF-PMEA/epoxy composite as illustrated in Figure 10. For CF-PHEA/epoxy composite, since the PHEA moieties in the grafted diblock copolymer contain many hydroxyl groups, it is easy to form the H-bonds between the PHEA moieties in the flexible layer (see Figure 11) [30]. It can be also reflected from the result in Figure 10 that the $T_g$ of PnBA-*co*-PMEA is only slightly higher than that of PnBA-*co*-PHEA. It is supposed to be that the substitution of MA groups (methacrylic double bonds) for hydroxyl groups can strongly increase the $T_g$ of PnBA-*co*-PMEA, but this effect is partly offset by the destroy of the H-bonds due to the disappearance of hydroxyl groups. However, in the CF-PMEA/epoxy composite, the interfacial structure without crosslinking possesses low cohesive strength and modulus, although PnBA-*co*-PMEA has higher $T_g$ than that of PnBA-*co*-PHEA. Thus, the formation of the interfacial network structure in CF-PHEA/epoxy composite, crosslinking by H-bonds, improved the strength and modulus of the flexible layer to a certain extent, and thereby the interfacial shear strength.

Furthermore, we can see that with an increase in the molar units of PHEA in the random copolymer PnBA-*co*-PHEA from 40 to 100 and 160, the IFSS value had a slight decrease. This indicates that the hydroxyl groups in PHEA moieties prefer to forming the H-bonds between each other, rather than being involved in the curing reaction of the epoxy resin in the presence of the PGMA blocks, because if the hydroxyl groups tend to involve in the curing reaction, the increase in the molar units of PHEA will be beneficial to the improvement in the interfacial adhesion. The slight decrease in IFSS resulted from that the total length of the flexible chain increased from 300 (PnBA/PHEA = 260:40) to 310 (PnBA/PHEA = 210:100) and 320 (PnBA/PHEA = 160:160). A more significant trend to decline was observed in the CF-PMEA/epoxy composite due to the destruction of the physical crosslinking by H-bonds. The increase in the total length of the flexible chain resulted in the larger deformation and interfacial slippage or damages, and thus the IFSS value of the CF-PMEA/epoxy composite decreased more significantly and from 40.15±1.4 to 38.3±1.5 MPa and 36.0±1.4 MPa.

### 3.4.2. Crosslinking by chemical bonds

In this section, the carbon fibers grafted with diblock copolymers ($PnBA_{160}$-*co*-$PMEA_{160}$)-*b*-PGMA were subjected to UV light for irradiation before and after being incorporated with the epoxy resin, respectively. The fibers that were first incorporated with epoxy resin and cured, then subjected to UV irradiation, are denoted as curing-crosslinking samples; while those with the treatment steps contrary to the above ones are named as crosslinking-curing samples. During the UV irradiation, the PMEA moieties in the grafted copolymers reacted with each other, as discussed in section 3.3, resulting in the crosslinking of flexible layer by chemical bonds. The IFSS values of the CF-PMEA/epoxy resin composites after UV irradiation for different time (15 and 20 min) through the two processes, respectively, are presented in Figure 12.

For the curing-crosslinking samples, the random copolymers PnBA-*co*-PMEA assembled into many hemispheres to form a perfect interfacial flexible layer on carbon fiber surface due to an entropic

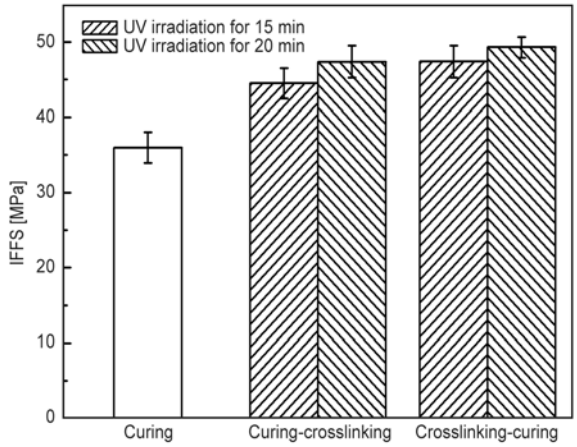


**Figure 12.** Effect of photo-crosslinking on IFSS of carbon fibers grafted with diblock copolymers ($PnBA_{160}$-*co*-$PMEA_{160}$)-*b*-PGMA/epoxy resin composite

repulsion during the curing process of the composite (see Figure 13) [10]. In this case, the unreacted low-molecular-weight epoxy resin and curing agent would be very hard to enter into the assembled flexible layer during the following process. Therefore, such an interfacial assembled structure that can release stress and uniformly transfer load, was perfectly retained after UV irradiation, resulting in the obviously increased interfacial shear strength, from 36.0±2.1 to 44.5±2.0 MPa for 15 min and 47.4±2.1 MPa for 20 min. However, since the molecular movement of the assembled hemispheres was difficult, the photo-crosslinking reactions between the PMEA moieties may tend to occur inside the isolated hemispheres. Thereby, the crosslinking between the hemispheres is less than the crosslinking inside the hemispheres, resulting in the crosslinked flexible interlayer with a regularly latticed distribution of crosslinking degree. Such an interfacial crosslinked structure can preferably retain the whole deformation ability of interface, but may lead to the local over-crosslinking inside the hemispheres as the crosslinking reaction proceeding.

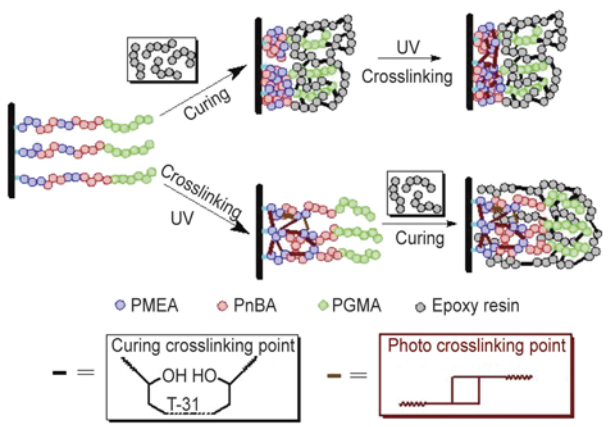


**Figure 13.** Illustration of the formation of the interfacial network structure crosslinking by chemical bonds

When the carbon fibers were first irradiated with UV light, the PMEA moieties in the grafted copolymers reacted with each other, forming the crosslinking networks in the flexible layer, which could be very difficult to reassemble in the following compounding process with epoxy resin. In this case, the grafted diblock copolymers, existing in a single chain, had strong motion ability before UV irradiation, beneficial to the crosslinking reaction and consequently the improvement of the crosslinking degree of the flexible blocks. Furthermore, due to the low molecular weight of the unreacted epoxy resin, some of the matrix polymer chains and the curing agent could diffuse into the photo-crosslinking network in the curing process. Therefore, the interfacial photo-crosslinked network and the epoxy cured network would form an interpenetrating crosslinked network structure in the interface region as illustrated in Figure 13. Such an interfacial network structure possesses high strength and modulus, which will benefit for the load transfer at the interface. Therefore, the interfacial adhesion between carbon fiber and epoxy resin was strongly enhanced, corresponding to the results (as seen in Figure 12) that the IFSS value sharply increased to 47.4±2.1 MPa after UV irradiation for 15 min, and 49.3±1.4 MPa for 20 min.

However, it should be noted that for the CF-PMEA/epoxy composite with the crosslinking-curing process, because of the formation of the interpenetrating crosslinked network and especially the small deformation ability of the epoxy crosslinked network, the whole deformation of the interfacial layer could be dramatically reduced, and thus the interfacial toughness of the composite may be decreased accompanying with the improvement of the interfacial adhesion.

## 4. Conclusions

In this study, a series of diblock copolymers (PnBA-*co*-PHEA)-*b*-PGMA containing one flexible random copolymer block PnBA-*co*-PHEA were successfully synthesized by ATRP. On one hand, the hydroxyl groups of the PHEA moieties in the flexible blocks can react with the functional groups on carbon fiber surfaces. On the other hand, the photo-

crosslinkable MA groups can be introduced into the flexible blocks by reacting with the hydroxyl groups. Due to the existence of the hydroxyl groups in the PHEA moieties, an interfacial network structure crosslinking by H-bonds was formed. While with the introduction of the photo-crosslinkable MA groups into the interface, an interfacial network structure crosslinking by chemical bonds was finally received by UV irradiation before (crosslinking-curing) and after (curing-crosslinking) CF incorporated with epoxy resin.

Microbond test showed that the formation of the interfacial network structure via photo-crosslinking greatly improved the cohesive strength of the flexible blocks, corresponding to the increased $T_g$, and thus effectively retained the whole deformation ability of the flexible interlayer. Furthermore, due to the formation of the interpenetrating crosslinked network structure between the photo-crosslinking network and the epoxy crosslinking network in the crosslinking-curing process, which possesses high strength and modulus and thus benefit for the load transfers of the interface, the interfacial properties of the CF/epoxy composites cured by the curing-crosslinking process and by crosslinking-curing process were slightly different. Consequently, the interfacial shear strength increased from 36.0±2.1 to 40.5±2.5 MPa for the interfacial network structure crosslinking by H-bonds, 47.4±2.1 MPa for 20 min UV irradiation in the curing-crosslinking process, and 49.3±1.4 MPa in the crosslinking-curing process.

## Acknowledgements

The authors sincerely acknowledge the support of NSFC 51073055 and the Fundamental Research Funds for the Central Universities.

## References

[1] Pearson R. A., Yee A. F.: Toughening mechanisms in elastomer-modified epoxies. Journal of Materials Science, **24**, 2571–2580 (1989).
DOI: 10.1007/BF01174528

[2] Kuwata M., Hogg P. J.: Interlaminar toughness of interleaved CFRP using non-woven veils: Part 1. Mode-I testing. Composites Part A: Applied Science and Manufacturing, **42**, 1551–1559 (2011).
DOI: 10.1016/j.compositesa.2011.07.016

[3] Wong D. W. Y., Lin L., MaGrail P. T., Peijs T., Hogg P. J.: Improved fracture toughness of carbon fibre/epoxy composite laminates using dissolvable thermoplastic fibres. Composites Part A: Applied Science and Manufacturing, **41**, 759–767 (2010).
DOI: 10.1016/j.compositesa.2010.02.008

[4] Gkikas G., Barkoula N-M., Paipetis A. S.: Effect of dispersion conditions on the thermo-mechanical and toughness properties of multi walled carbon nanotubes-reinforced epoxy. Composites Part B: Engineering, **43**, 2697–2705 (2012).
DOI: 10.1016/j.compositesb.2012.01.070

[5] Jiang Z. X., Liu L., Huang Y. D., Ren H.: Influence of coupling agent chain lengths on interfacial performances of carbon fiber and polyarylacetylene resin composites. Surface and Interface Analysis, **41**, 624–631 (2009).
DOI: 10.1002/sia.3074

[6] Tsubokawa N., Abe N., Wei G., Chen J., Saitoh S., Fujiki K.: Grafting of polymers onto a carbon-fiber surface by ligand-exchange reaction of poly(vinyl ferrocene-*co*-vinyl monomer) with polycondensed aromatic rings of the surface. Journal of Polymer Science Part A: Polymer Chemistry, **40**, 1868–1875 (2002).
DOI: 10.1002/pola.10268

[7] Severini F., Formaro L., Pegoraro M., Posca L.: Chemical modification of carbon fiber surfaces. Carbon, **40**, 735–741 (2002).
DOI: 10.1016/S0008-6223(01)00180-4

[8] Gerard J-F.: Characterization and role of an elastomeric interphase on carbon fibers reinforcing an epoxy matrix. Polymer Engineering and Science, **28**, 568–577 (1988).
DOI: 10.1002/pen.760280905

[9] Ishida I., Chaisuwan T.: Mechanical property improvement of carbon fiber reinforced polybenzoxazine by rubber interlayer. Polymer Composites, **24**, 597–607 (2003).
DOI: 10.1002/pc.10056

[10] Li Y., Lin Q., Chen L., Zhou X.: Assembly of triblock copolymer brush at glass fiber/polystyrene interface and its effect on interfacial shear strength. Composites Science and Technology, **69**, 1919–1924 (2009).
DOI: 10.1016/j.compscitech.2009.04.008

[11] Shen T., Zhou X., Lin Q.: Influence of grafting density of diblock copolymers on interfacial assembly behavior and interfacial shear strength of glass fiber/polystyrene composites. Composite Interfaces, **18**, 701–714 (2011).
DOI: 10.1163/156855412X626270

[12] Zhou X., Ying S.: Basalt fibres/polystyrene interfacial adhesion through modification of basalt fibres by block copolymers. Iranian Polymer Journal, **20**, 571–578 (2011).

[13] Deng S., Zhou X., Fan C., Lin Q., Zhou X.: Release of interfacial thermal stress and accompanying improvement of interfacial adhesion in carbon fiber reinforced epoxy resin composites: Induced by diblock copolymers. Composites Part A: Applied Science and Manufacturing, **43**, 990–996 (2012).
DOI: 10.1016/j.compositesa.2012.01.004

[14] Pilon L. N., Armes S. P., Findlay P., Rannard S. P.: Synthesis and characterisation of new shell cross-linked micelles with amine-functional coronas. European Polymer Journal, **42**, 1487–1498 (2006).
DOI: 10.1016/j.eurpolymj.2006.01.006

[15] Tillet G., Boutevin B., Ameduri B.: Chemical reactions of polymer crosslinking and post-crosslinking at room and medium temperature. Progress in Polymer Science, **36**, 191–217 (2011).
DOI: 10.1016/j.progpolymsci.2010.08.003

[16] Zheng Y., Andreopoulos F. M., Micic M., Huo Q., Pham S. M., Leblanc R. M.: A novel photoscissile poly (ethylene glycol)-based hydrogel. Advanced Functional Materials, **11**, 37–40 (2001).
DOI: 10.1002/1616-3028(200102)11:1<37::AID-ADFM37>3.0.CO;2-V

[17] Kadam V. S., Nicol E., Gaillard C.: Synthesis of flower-like poly(ethylene oxide) based macromolecular architectures by photo-cross-linking of block copolymers self-assemblies. Macromolecules, **45**, 410–419 (2012).
DOI: 10.1021/ma2022937

[18] Kim J. S., Youk J. H.: Preparation of core cross-linked micelles using a photo-cross-linking agent. Polymer, **50**, 2204–2208 (2009).
DOI: 10.1016/j.polymer.2009.03.013

[19] Sonoda Y.: Solid-state [2+2] photodimerization and photopolymerization of α,ω-diarylpolyene monomers: Effective utilization of noncovalent intermolecular interactions in crystals. Molecules, **16**, 119–148 (2011).
DOI: 10.3390/molecules16010119

[20] Stauch O., Uhlmann T., Fröhlich M., Thomann R., El-Badry M., Kim Y-K., Schubert R.: Mimicking a cytoskeleton by coupling poly(*N*-isopropylacrylamide) to the inner leaflet of liposomal membranes: Effects of photopolymerization on vesicle shape and polymer architecture. Biomacromolecules, **3**, 324–332 (2002).
DOI: 10.1021/bm015613y

[21] Piogé S., Nesterenko A., Brotons G., Pascual S., Fontaine L., Gaillard C., Nicol E.: Core cross-linking of dynamic diblock copolymer micelles: Quantitative study of photopolymerization efficiency and micelle structure. Macromolecules, **44**, 594–603 (2011).
DOI: 10.1021/ma102284y

[22] Hou J., Zhou X., Zhou X.: Grafting of poly(n-butylacrylate)-*b*-poly(2-hydroxyethyl methacrylate) on carbon fiber and its effect on composite properties. Polymer-Plastics Technology and Engineering, **50**, 260–265 (2011).
DOI: 10.1080/03602559.2010.531863

[23] He J. M., Huang Y. D.: Effect of silane-coupling agents on interfacial properties of CF/PI composites. Journal of Applied Polymer Science, **106**, 2231–2237 (2007).
DOI: 10.1002/app.26875

[24] Deng S., Ye H., Jiang D., Fan C., Lin Q., Zhao J., Zhou X.: Copolymerization and reactivity ratio measurement of n-butylacrylate and hydroxyethyl acrylate (in Chinese). Engineering Plastics Application, **41**, 92–95 (2013).
DOI: 10.3969/J.ISSN.1001-3539.2013.09.020

[25] Jin L., Agag T., Yagci Y., Ishida H.: Methacryloyl-functional benzoxazine: Photopolymerization and thermally activated polymerization. Macromolecules, **44**, 767–772 (2011).
DOI: 10.1021/ma102351a

[26] Pedrón S., Bosch P., Peinado C.: Using hyperbranched macromers as crosslinkers of methacrylic networks prepared by photopolymerization. Journal of Photochemistry and Photobiology A: Chemistry, **200**, 126–140 (2008).
DOI: 10.1016/j.jphotochem.2008.07.002

[27] Maruyama K., Kudo H., Ikehara T., Ito N., Nishikubo T.: Synthesis of photocrosslinkable hyperbranched polyesters and their film properties. Journal of Polymer Science Part A: Polymer Chemistry, **43**, 4642–4653 (2005).
DOI: 10.1002/pola.20957

[28] Maruyama K., Kudo H., Ikehara T., Nishikubo T.: Synthesis and properties of photo-cross-linkable hyperbranched poly(urethane)s containing both terminal methacryloyl groups and carboxyl groups. Macromolecules, **40**, 4895–4900 (2007).
DOI: 10.1021/ma062381s

[29] Chartoff R. P., Menczel J. D., Dillman S. H.: Dynamic mechanical analysis (DMA). in 'Thermal analysis of polymers: Fundamentals and applications' (eds.: Menczel J. D., Prime R. B.). Wiley, New York, 438–439 (2009).

[30] Lewin J. L., Maerzke K. A., Schultz N. E., Ross R. B., Siepmann J. I.: Prediction of hildebrand solubility parameters of acrylate and methacrylate monomers and their mixtures by molecular simulation. Journal of Applied Polymer Science, **116**, 1–9 (2010).
DOI: 10.1002/app.31232

*eXPRESS Polymer Letters Vol.8, No.7 (2014) 517–527*
*Available online at www.expresspolymlett.com*
*DOI: 10.3144/expresspolymlett.2014.55*

# Partially bio-based thermoplastic elastomers by physical blending of poly(hydroxyalkanoate)s and poly(ethylene-co-vinyl acetate)

*P. Ma[1,2,3*], X. Cai[4], M. Chen[1,2], W. Dong[1,2], P. J. Lemstra[3]*

[1]The Key Laboratory of Food Colloids and Biotechnology of Ministry of Education, 1800 Lihu Road, 214122 Wuxi, China.
[2]School of Chemical and Material Engineering, Jiangnan University, 1800 Lihu Road, 214122 Wuxi, China.
[3]Department of Chemical Engineering and Chemistry, Eindhoven University of Technology, 5612 Eindhoven AZ, the Netherlands.
[4]School of Food Science and Technology, Jiangnan University, 1800 Lihu Road, 214122 Wuxi, China

*Received 16 January 2014; accepted in revised form 19 March 2014*

**Abstract.** Partially bio-based thermoplastic elastomers (bio-TPE) were designed and prepared by physical blending a commercial grade poly(hydroxyalkanoate)s (PHBM, Metabolix) and poly(ethylene-co-vinyl acetate) (EVA). The PHBM is miscible with EVA90 which has a vinyl acetate (VA) content of 90 wt% while it is not miscible with EVA at low VA content (≤70 wt%). The PHBM/EVA90 blends exhibit high tensile strength and typical thermoplastic elastomeric characteristics e.g. high elongation at break (>800%), good strain-recovery (>60%) and melt processability. The spherulite growth rate of PHBM decreases with increasing EVA90 content. Consequently, a large number of fine PHBM spherulites were formed in the blends. The spherulites act as physical crosslink-points leading to a thermoreversable network in the blends. Such network and elastic EVA90 molecules result in the thermoplastic and elastomeric characteristics of the PHBM/EVA90 blends.

***Keywords:*** *polymer blends and alloys, poly(hydroxybutyrate), poly(ethylene-co-vinyl acetate), miscibility, thermoplastic elastomer*

## 1. Introduction

Polymers that derived from biomass have received considerable attention due to the sustainability issue and environment concern. Poly(hydroxyalkanoates) (PHAs) are synthesized and accumulated intracellularly by a number of micro-organisms [1, 2]. The best-known PHA is poly(3-hydroxybutyrate) (PHB) discovered in *Bacillus megaterium* by Lemoigne in 1926 [3]. PHB is a semi-crystalline thermoplastic with niche applications due to its biocompostability under both aerobic and anaerobic conditions, biocompatibility and renewable nature [4]. The mechanical and thermal properties of PHB are similar to those of poly(propylene). However, poly(propylene) cannot be substituted by PHB yet since there are many drawbacks which limit the applications of PHB, e.g. high production cost, poor processability and brittleness.

The brittleness of PHB is ascribed to large spherulites and cracks inside of the spherulites [5]. Consequently, PHB has low elongation at break ($\varepsilon_b$ ~3%) and low impact toughness ($\sigma_i$ ~2 kJ/m$^2$) [6]. Techniques such as synthesis of PHB copolymers by biological modification [7–9], blending [6, 10–14] and improvement on processing conditions [15, 16] have been developed to minimize the drawbacks.

*Corresponding author, e-mail: pimingma@hotmail.com

Synthesis of PHB copolymers could improve the toughness but compromise the strength and crystallization rate. On the other hand, blending is preferably used to toughen PHB.

The toughness of PHB could be improved by incorporation of rubbers. The $\sigma_i$ was increased by 440% after addition of epoxy natural rubber using maleated-poly(butadiene) as a compatibilizer [10]. The $\varepsilon_b$ of PHB was increased to 10% after addition of 20 wt% poly(hydroxyoctanoate) accompanied by a considerable reduction in tensile strength, crystallization temperatures ($T_c$) and melting temperatures ($T_m$) [11]. The $\varepsilon_b$ of PHB was even increased by a factor of 50 after addition of cellulose nanowhiskers using poly(ethylene glycol) as a plasticizer [12]. In another study, the ductility of poly(3-hydroxybutyrate-*co*-3-hydroxyvalerate) (PHBV, HV content = 12 mol%) was considerably enhanced by incorporation of 20 wt% bisphenol-A (BPA) ascribing to a formation of hydrogen bond network between the two components [13]. The yield stress and εb of the PHBV/BPA (80/20, wt/wt) blend were reported to be 16 MPa and 370% respectively. In our previous study, both $\varepsilon_b$ and $\sigma_i$ of PHB were increased by melt blending with biodegradable copolymers, i.e. poly(d,l-lactic acid) and poly(butylene succinate). The $\varepsilon_b$ and $\sigma_i$ were further improved via *in situ* compatibilization using peroxide as a free radical initiator [6, 14].

Blending is an effective and economic route to improve mechanical properties of polymers, however the toughness of PHB was only increased to a certain extent by blending with immiscible (co-)polymers. Some miscible (co-)polymers were blended with PHB in literatures such as poly(methyl methacrylate) [17], poly(ethylene oxide) [18] and poly (vinyl acetate) [19]. However, the effect of the miscible (co-)polymers on the mechanical properties of PHB was rarely studied. PHB-based thermoplastic elastomer (TPE) was even less reported.

The prime objective of this paper is to provide a method to prepare partially bio-based thermoplastic elastomers by physical blending PHBM and poly(ethylene-co-vinyl acetate) (EVA) copolymer. In the first part, the effect of vinyl acetate (VA) content on the miscibility, morphology and mechanical properties of the PHBM/EVA blends were investigated. In the second part, mechanical properties and morphology of the miscible PHBM/EVA blends were studied in detail and a mechanism for the thermoplastic elasticity was proposed based on the relation between properties and morphology. The thermoplastic elastomeric behavior of PHBM via melt blending with EVA, to the best of the authors' knowledge, has not been reported yet, which might broaden the application range of this polymer.

## 2. Experimental details

### 2.1. Materials

Commercial grade poly(hydroxyalkanoate)s (Mirel™ M6000) was supplied by Metabolix, Inc. USA, which is a mixture of poly(3-hydroxybutyrate) and poly (3-hydroxybutyrate-*co*-4-hydroxybutyrate). Since the two components are miscible, the mixture shows single phase morphology and thus is referred to as PHBM in this paper. EVA copolymers (Levapren® EVM) with VA contents from 40 to 90 wt% were supplied by Lanxess Chemical Co., Ltd.. The EVA with VA content of x wt% is coded as EVAx in this paper. The parameters of each grade EVA are shown in Table 1. Behenamide (analytical standard) as a nucleating agent was purchased from Fluka. All the materials were used as received.

**Table 1.** Characteristics of EVA copolymers

| Sample code | VA content [wt%] | Mooney viscosity[a] ML (1+4) 100°C [MU] | Density [kg/m$^3$] | $T_g$[b] [°C] |
|---|---|---|---|---|
| EVA40 | 40±1.5 | 20±4 | 980 | –32 |
| EVA50 | 50±1.5 | 27±4 | 1000 | –29 |
| EVA60 | 60±1.5 | 27±4 | 1040 | –28 |
| EVA70 | 70±1.5 | 27±4 | 1080 | –20 |
| EVA90 | 90±2.0 | 38±6 | 1150 | 14 |

[a]Tested according to IS289/ASTM D 1646.
[b]Measured by DSC at a heating rate of 10°C/min.

### 2.2. Blend preparation

The PHBM and EVA copolymers were dried at 50°C in a vacuum oven for 12 hours before use. PHBM/EVA blends with 0.5 wt% of behenamide based on the weight of PHBM were prepared in a twin-screw mini-extruder at 170°C for 3 min. The speed of screw was 90 rpm.

Two series of blends were studied:

– PHBM/EVA (80/20, wt/wt) blends with varying the VA content in EVA copolymers from 40 to 90 wt%;
– PHBM/EVA90 blends with compositions of 100/0, 90/10, 80/20, 70/30, 50/50, 30/70 and 0/100 (wt/wt).

The extrudates of PHBM/EVA blends were compression-molded into sheets (0.6 mm in thickness) at 175°C for 2 min and then cold compression-

molded for 15 min. The compression-molded samples were used for further characterizations. It has to be addressed that the degradation of PHBM/EVA blends under the above processing conditions were not so serious as evidenced by a relatively stable torque values of the mini-extruder as a function of processing time.

### 2.3. Characterizations

Scanning electron microscope (SEM): SEM (Quanta 600-F-ESEM, FEI, the Netherlands) was used to characterize the phase morphology of the PHBM/EVA blends. The samples were first cryo-microtomed at –80°C with a diamond knife and then sputter-coated with a thin gold layer at 65 mA for 45 seconds before observation.

Transmission electron microscope (TEM): TEM was performed on the PHBM/EVA90 (80/20, wt/wt) samples using a Tecnai 20 microscope, operated at 200 kV. Ultrathin sections (~100 nm) were prepared at –80°C using a Leica Ultracut S/FCS microtome. No staining was applied because PHBM and EVA copolymers have enough electron density contrast according to our previous study.

Two types of mechanical behavior were studied at room temperature:

– Universal tensile properties of the samples were measured by using a Zwick Z100 tensile tester at a crosshead speed of 10 mm/min. The narrow parallel-sided portion of the dumbbell-shaped tensile bar was 12 mm in length, 0.6 mm in thickness and 2 mm in width.
– Hysteresis cycle tests were performed on the same tensile tester. The dumbbell-shaped tensile bar was first stretched to 500% elongation with no hold time imposed at extension, after which the crosshead direction was immediately reversed to 170% elongation. The cross-head speed of stretching and recovering is 10 mm/min. Three repeating cycles were tested.

Dynamic mechanical analysis (DMA): DMA was carried out on a DMAQ800 (TA Instruments, USA) with a tensile-film mode. The specimens (13.0×6.5×0.6 $mm^3$) were measured from –60 to 170°C at a frequency of 1 Hz, with a constant amplitude of 10 μm and a temperature ramp of 3°C/min. The storage modulus and loss modulus were recorded as a function of temperature.

Differential scanning calorimetry (DSC): DSC analysis is performed on a DSC Q1000 (TA Instruments, USA). The samples were heated from –50 to 190°C. The first heating DSC scans were recorded and the glass transition temperatures ($T_g$) were obtained from the first heating DSC curves.

Polarized optical microscope (POM): Thin films of PHBM/EVA blends were cryo-microtomed from the compression-molded sheets. The spherulite morphology of each film was observed by using a Zeiss LM Axioplan microscope under polarization mode. The spherulite growth rate ($G$) of PHBM was measured by using the microscope in combination with a Linkam hot stage. Thin film of each sample was first heated to 190°C to erase thermal history, then quenched to designed temperatures, i.e. 70–130°C at a cooling rate of 60°C/min, and kept at the designed temperatures for isothermal crystallization. The radii of the spherulites ($r$, [μm]) were recorded as a function of time ($t$, [min]). The spherulite growth rate ($G$) was obtained via equation $G = \Delta r/\Delta t$.

## 3. Results and discussion

### 3.1. Effect of VA content on the miscibility and morphology of PHBM/EVA blends

A first insight in miscibility and phase separation of two (co-)polymers is comparing their solubility parameters ($\delta$). Two polymers may show miscible behavior if their solubility parameters are close to each other. An example is about poly(vinyl acetate) (PVAc) and PHBM whose solubility parameters are 9.6 and 9.1 $(cal/cm^3)^{1/2}$ respectively [20]. The solubility parameters of the EVA copolymers vary between the $\delta$ of LDPE (8.3 $(cal/cm^3)^{1/2}$ [20] and the $\delta$ of PVAc depending on composition. Thus, the miscibility between PHBM and EVA could be tuned by varying composition of the EVA copolymers.

The miscibility of polymers can be indicated by analysis of the glass transition temperatures ($T_g$) in their blends. The storage modulus ($E'$) and loss modulus ($E''$) of the PHBM/EVA blends from dynamic mechanical analysis (DMA) are presented in Figure 1. The peak temperatures of the $E''$ are referred to as $T_g$ of the corresponding components. The neat PHBM and the PHBM/EVA90 (80/20, wt/wt) blend show single $T_g$ of –1.3 and 8.3°C respectively. Each of the other samples displays two separate $T_g$, one for the PHBM phase ($T_{g\text{-PHBM}}$) and the other for the EVA phase ($T_{g\text{-EVA}}$), as noted in Figure 1. The glass transition temperatures of the PHBM/EVM90 blends were investigated as a function of EVA90 content, as shown in Figure 2. Only single $T_g$ is detected for

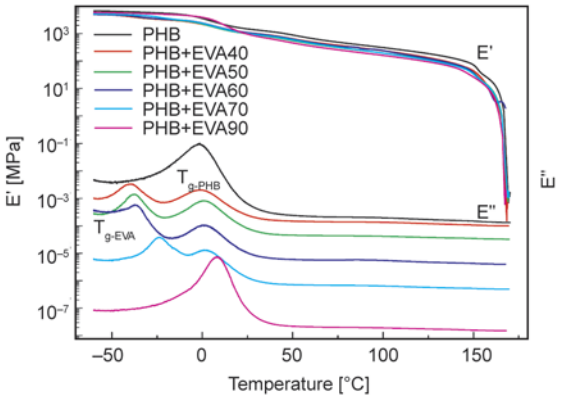


**Figure 1.** Storage modulus ($E'$) and loss modulus ($E''$) of the PHBM and the PHBM/EVA (80/20, wt/wt) blends. The $E''$ curves were shifted in the $y$ axis to avoid overlaps.

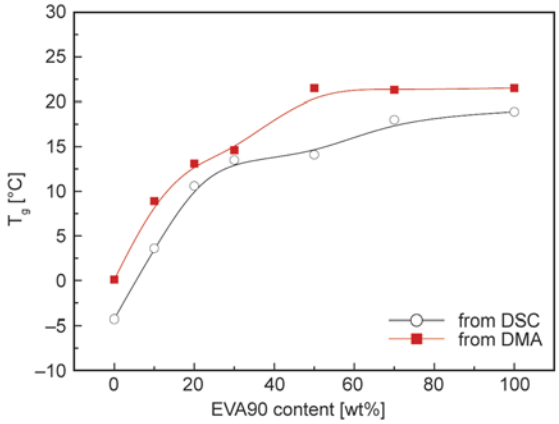


**Figure 2.** Glass transition temperatures ($T_g$) of the PHBM/EVA90 blends as a function of EVA90 contents. The $T_g$ is measured by using DSC and DMA respectively

each PHBM/EVA90 blend. Moreover, the $T_g$ shows strong dependence on compositions. These results indicate that PHBM is thermodynamically miscible with EVA90 but is immiscible with the other EVA copolymers. The values and variation trend of the storage modulus ($E'$) of the PHBM are slightly affected by addition of 20 wt% of the EVA copolymers since PHBM is a matrix.

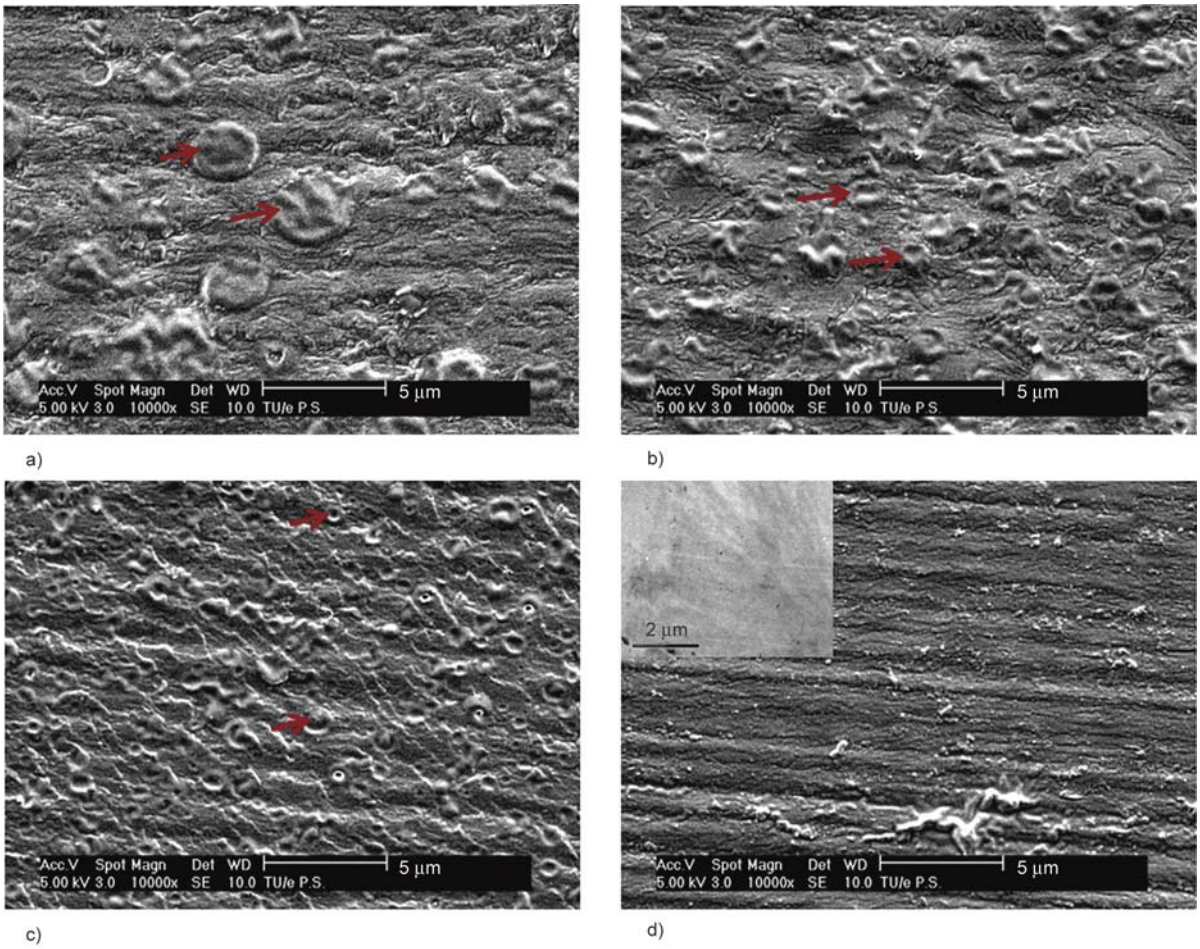


**Figure 3.** SEM images (scale bar = 5 µm) of the PHBM/EVA (80/20, wt/wt) blends as a function of VA contents: (a) 40 wt%, (b) 50 wt%, (c) 70 wt% and (d) 90 wt%. The EVA domains are indicated by arrays in PHBM matrix. The slight orientation of the morphology in these images is resulted from section-preparation (microtome). A TEM image of the PHBM/EVA90 (80/20, wt/wt) is shown as an inset in image d.

The morphology of PHBM/EVA (80/20) blends as a function of VA content is shown in Figure 3. Phase separation occurs between the PHBM and EVA when VA content is less than 70 wt%, indicating an immiscible feature. Since the vinyl acetate segments are miscible with the PHBM matrix, [19] the interfacial properties of the PHBM/EVA blends are improved with an increase in VA content. The particle size of the EVA40 in the blend is relatively large (~3 μm) being ascribed to a high interfacial tension. The EVA particle size is decreased to ~1 μm with increasing the VA content to 70 wt% (Figure 3a–3c). On the other hand, no phase separation is observed in the PLA/EVA90 blend (Figure 3d) as they are miscible. It has to be remarked that heterogeneities and oriented pattern on the PHBM/EVA90 surface (Figure 3d) are caused in sample preparation (microtome) process. The single-phase morphology of the PHBM/EVA90 blend is further confirmed by TEM characterization as shown by the inset in Figure 3d.

### 3.2. Effect of VA content on the mechanical properties of PHBM/EVA blends

Miscibility and morphology are crucial to mechanical properties of a polymer blend. Tensile properties of the PHBM/EVA (80/20, wt/wt) blends as a function of VA content are investigated and shown in Figure 4. All the blends show yielding behavior during tensile test. The maximum tensile strength ($\sigma_{m\text{-}t}$) of the blends increases gradually with the VA content. The highest $\sigma_{m\text{-}t}$ (30 MPa) and elongation at break ($\varepsilon_b$ = 150%) are obtained at the VA content of 90 wt%. The *E*-modulus of the blends varies between 600 and 800 MPa when the VA content increases from 40 to 90 wt%, as shown in Figure 4b. Neat PHBM is rigid with $\sigma_{m\text{-}t}$ and $\varepsilon_b$ of 36 MPa and 5.6% respectively (see Figure 5), thus the ductility of PHBM was improved by addition of 20 wt% EVA.

### 3.3. Mechanical properties of PHBM/EVA90 blends

EVA90 is the most promising among the studied EVA grades in improving mechanical properties of PHBM (Figure 4), therefore the mechanical behavior of the PHBM/EVA90 blends are investigated in detail, as shown in Figure 5.

The stress-strain curves of the PHBM/EVA90 blends are shown in Figure 5a. EVA90 shows typical stress-strain behavior of an elastomer. In contrast, PHBM is brittle with high tensile stress and low elongation at break. It fractures without yielding (Figure 5a curve 1). The PHBM/EVA90 (80/20, wt/wt) shows strong strain-softening followed by a weak strain-hardening. Consequently this blend breaks at relatively low elongation, as shown in Figure 5a curve 2. Strain-softening is an indication of strain localization. If the strain cannot be delocalized brittle fracture would occur. It is known that strain can be delocalized via strain-hardening resulting in tough materials [21]. The strain-softening behavior becomes less pronounced with increasing the EVA90 content up to 70 wt%, while the strain-hardening becomes more pronounced. As a consequence, the blends with high EVA90 content behave as thermoplastic elastomers (TPE) or thermoplastic vulcanizates (TPV) [22].

Figure 5b shows the yield stress ($\sigma_y$) and yield strain ($\varepsilon_y$) of the PHBM/EVA90 blends. The $\sigma_y$ decreases monotonically with increasing EVA90 content accompanied by an increase in $\varepsilon_y$ indicating an enhanced ductility. The $\sigma_{m\text{-}t}$ and $\varepsilon_b$ of the blends (Figure 5c) show similar trends as the $\sigma_y$ and $\varepsilon_y$ respectively. Remarkably, the $\varepsilon_b$ of the PHBM is

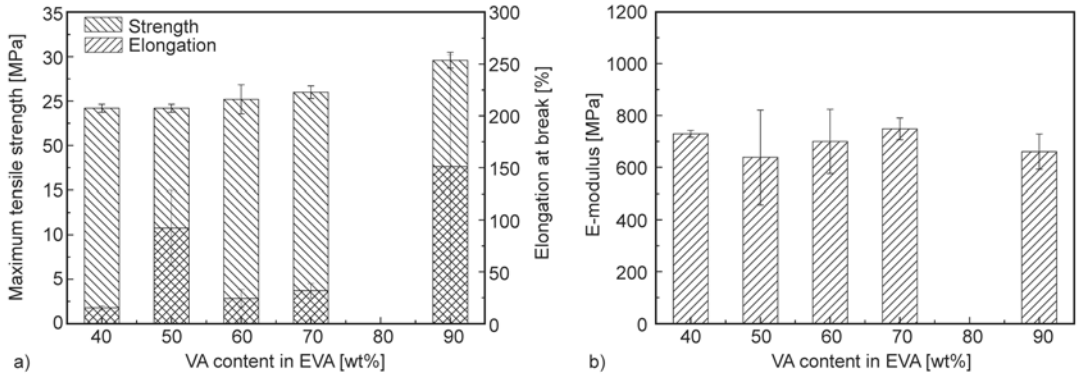


**Figure 4.** Tensile properties of the PHBM/EVA (80/20, wt/wt) blends as a function of VA contents. (a) maximum tensile strength and elongation at break and (b) *E*-modulus.

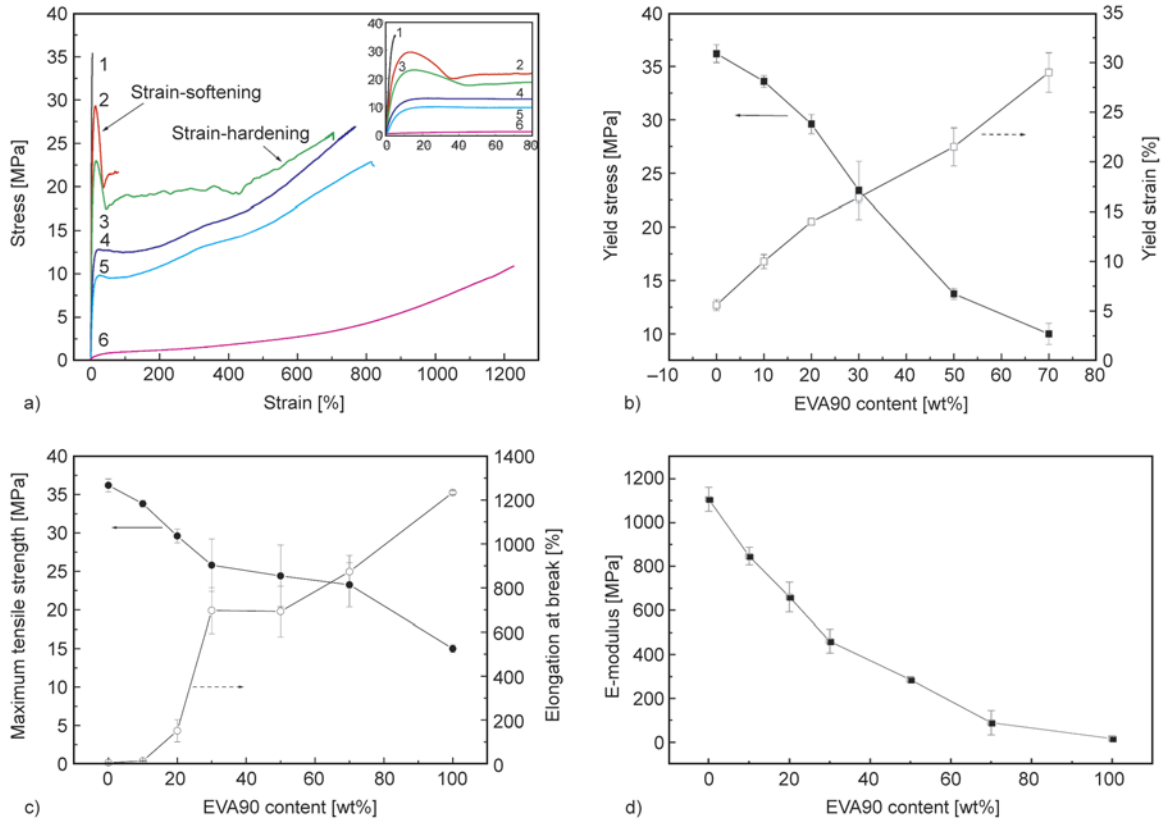


**Figure 5.** Mechanical behaviour of the PHBM/EVA90 blends as a function of EVA90 contents. (a) stress-strain curves, (b) yield stress and yield strain, (c) maximum tensile strength and elongation at break and (d) *E*-modulus. The stress-strain curves of 1–6 in Figure 5a correspond to the PHBM/EVA90 blends with the EVA90 content of 0, 20, 30, 50, 70 and 100 wt% respectively, and the initial stage of the stress-strain curves is inset in Figure 5a to clarify the yielding behavior of the samples.

increased by a factor of more than 140 after addition of 30–50 wt% of the EVA90. Meanwhile, the $\sigma_{m\text{-}t}$ is much higher than the $\sigma_y$, notably at high EVA90 content because of the pronounced strain-hardening. In addition, *E*-modulus of the blends decreases with increasing the EVA90 content, as shown in Figure 5d. These results display elastic behavior of the PHBM/EVA90 blends.

### 3.4. Strain-recovery behavior of PHBM/EVA90 blends

The PHBM/EVA90 blends show high and fast strain-recovery within a short time (>60% within 4 min), as demonstrated in Figure 6. The strain-recovery feature remains in the repeating cycles. These results indicate good elasticity and rubbery characters of the blends. Meantime, the PHBM/EVA90 blends exhibit notable stress-strain hysteresis which is a characteristic feature of thermoplastic elastomers [23] The lower content of the EVA90 the more remarkable hysteresis. It is also noticed that the hysteresis mainly occurs in the first hysteresis stress-strain cycle since the second and third cycles are close to each other (the 3rd cycle is not shown here to make the curves more readable). EVA90 shows very similar strain-recovery behavior as the blends (Figure 6d). Hence, the existence of EVA90 might be one of the key reasons for the elastic behavior of the PHBM/EVA90 blends.

### 3.5. Mechanism of the thermoplastic elasticity of PHBM/EVA90 blends

Heterogeneities are needed for toughness of polymers while crosslink is required for elasticity. As discussed above, the PHBM/EVA90 blends show typical thermoplastic elasticity. However, neither heterogeneities nor chemical crosslinks exist in the blends. It thus would be of interest to reveal the mechanism of the thermoplastic elasticity of the blends.

A typical route to make TPE is by blending a plastic with an immiscible rubber in combination with dynamic crosslinking. [24–26] In such process the rubber phase is crosslinked and re-dispersed in the

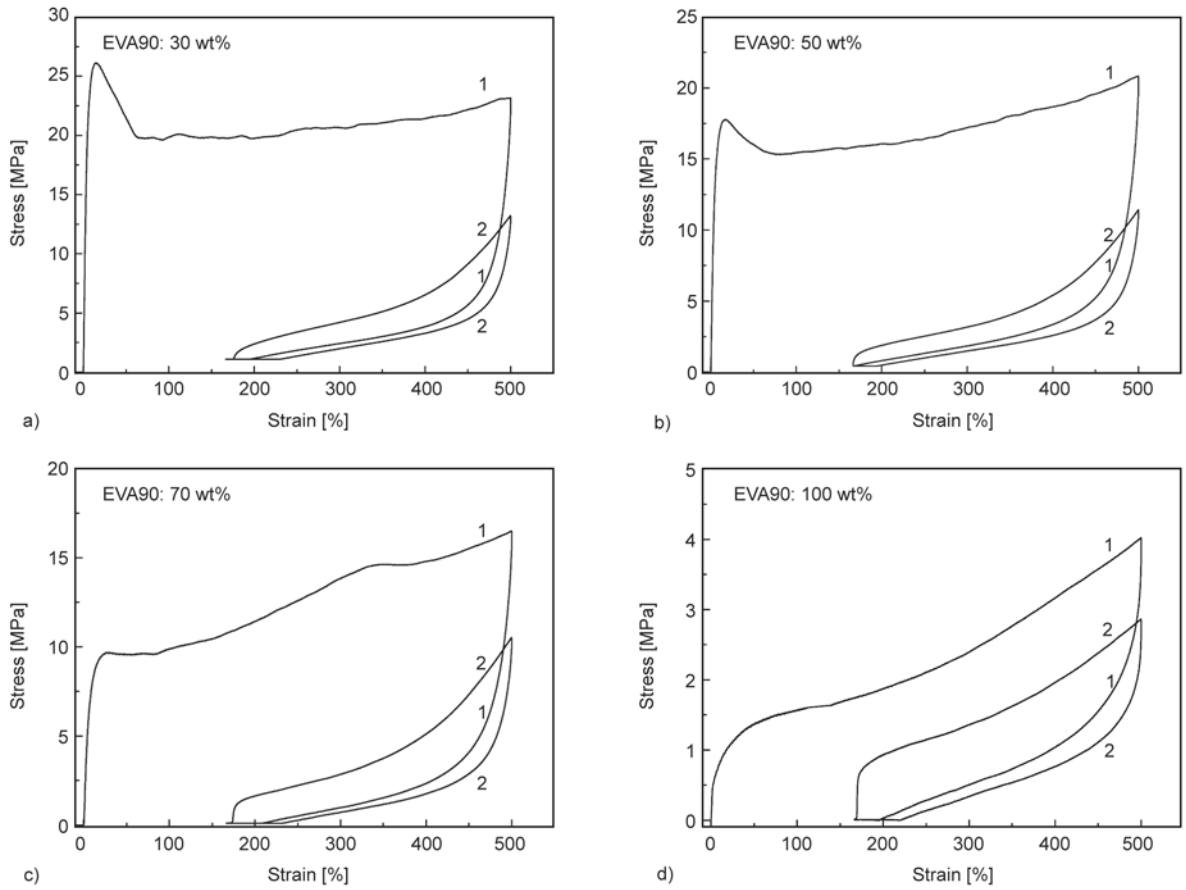


**Figure 6.** Hysteresis stress-strain curves of the PHBM/EVA90 blends as a function of EVA90 contents: (a) 30 wt%, (b) 50 wt%, (c) 70 wt% and (d) 100 wt%. The 1st and 2nd cycles are indicated by Arabic numerals in the figures.

plastic phase. The re-dispersed rubber phase interconnects leading to good elastic properties and the properties are affected by rubber particle size, e.g. TPE (or TPV) from poly(propylene)/ethylene-propylene-diene rubber blends [22]. The other route to prepare TPE is by making block copolymers containing both soft and hard segments, e.g. thermoplastic poly(urethane) (TPU) and styrene-b-butadiene-b-styrene copolymers (SBS) [27, 28].

PHBM is a brittle semi-crystalline thermoplastic. The brittleness of PHBM is ascribed to large spherulites and cracks in the spherulites [5]. Therefore, the crystallization behavior (e.g. morphology and crystallinity) is important to its mechanical properties. In this study, the crystallization of PHBM in the blends was complete since no cold crystallization peaks were detected from the first heating DSC curves, as shown in Figure 7. The crystallinity ($X_c$) of PHBM is around 38% in the samples (Figure 8) calculated via equation $X_c = \Delta H_m/(\Delta H_0 \cdot W)\cdot 100\%$, where $\Delta H_0$ is the melt enthalpy of 100% crystalline PHB (146.6 J/g) [29], $\Delta H_m$ is the measured melt enthalpy of PHBM in the blends, $W$ is the weight fraction of the PHBM in the blends. Although the $X_c$ of PHBM was similar in different samples, the crystallization kinetics, crystal morphology and the $X_c$ of the blends (obtained via equation $X_c = \Delta H_m/\Delta H_0 \cdot 100\%$) show strong dependence on the compositions.

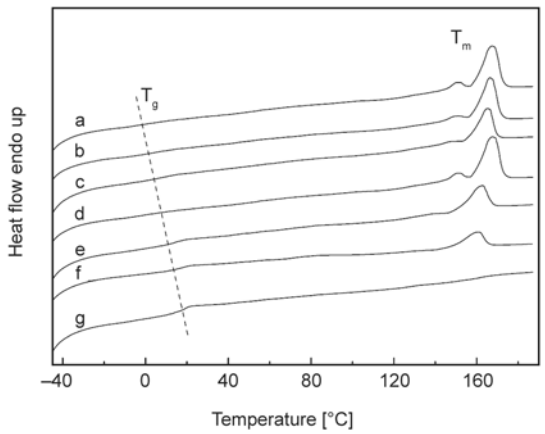


**Figure 7.** The first heating DSC curves of the PHBM/EVA90 blends as a function of EVA90 contents: (a) 0 wt%, (b) 10 wt%, (c) 20 wt%, (d) 30 wt%, (e) 50 wt%, (f) 70 wt% and (g) 100 wt%

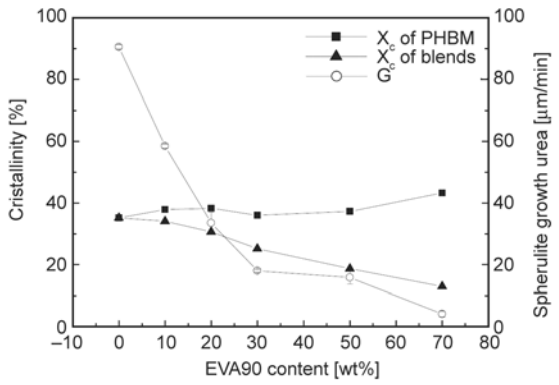


**Figure 8.** Crystallinity ($X_c$) of the PHBM and the PHBM/EVA90 blends and spherulite growth rate ($G$) of the PHBM as a function of EVA90 contents. The $G$ presented in Figure 8 was measured at 90°C while it shows similar trend at other temperatures (not shown here).

It was reported that crystallization kinetics of PHB were slowed down by addition of miscible PVAc. [19]. Similar behavior was observed in the PHBM/EVA90 blends e.g., the spherulite growth rate ($G$) of the PHBM decreases with increasing the EVA90 content, as shown in Figure 8. As a result, the spherulite morphology of the PHBM/EVA90 blends was improved by addition of the EVA90, which was studied by using polarized optical microscope (POM), as shown in Figure 9.

Large spherulites (~150 μm) with cracks are observed in neat PHBM (Figure 9a) resulting in brittleness of the PHBM. The spherulite size was reduced to 50–100 μm after addition of 10–20 wt% of the EVA90, leading to a notable improvement in the toughness. Due to the decrease in $G$ and the presence of nucleating agents, a large number of spherulites with sub-μm dimensions are uniformly dispersed in the PHBM/EVA90 blends when the EVA90 content is higher than 30 wt% (Figures 9d, 9e and 9f). Such morphology is associated with the above discussed thermoplastic elastomeric properties. The EVA90 molecules are diluted in the PHBM matrix when the EVA90 content is lower than 20 wt%, whereas the EVA90 molecules may interentangle at high content (>30 wt%) in the blends. Since the EVA90 is amorphous and rubbery (Figure 9g and Figure 5a), it exists as random coil in the amorphous region of the blends, i.e. between PHBM lamellae and between spherulites. The lamellae and fine spherulites play a role of physical crosslink points of the amorphous PHBM and the rubbery EVA90 molecules resulting in a thermoreversible network. The network is schematically illustrated in Figure 10a. The stress under deformation can be delocalized by stretching the random coils and the physical network (Figure 10b), thus toughness and ductility of the blends are obtained. The deformation can be recovered to a high degree when the stress is removed because random coil is the favorable state of the rubbery molecules, as illustrated in Figure 10a–10b. Consequently, this special structure results in high elasticity of the PHBM/EVA90 blends. Another advantage is that the blends are easily processable after melting and show elastic behavior after crystallization, as illustrated in Figure 10a–10c.

## 4. Conclusions

The properties of poly(hydroxyalkanoate)s (PHBM, Metabolix) were modified by poly(ethylene-co-vinyl acetate) (EVA) using a melt-blending technique. The miscibility between the PHBM and EVA were studied via thermal analysis (DMA and DSC) and microscopy (SEM and TEM). The PHBM is immiscible with EVA at VA content lower than 70 wt%, while is miscible with EVA90 which contains 90 wt% of VA. The effect of VA content on the mechanical properties of the PHBM/EVA (80/20, wt/wt) blends was studied. The PHBM/EVA90 (80/20, wt/wt) blend shows higher maximum tensile strength ($\sigma_{m\text{-}t}$) and larger elongation at break ($\varepsilon_b$) than the others. PHBM is brittle and stiff with high $\sigma_{m\text{-}t}$ and low $\varepsilon_b$. It is toughened by 20 wt% of the EVA90 showing notable stress yielding and high elongation at break. Interestingly, thermoplastic elastomeric behavior of the PHBM/EVA90 blends was achieved when the EVA90 content is higher than 30 wt%, i.e., high $\varepsilon_b$ (>800%), good strain-recovery and moderate $E$-modulus (<500 MPa). The thermoplastic elastomeric properties of the PHBM/EVA90 blends are associated with their structures. Crystallization of the PHBM occurred in the PHBM/EVA90 blends upon cooling. Since the EVA90 is thermodynamically miscible with the PHBM it exists among the PHBM crystals (lamellae and spherulites). Moreover the spherulite growth rate of PHBM is reduced in the presence of EVA90 which results in small spherulite size but large in numbers. Consequently the PHBM crystals, e.g. the large number of fine spherulites act as crosslink points leading to a physical network in the blends. The physical network and elastic EVA90 molecules are considered to be responsible for the thermoplastic elastomeric prop-

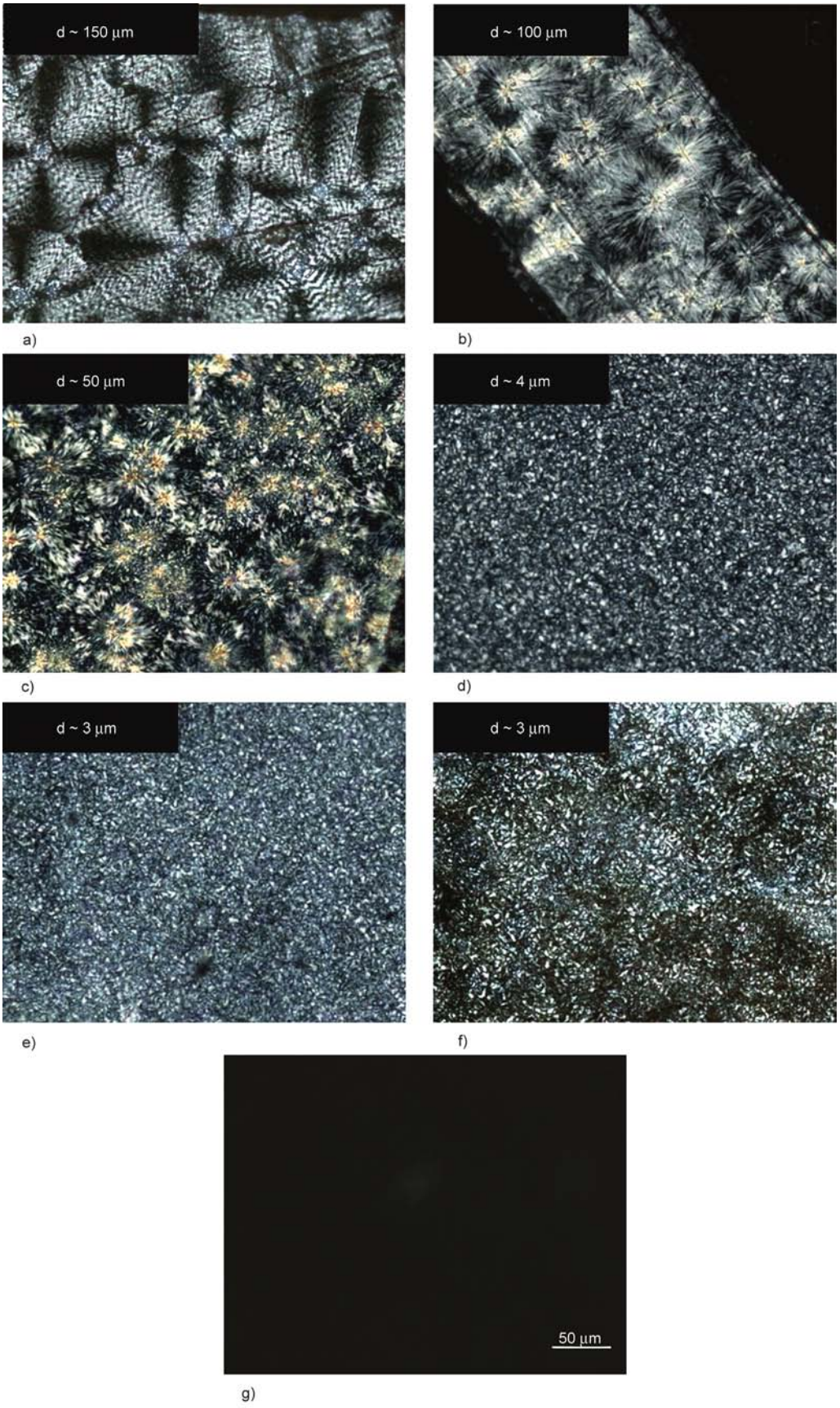


**Figure 9.** Polarized optical microscope images (scale bar = 50 µm, same magnification) of the PHBM/EVA90 blends as a function of EVA90 contents: (a) 0 wt%, (b) 10 wt%, (c) 20 wt%, (d) 30 wt%, (e) 50 wt%, (f) 70 wt% and (g) 100 wt%. The images were taken from compression molded samples. The average spherulite size is shown on the top left of each image.

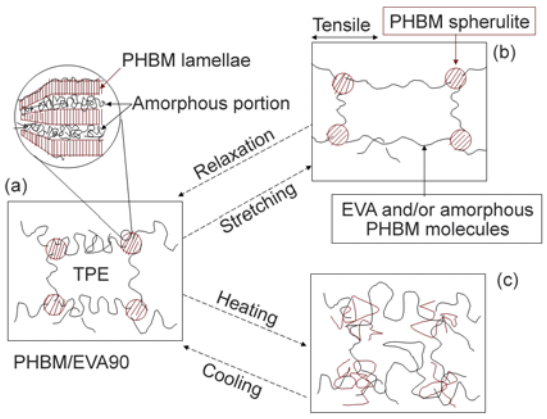


**Figure 10.** Schematic illustration of micro-structures of the PHBM/EVA90 blends in different states: (a) solid static state, (b) stretched state and (c) melt state. (a)–(b) shows the elastic behavior while (a)–(c) shows the thermoplastic behavior.

erties. Therefore, a new class of partially bio-based thermoplastic elastomers (bio-TPE) is designed and prepared which has potential application in substitution of conventional TPE materials.

## Acknowledgements

This work is supported by the National Natural Science Foundation of China (51303067, 51173072) and the Natural Science Foundation of Jiangsu Province (BK20130147). The authors acknowledge P. Schmit and A.B. Spoelstra from Eindhoven University of Technology in the Netherlands for valuable discussions on the morphology characterization and acknowledge Lanxess Chemical Co., Ltd. for kindly providing EVA (Levapren® EVM) materials.

## References

[1] Saito Y., Doi Y.: Microbial synthesis and properties of poly(3-hydroxybutyrate-*co*-4-hydroxybutyrate) in *Comamonas acidovorans*. International Journal of Biological Macromolecules, **16**, 99–104 (1994). DOI: 10.1016/0141-8130(94)90022-1

[2] Rodríguez-Contreras A., Koller M., Dias M. M. D.: Calafell-Monfort M., Braunegg G., Marqués-Calvo M. S.: High production of poly(3-hydroxybutyrate) from a wild *Bacillus megaterium* Bolivian strain. Journal of Applied Microbiology, **114**, 1378–1387 (2013). DOI: 10.1111/jam.12151

[3] Lemoigne M.: Assay of poly-β-hydroxybutyric acid. Bulletin de la Societe de Chimie Biologique, **8**, 770–782 (1926).

[4] Sudesh K., Abe H., Doi Y.: Synthesis, structure and properties of polyhydroxyalkanoates: Biological polyesters. Progress in Polymer Science, **25**, 1503–1555 (2000). DOI: 10.1016/S0079-6700(00)00035-6

[5] Hobbs J. K., McMaster T. J., Miles M. J., Barham P. J.: Cracking in spherulites of poly(hydroxybutyrate). Polymer, **37**, 3241–3246 (1996). DOI: 10.1016/0032-3861(96)88468-0

[6] Ma P., Hristova-Bogaerds D. G., Lemstra P. J., Zhang Y., Wang S.: Toughening of PHBV/PBS and PHB/PBS blends via *in situ* compatibilization using dicumyl peroxide as a free-radical grafting initiator. Macromolecular Materials and Engineering, **297**, 402–410 (2012). DOI: 10.1002/mame.201100224

[7] Tanadchangsaeng N., Yu J.: Miscibility of natural polyhydroxyalkanoate blend with controllable material properties. Journal of Applied Polymer Science, **129**, 2004–2016 (2013). DOI: 10.1002/app.38906

[8] Madden L. A., Anderson A. J., Asrar J.: Synthesis and characterization of poly(3-hydroxybutyrate) and poly(3-hydroxybutyrate-*co*-3-hydroxyvalerate) polymer mixtures produced in high-density fed-batch cultures of *Ralstonia eutropha* (*Alcaligenes eutrophus*). Macromolecules, **31**, 5660–5667 (1998). DOI: 10.1021/ma980606w

[9] Doi Y., Kitamura S., Abe H.: Microbial synthesis and characterization of poly(3-hydroxybutyrate-*co*-3-hydroxyhexanoate). Macromolecules, **28**, 4822–4828 (1995). DOI: 10.1021/ma00118a007

[10] Parulekar Y., Mohanty A. K.: Biodegradable toughened polymers from renewable resources: Blends of polyhydroxybutyrate with epoxidized natural rubber and maleated polybutadiene. Green Chemistry, **8**, 206–213 (2006). DOI: 10.1039/B508213G

[11] Basnett P., Ching K. Y., Stolz M., Knowles J. C., Boccaccini A. R., Smith C., Locke I. C., Keshavarz T., Roy I.: Novel poly(3-hydroxyoctanoate)/poly(3-hydroxybutyrate) blends for medical applications. Reactive and Functional Polymers, **73**, 1340–1348 (2013). DOI: 10.1016/j.reactfunctpolym.2013.03.019

[12] de O. Patrício P. S., Pereira F. V., dos Santos M. C., de Souza P. P., Roa J. P. B., Orefice R. L.: Increasing the elongation at break of polyhydroxybutyrate biopolymer: Effect of cellulose nanowhiskers on mechanical and thermal properties. Journal of Applied Polymer Science, **127**, 3613–3621 (2013). DOI: 10.1002/app.37811

[13] Fei B., Chen C., Wu H., Peng S., Wang X., Dong L., Xin J. H.: Modified poly(3-hydroxybutyrate-*co*-3-hydroxyvalerate) using hydrogen bonding monomers. Polymer, **45**, 6275–6284 (2004). DOI: 10.1016/j.polymer.2004.07.008

[14] Dong W., Ma P., Wang S., Chen M., Cai X., Zhang Y.: Effect of partial crosslinking on morphology and properties of the poly(β-hydroxybutyrate)/poly(D,L-lactic acid) blends. Polymer Degradation and Stability, **98**, 1549–1555 (2013). DOI: 10.1016/j.polymdegradstab.2013.06.033

[15] de Koning G. J. M., Lemstra P. J.: Crystallization phenomena in bacterial poly[(*R*)-3-hydroxybutyrate]: 2. Embrittlement and rejuvenation. Polymer, **34**, 4089–4094 (1993).
DOI: 10.1016/0032-3861(93)90671-V

[16] Calvão P. S., Chenal J-M., Gauthier C., Demarquette N. R., dos Santos A. M., Cavaille J. Y.: Influence of the rubbery phase on the crystallinity and thermomechanical properties of poly(3-hydroxybutyrate)/elastomer blends. Polymer International, **59**, 851–858 (2010).
DOI: 10.1002/pi.2799

[17] Chiu H-J.: Miscibility and crystallization kinetics of poly(3-hydroxybutyrate-*co*-3-hydroxyvalerate)/poly (methyl methacrylate) blends. Journal of Applied Polymer Science, **91**, 3595–3603 (2004).
DOI: 10.1002/app.13592

[18] Parra D. F., Fusaro J., Gaboardi F., Rosa D. S.: Influence of poly (ethylene glycol) on the thermal, mechanical, morphological, physical–chemical and biodegradation properties of poly(3-hydroxybutyrate). Polymer Degradation and Stability, **91**, 1954–1959 (2006).
DOI: 10.1016/j.polymdegradstab.2006.02.008

[19] Hay J. N., Sharma L.: Crystallisation of poly(3-hydroxybutyrate)/polyvinyl acetate blends. Polymer, **41**, 5749–5757 (2000).
DOI: 10.1016/S0032-3861(99)00807-1

[20] He M. J., Chen X. W., Dong X. X.: Polymer physics (in Chinese). Fu Dan University Press, Shanghai (2005).

[21] Meijer H. E. H., Govaert L. E.: Mechanical performance of polymer systems: The relation between structure and properties. Progress in Polymer Science, **30**, 915–938 (2005).
DOI: 10.1016/j.progpolymsci.2005.06.009

[22] L'Abee R. M. A., van Duin M., Spoelstra A. B., Goossens J. G. P.: The rubber particle size to control the properties-processing balance of thermoplastic/cross-linked elastomer blends. Soft Matter, **6**, 1758–1768 (2010).
DOI: 10.1039/b913458a

[23] Wiyatno W., Fuller G. G., Pople J. A., Gast A. P., Chen Z-R., Waymouth R. M., Myers C. L.: Component stress–strain behavior and small-angle neutron scattering investigation of stereoblock elastomeric polypropylene. Macromolecules, **36**, 1178–1187 (2003).
DOI: 10.1021/ma020477q

[24] Kakroodi A. R., Rodrigue D.: Degradation behavior of maleated polyethylene/ground tire rubber thermoplastic elastomers with and without stabilizers. Polymer Degradation and Stability, **98**, 2184–2192 (2013).
DOI: 10.1016/j.polymdegradstab.2013.08.017

[25] Wu W., Wan C., Zhang Y.: Morphology and mechanical properties of ethylene-vinyl acetate rubber/polyamide thermoplastic elastomers. Journal of Applied Polymer Science, **130**, 338–344 (2013).
DOI: 10.1002/app.39046

[26] Zhou Z., Zhang X., Zhang W., Li J., Lu C.: Microstructure and properties of solvent-resistant fluorine-contained thermoplastic vulcanizates prepared through dynamic vulcanization. Materials and Design, **51**, 658–664 (2013).
DOI: 10.1016/j.matdes.2013.04.070

[27] Hrdlička Z., Kuta A., Poręba R., Špírková M.: Polycarbonate-based polyurethane elastomers: Temperature-dependence of tensile properties. Chemical Papers, **68**, 233–238 (2014).
DOI: 10.2478/s11696-013-0439-0

[28] Huy T. A., Adhikari R., Michler G. H.: Deformation behavior of styrene-*block*-butadiene-*block*-styrene triblock copolymers having different morphologies. Polymer, **44**, 1247–1257 (2003).
DOI: 10.1016/S0032-3861(02)00548-7

[29] Barham P. J., Keller A., Otun E. L., Holmes P. A.: Crystallization and morphology of a bacterial thermoplastic: Poly-3-hydroxybutyrate. Journal of Materials Science, **19**, 2781–2794 (1984).
DOI: 10.1007/BF01026954

*eXPRESS Polymer Letters Vol.8, No.7 (2014) 528–542*
*Available online at www.expresspolymlett.com*
*DOI: 10.3144/expresspolymlett.2014.56*

# Dual-switchable surfaces between hydrophobic and superhydrophobic fabricated by the combination of click chemistry and RAFT

*M. S. Han, X. Y. Zhang, L. Li, C. Peng, L. Bao, E. C. Ou, Y. Q. Xiong, W. J. Xu**

Institute of Polymer Science and Technology, College of Chemistry and Chemical Engineering, Hunan University, 410082 Changsha, P.R. China

*Received 1 January 2014; accepted in revised form 1 April 2014*

**Abstract.** A dual-switchable surface between hydrophobic and superhydrophobic has been fabricated successfully by combining reversible addition-fragmentation chain transfer polymerization (RAFT) polymeric technology and thiol-NCO click chemistry. Well-defined block copolymer, poly(7-(6-(acryloyloxy) hexyloxy) coumarin)-*b*-poly(N-Isopropylacryl amide), was synthesized by RAFT, and then the block copolymer was grafted onto the surface of $SiO_2$ modified by toluene disocynate (TDI) via thiol-NCO click chemistry. The results of nuclear magnetic resonance (NMR) and Fourier Transform Infrared (FTIR) spectroscopies confirmed that the block copolymer (Number average molecular weight ($M_n$) = 9400, polydispersity index (PDI) = 1.22) has been synthesized successfully. The static contact angle (CA) of the surface prepared by $SiO_2$/P (7-6-AC)-*b*-PNIPAAm switches from 98±2 to 137±2° by adjusting the temperature. Furthermore, the contact angle can also oscillate between 137±2 and 157±2° on the irradiation of UV light at 365 and 254 nm, respectively. The dual-switchable surfaces exhibit high stability between hydrophilicity and superhydrophobicity. Therefore, the method provides a new method to fabricate the dual-stimuli-responsive surface with tunable wettability, reversible switching, and also be easily extended to other dual-responsive surfaces. This ability to control the wettability by the adjustment of the temperature and UV light has applications in a broad range of fields.

***Keywords:*** *polymer composites, superhydrophobic surface, photo-sensitive, thermal-sensitive, click chemistry*

## 1. Introduction

The wetting properties of superhydrophobic surfaces have received worldwide and tremendous attention [1] since the dual hierarchical structure of the lotus leaf was discovered [2]. Lotus-Leaf-like superhydrophobic surfaces, exhibit an amazing property for not only being wetted by water leading to a self-cleaning effect [3], but also for their great advantages in applications. In recent years, superhydrophobic surfaces are widely used in the human body implant materials [4], microfluidic tools [5], Calix azacrown [6], tunable optical lenses [7], lab-on-chip systems [8]. The wettability of the surface is influenced by its chemical composition and morphology [9], because chemical composition determines the surface free energy, and a lower surface energy leads to higher hydrophobicity. Additionally, the hierarchical structure (micro roughness covered with nano roughness) was not only necessary for a high contact angle (CA) but essential for the stability of the water-solid and water-air interfaces [10] (the composite interface). For example, Wang *et al*. [11] prepared cauliflower-like silica nanospheres with tunable wettability through regulating chemical compositions. The chemical etching method [12] used to prepare the superhydrophobic CuO

*Corresponding author, e-mail: weijianxu59@gmail.com

surfaces with tunable adhesion by controlling the etching time to control the morphology. However, these reports mainly focused on realizing controllable wettability by different means, rather than the reversibility and did not consider the transition of the reversible.

Functional surfaces with controlled wetting properties responsive to external stimuli become more attractive for both the scientific interest and the practical application due to the wide range of their potential applications. A variety of approaches including appropriate external stimuli [13], and exchange of counterions [14] can dynamically trigger the reversible wettability conversion. The external stimuli-responsive superhydrophobic materials have been intensively studied, and many positive results have also been obtained [15]. External stimuli, such as light illumination [16], temperature [17], curvature driven [18], ion pairs driven [19], pH [20], can change the surface conformation or morphology of stimuli-sensitive materials, thus resulting in the change of wettability. However, most of these wetting surfaces are responsive to only single stimulus, such as temperature, optical or electric field, and this may be the limitation in many important practical applications with complex environments, such as biological devices, which often need the surface can respond to more than one stimulus simultaneously [21]. It is, therefore, desirable to design dual- or multiresponsive surfaces to meet with the needs of double or multi-stimulation in complex environments.

Multiple functional and responsive surfaces with special wettability and reversible properties, especially thermal-sensitive and photo-sensitive surfaces, have an extensive range of application in many important fields [22–24]. Recently, several thermally, pH, or optically responsive smart interfacial materials that can switch between superhydrophilicity and superhydrophobicity or hydrophobicity and superhydrophobicity have been reported [25–27]. For the responsive superhydrophobic surfaces, it is necessary to graft some responsive groups, onto the surface of inorganic materials or organic compounds for example, a temperature-responsive polymer poly (N-isopropyl acrylamide (PNIPAAm) [28], reversible pH-responsive group [29], photosensitive materials [30], such as spiropyram [31], coumarin [32] and azobenzene [33, 34]. Therefore, grafting functional group or polymer with a responsive group onto the inorganic sphere surface to construct multi-responsive superhydrophobic materials is a feasible method, and the most effective method to achieve the goal is the click chemistry [35] which can fabricate the core-shell structure. Additionally, it is convenient to tune the surface roughness by controlling click reaction cycles [35, 36] to obtain hierarchical structures with different sizes of $SiO_2$. Coumarin and its derivatives are one of the most common used to prepare for photo-sensitive materials, such as the superhydrophobic materials [32], which are potentially applied in biological and medical fields [37–39]. Reversible addition-fragmentation chain transfer polymerization (RAFT) is an effective method to synthesize living/controlled polymer and now have been applied in polymerizing PVAc [40], PHEMA [41], P4VP [42], PNIPAAm [43], PS [44] etc. The high degree of compatibility with a wide range of functional monomers and good tolerance of water and oxygen in the systems make RAFT technique has been widely used in the synthesis of functional polymers. For example, coumarin and its derivatives have been successfully grafted onto the chain of polymer by living free radical polymerization [45, 46].

In this work, we report a method for the fabrication of photo- and thermal-sensitive superhydrophobic surface by the combination of RAFT and click chemistry, resulting in that the block polymers are grafted onto the surface of silica nanosphere. The strategies in our work not only improve the grafting rate between the organic group and inorganic materials by click chemistry (thiol-NCO), but also increase the stability of the superhydrophobic materials. Moreover, the copolymers containing coumarin and N-isopmpylacrylamide group can be easily synthesized by RAFT polymeric technology, and a superhydrophobic surface can be designed and constructed by using the multiple responsive block polymers which synthesized by RAFT polymeric technology. To the best of our knowledge, it is the first time to fabricate photo-sensitive and thermal-sensitive superhydrophobic surfaces by the combination of 'click' chemistry and RAFT polymeric technology, and graft the block polymer onto the silica surface. Therefore, it would provide a new pathway to fabricate multiple responsive superhydrophobic surfaces, and other responsive superhydrophobic surfaces can be designed and prepared by this method.

## 2. Experimental section

### 2.1. Materials

All the other chemicals were analytical grade and used as received without further purification. 7-Hydroxy coumarin (7-AC) was received from Ziyan Chemical Co. Ltd (Lianyungang, China). 1,6-dibromohexane , silica nanoparticle and N-Isopropylacrylamide (NIPAAm recrystallized twice from benzene/hexane) was purchased from Aladdin Co. Ltd. (Shanghai, China). 2-Cyanoprop-2-yl-dithiobenzoate (CPDB), N, N-dimethyl-formamide (DMF), petroleum ether and ethyl acetate were purchased from Sinopharm Chemical Reagent Co. Ltd (Shanghai, China). Carbonic acid, ethanol, acrylic acid, potassium hydroxide, dibutyltin dilaurate (DBTDL), toluene di-isocyanate (TDI) and azodiisobutyronitrile (AIBN) were commercially available from Tianjin Damao Chemical Reagent Company (Tianjin, China), respectively.

### 2.2. Synthesis of 7-(6-bromohexyloxy) coumarin

The mixture of 7-hydroxy coumarin (10.0 g, 62 mmol) and excess 1,6-dibromohexane (45 g, 186 mmol) were dissolved in acetone (200 mL), then anhydrous $K_2CO_3$ (17.4 g, 124 mmol) was added into the flask. The resulted suspension was heated to reflux for 24 h. The precipitate was filtered off and extracted with acetone (3×100 mL). After the solvent was removed in reduced pressure, water was added, and used $CH_2Cl_2$ (3×200 mL) to extract the residue. The extract was dried with anhydrous $MgSO_4$, filtered, and evaporated under reduced pressure. The product was then purified by means of column chromatography on silica oxide with mixed petroleum ether and ethyl acetate (5:1, v/v) as eluent, and resulted in a white solid after dried in vacuum drying oven (14.8 g, 74.3%). The synthesis route of 7-(6-bromohexyloxy) coumarin (7-6-BC) is shown in Figure 1a.

$^1$H NMR($CDCl_3$): 7.65(d, 1H), 7.38(d, 1H), 6.82(d, 1H), 6.80(d, 1H), 4.02(t, 2H), 3.43(t, 2H), 1.90(m, 4H), 1.50(m, 4H).

### 2.3. Synthesis of 7-(6-(acryloyloxy) hexyloxy) coumarin

7-(6-bromohexyloxy) coumarin (5.8 g, 18 mmol) and excess potassium acrylate (30 g, 27 mmol) were dissolved in ethanol (150 mL). Hydroquinone (0.02 g, 1.8 mmol) was added. The solution was heated to reflux for 24 h. The precipitate was filtered off and extracted with ethanol (3×50 mL). After the solvent was removed in reduced pressure, water was added, and the residue was extracted with $CH_2Cl_2$ (3×100 mL). The residue was then purified by means of column chromatography on silica oxide with mixed petroleum ether and ethyl acetate (3:1, v/v) as an eluent and resulted in a white solid after dried in vacuum drying oven (4.6 g, 81.65%). The synthesis process of 7-(6-(acryloyloxy) hexyloxy) coumarin (7-6-AC) is presented in Figure 1b.

$^1$H NMR($CDCl_3$): 7.65(d, 1H), 7.37(d, 1H), 6.80(m, 2H), 6.41(d, 1H), 6.26(d, 1H), 6.18(m, 1H), 5.82(t, 1H), 4.20(t, 2H), 4.03(t, 2H), 1.83(m, 2H), 1.65(m, 2H), 1.5(m, 4H).

### 2.4. Polymerization of 7-(6-(acryloyloxy) hexyloxy) coumarin by RAFT

A dry ampoule was filled with 7-(6-(acryloyloxy) hexyloxy) coumarin (0.5 g, 1.58 mmol), AIBN (1.3 mg, 0.0079 mmol), CPDB (8.75 mg, 0.0395 mmol), and N,N-dimethylformamide (DMF) (1.5 mL). The Schlenk line was used to keep the ampoule vacuum and filled with nitrogen. Then, the ampoule was placed in an oil bath at the desired temperature to polymerize. At timed intervals, the ampoule was immersed into icy water and then opened. The suspension liquid in the ampoule was dissolved in 2 mL of tetrahydrofuran (THF) and precipitated into a 200 mL of methanol. The polymer was obtained by centrifuge at the speed of 15 000 rpm and dried at room temperature. The synthesis process of poly7-(6-(acryloyloxy) hexyloxy) coumarin (P(7-6-AC)) is presented in Figure 1c.

### 2.5. Synthesis of P(7-6-AC)-*b*-PNIPAAm

P7-6-AC (0.1 mmol, $M_n$ = 8300), AIBN (5.47 mg, 0.033 mmol), NIPAAm (1.13 g, 10 mmol) were placed in an ampoule (The volume fraction of block copolymer was 30:10 ), the schlenk line was used to keep the ampoule vacuum and fill with nitrogen, and the process must be repeated at least 3 times or more. Then DMF (1.5 mL) was added into the ampoule by syringe. The ampoule was placed in an oil bath at the desired temperature. At timed intervals, the suspension liquid in the ampoule was poured into 200 mL of methanol. The polymer was obtained by the centrifuge at the speed of 15 000 rpm and dried

at room temperature. The scheme and structure for the synthesis of P(7-6-AC)-*b*-PNIPAAm are described in Figure 1d.

### 2.6. Reduction of the end group of P(7-6-AC)-*b*-PNIPAAm

The P(7-6-AC)-*b*-PNIPAAm (0.5 g, $M_n$ = 9400) was dissolved in THF (10 mL), then the NaBH4 (114 mg, 3 mmol) was added into the solution by three times very slowly, stirring for 30 min under ice salt bath, and the exhaust system must be kept unobstructed. At last, the icy water was used to quench the activity of $NaBH_4$. The solvent was extracted by $CH_2Cl_2$ (3×50 mL). Finally, $CH_2Cl_2$ was eliminated by rotating distillation, and solid samples were dried in vacuum at 35°C overnight. The synthetic route is shown in Figure 1e.

### 2.7. Decoration of silica with toluene diisocyanate

Silica nanosphere (14 nm) should be activated in a vacuum drying oven at 110°C overnight, then the silica (0.4 g) was dispersed evenly in ethyl acetate (120 mL) by ultrasonic cleaner, then DBTDL (0.5 mL) and TDI (2 mL) were appended in the reaction system, the flask was placed into an oil bath and heated to 60°C for 6 h under the nitrogen atmosphere. The final product was separated at the speed of 4000 rpm in centrifuge. Then the products were dried overnight at 60°C. Schematic representation of the modified silica nanosphere with TDI is given in Figure 2a.

### 2.8. The grafting of P(7-6-AC)-*b*-PNIPAAm onto the surface of $SiO_2$

The reduced P(7-6-AC)-*b*-PNIPAAm (0.5 g) and silica modified with TDI (0.1 g) were dissolved in THF (50 mL). DBTDL (0.25 mg) as catalyst was added. The solution was heated to 40°C for 2 h under the nitrogen atmosphere. The $SiO_2$/P(7-6-AC)-*b*-PNIPAAm was obtained after being centrifuged and dried. Schematic representation of the modified silica nanosphere with TDI is given in Figure 2b.

### 2.9. Preparation of the film to measure the contact angles

Silicon wafers were ultrasonically cleaned in water and acetone for 10 min, respectively. Then the as-prepared $SiO_2$/P(7-6-AC)-*b*-PNIPAAm dispersions were coated on the silicon wafer, and dried at room temperature for 24 h. The static water contact angles were measured with deionized water (4 μL) on a contact angle goniometer (JC2001) instrument at room

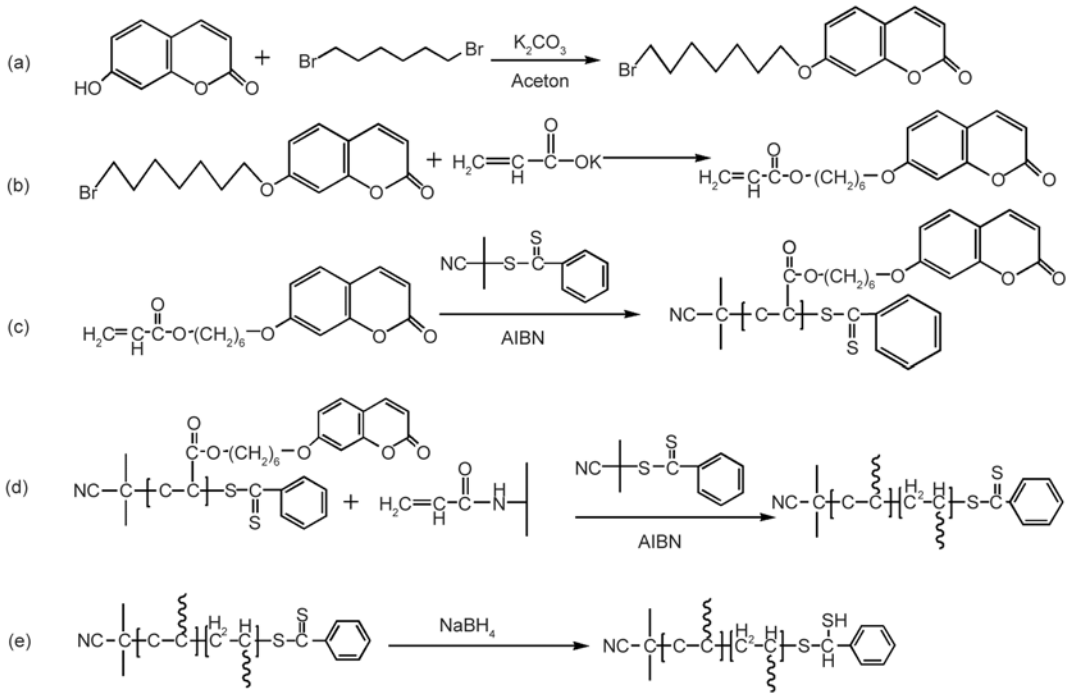


**Figure 1.** The scheme and structure for the synthesis of (a) 7-(6-bromohexyloxy) coumarin, (b) 7-(6-(acryloyloxy) hexyloxy) coumarin, (c) poly 7-(6-(acryloyloxy) hexyloxy) coumarin, (d) P(7-6-AC)-*b*-PNIPAAm, and (e) the reduction of the end group of P(7-6-AC)-*b*-PNIPAAm

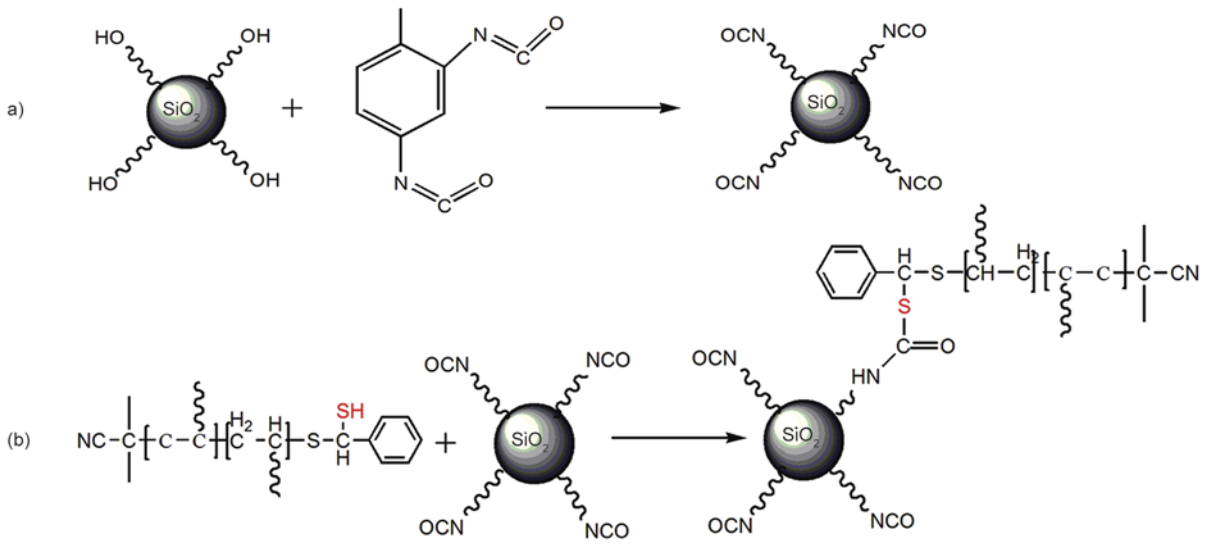


**Figure 2.** Synthesis route of (a) silica nanosphere modified with TDI, and (b) $SiO_2$/P(7-6-AC)-*b*-PNIPAAm

temperature. The contact angles were measured at three different points for each sample surface, and the average values were reported here. The static water contact angles were further measured after the irradiation of UV light at 365 and 254 nm, respectively.

### 2.10. Characterization

The morphologies of functional silica particles were observed using transmission electron microscope (TEM) (JEOL JEM-2000EXII, Japan). FT-IR analysis was used to confirm the TDI functionalized $SiO_2$ particles and P (7-6-AC)-*b*-PNIPAAm grafted with $SiO_2$ particles. All FT-IR spectra were recorded at room temperature on a Magna-IR 760 (Nicolet, USA) spectrometer using 32 scans at an instrument resolution of 4 $cm^{-1}$. Ultraviolet spectrophotometer (Iambda 35, Perkin Elmer, Germany) was used to confirm the copolymer successfully grafted with functioned $SiO_2$ and the transformation of absorbance under 365 and 254 nm UV irradiation. Thermal gravimetric analysis (TGA) (TGA 7, Perkin Elmer, Germany) was performed to analyze the weight-loss percent of the organic component. The particles were heated from 20 to 600°C at the heating rate of 10°C/min under nitrogen atmosphere with the rate of 50 mL/min. And the Attension Theta Lite (Attension, Finland) was used to measure the contact angle of the $SiO_2$ particles as prepared.

## 3. Results and discussion

### 3.1. Preparation of P(7-6-AC)-*b*-PNIPAAm by RAFT

The structures of 7-6-AC, P(7-6-AC) and P(7-6-AC)-*b*-PNIPAAm were characterized by $^1$H NMR. The $^1$H NMR spectra of the 7-6-AC, P(7-6-AC) and P(7-6-AC)-*b*-PNIPAAm are shown in Figure 3, respectively. Compared with 7-6-AC (Figure 3a), the signals (5.84, 6.23 and 6.40 ppm ($CH_2$=CH–)) of P(7-6-AC) disappear in Figure 3b. It clearly demonstrates that the double bond in the long chain has been polymerized. In Figure 3c, the new signal (7.95 ppm (O=C–N–H)) could be assigned to the amide group in the repeat unit of PNIPAAm structure introduced into P(7-6-AC)-*b*-PNIPAAm. The signals of ppm = 6.2, ppm = 6.6, ppm = 6.8, ppm = 7.3, ppm = 7.6 were attributed to the coumarin group in 7-6-AC, P(7-6-AC) and P(7-6-AC)-*b*-PNIPAAm. All the results indicate that the P(7-6-AC)-*b*-PNIPAAm with the end group which can easily restore to sulfhydryl has been synthetized successfully.

The P(7-6-AC) ($M_n$ = 8100 g/mol, PDI = 1.17) as the macro-RAFT agent, which reacted with NIPAAm to obtain the block polymer. Gel permeation chromatographic (GPC) curves (Figure 4) demonstrates that there was an increase in the molecular weights (from 8100 to 9400 g/mol) after chain extension. However, the value of PDI increases from 1.17 to 1.22 with the chain extension of the polymer. The

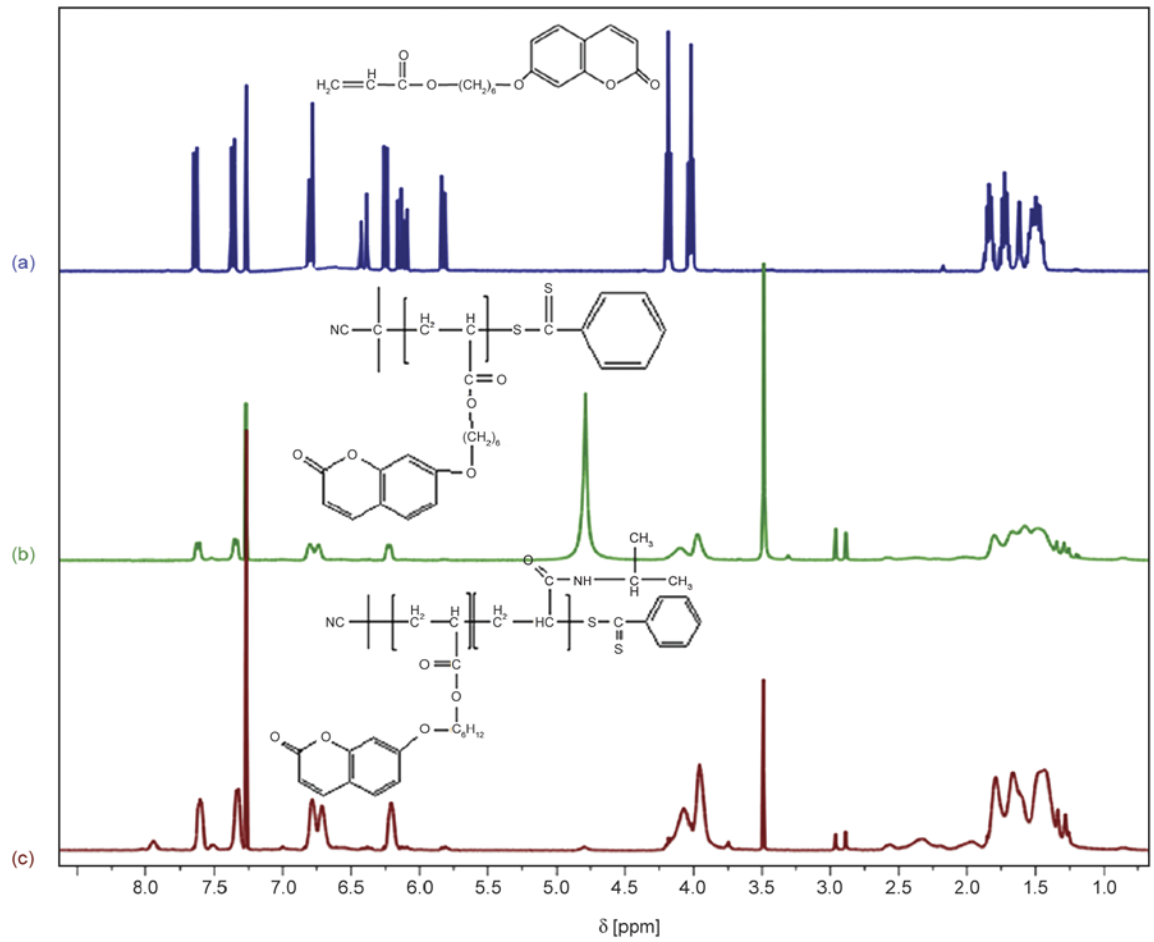


**Figure 3.** $^{1}$H NMR spectra of (a) 7-6-AC, (b) P(7-6-AC) and (c) P(7-6-AC)-*b*-PNIPAAm

increase can be due to the increase of the block and the molecular weight of the P(7-6-AC)-*b*-PNIPAAm.

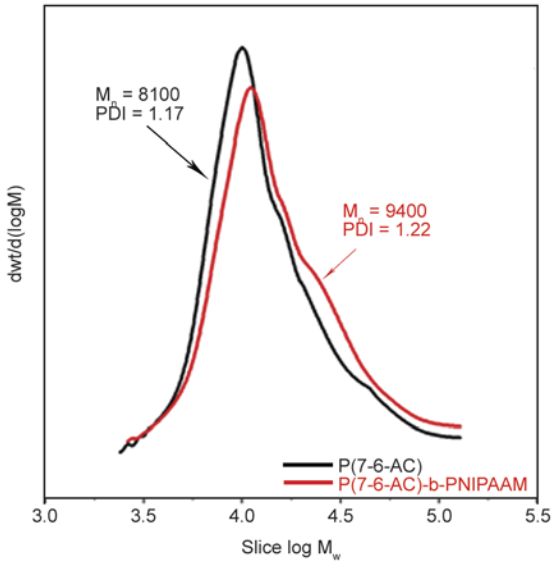


**Figure 4.** GPC curves of the original macro-RAFT agent (P(7-6-AC)) and the chain extended block copolymer P(7-6-AC)-*b*-PNIPAAm in THF solution

### 3.2. Fabrication of $SiO_2$/P(7-6-AC)-*b*-PNIPAAm composites

Figure 5 presents the FT-IR spectra (I), contact angles (II) and TGA profile (III) of (a) pure $SiO_2$, (b) $SiO_2$/TDI and (c) $SiO_2$/P(7-6-AC)-*b*-PNIPAAm, respectively. In Figure 5(I) a, the peaks at 1105 cm$^{-1}$ and the shoulder part between the bands of 1100–1300 cm$^{-1}$ correspond to the concerted (Si–O–Si) stretches. Compared with the spectra of pure $SiO_2$, the intensity of the peak at 2276 cm$^{-1}$ (Figure 5(I)b) corresponded to the characteristic absorption peak of –NCO group, and the typical benzene ring absorption bands at 1500–1600 cm$^{-1}$ are clearly found, implying that the TDI has been grafted successfully onto the surface of $SiO_2$. The absorption peak of 3167 cm$^{-1}$ in Figure 5(I)c demonstrate the existence of amide group, and the absorption appearing at 974 cm$^{-1}$ implies that the –CH–$CH_2$– groups existed on the surface of $SiO_2$ nanosphere. These results suggest that P(7-6-AC)-*b*-PNIPAAm has been successfully grafted onto the surface of $SiO_2$ nanosphere by RAFT and thiol-NCO click chemistry.

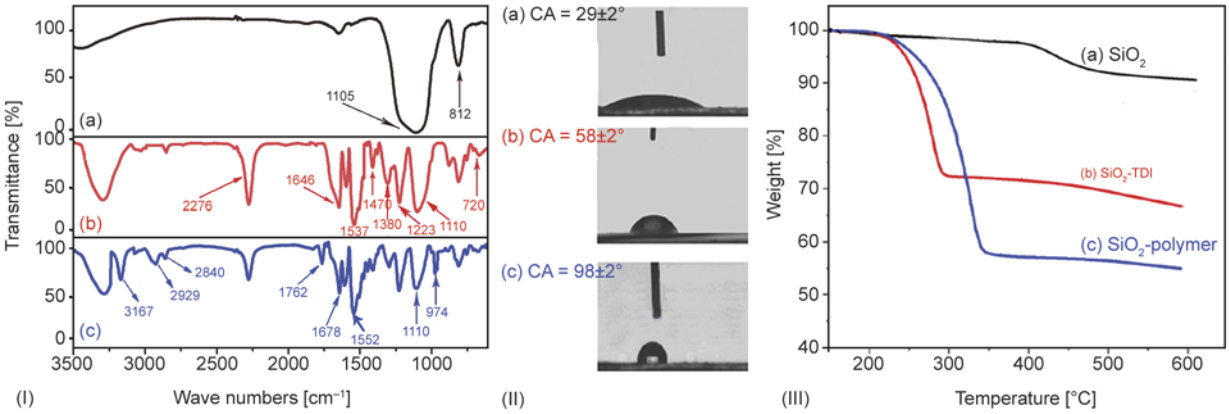


**Figure 5.** The FT-IR spectra (I), contact angles (II) and TGA (III) profile of (a) pure $SiO_2$, (b) $SiO_2$/TDI and (c) $SiO_2$/P(7-6-AC)-*b*-PNIPAAm, respectively

Moreover, the typical absorption of the cyclic lactones group appears at 1762 $cm^{-1}$, which further demonstrated that the $SiO_2$/P(7-6-AC)-*b*-PNIPAAm composites were synthesized. the characteristic absorptions at 2929 and 2840 $cm^{-1}$ are assigned to the vibration of $–CH_2–$ groups, the correlative peak of $–CH_3$ group, and the peaks at 1470, 1380, 720 $cm^{-1}$ can be assigned to the out-of-plane and in plane bending vibration of $–CH_3$ group. Additionally, the absorption peak at 2276 $cm^{-1}$ (Figure 5(I)c) can be attributed to the residual –NCO groups remaining on the surface of $SiO_2$/TDI, which did not react with –SH. The results can also be considered to the identification of the $SiO_2$/P(7-6-AC)-*b*-PNIPAAm by the TEM images, which show a core-shell structure.

In Figure 5(II), the contact angles of $SiO_2$, $SiO_2$/TDI and $SiO_2$/P(7-6-AC)-*b*-PNIPAAm were 29±2, 58±2 and 98±2°, respectively. The results imply that the wettability has been changed after the modification of TDI and P(7-6-AC)-*b*-PNIPAAm on the surface of $SiO_2$. Low contact angles (29±2°) of pure $SiO_2$ can be explained by the fact that many hydrophilic groups (hydroxyl groups) covered on the pure $SiO_2$ surface. As for $SiO_2$/TDI, the contact angles increases up to 58±2° for the hydrophobic group of TDI on the surface of $SiO_2$, which further demonstrated that PDI has been grafted on $SiO_2$. The sulfhydryl group on P(7-6-AC)-*b*-PNIPAAm as the terminal group can react with the portion of –NCO group on $SiO_2$/TDI surface. Therefore, the $SiO_2$ particles covered with –NCO group and P(7-6-AC)-*b*-PNIPAAm possess a higher hydrophobic surface and higher contact angles, and the high contact angle (98±2°) was primarily attributed to P(7-6-AC)-*b*-PNIPAAm, which own lower surface energy than inorganic molecule.

The thermal behavior of the $SiO_2$, $SiO_2$/TDI and $SiO_2$/P(7-6-AC)-*b*-PNIPAAm was investigated by TGA in $N_2$ for comparison, which serves to confirm the percentage of the particles surrounding by organic phase. Figure 5(III) shows the TGA analysis of the bare $SiO_2$, $SiO_2$-PDI, and $SiO_2$-P(7-6-AC)-*b*-PNIPAAm. As shown in Figure 5(III)a, the main temperature regions of weight loss appear in the interval 400–500°C, which can be assigned to the dehydration condensation reaction of the hydroxyl on the silica surface , and the chemical reaction equations can be expressed as Equation (1) [47]:

$$Si–OH + Si– OH \rightarrow –Si–O–Si– + H_tO \quad (1)$$

Figure 5(III)b, 5(III)c describes the thermal behavior of $SiO_2$/TDI and $SiO_2$-P(7-6-AC)-*b*-PNIPAAm, The results show the weight loss with 4.73% of $SiO_2$/TDI and $SiO_2$-P(7-6-AC)-*b*-PNIPAAm was 27.2, 41.1%, respectively, and the peak pyrolysis temperatures of $SiO_2$/TDI and $SiO_2$-P(7-6-AC)-*b*-PNIPAAm are 291.4 and 349.4°C. According to the reference [48], the surface grafting density of $SiO_2$-TDI and $SiO_2$-P(7-6-AC)-*b*-PNIPAAm was calculated to be about 1.29 mmol/g (0.222 g/g) and 0.02 mmol/g (0.188 g/g) respectively. Obviously, the graft density obtained from 'click chemistry' is higher than that of the traditional and classic method [49, 50], for example $SiO_2$ surface silanization using silane coupling agent.

### 3.3. The responsive switch of $SiO_2$/P (7-6-AC)-*b*-PNIPAAm composites

It is well known that the properties of the block polymer determined by the different ratio of its two blocks. In P(7-6-AC)-*b*-PNIPAAm, the first block

P(7-6-AC) may cause the cross-linking because of the existence of coumarin group. If the ratio of the coumarin block too high, the PDI will out of 1.2 and the cross-linking of the coumarin will change the property of the polymer. For the second block, because of strong hydrophilicity of the amido group, the high ratio of the NIPAAm will enhance the hydrophilicity and the contact angles of the prepared nanoparticles will less than 150°. On the other hand, while the ratio is too low, the thermal-sensitive features are not obvious. In fact, a variety of block polymers with different block unit, such as 10, 15, 20, 25, 30, 50 polymerization units, have been synthesized. The thermal-sensitive characteristics and the contact angles of the $SiO_2$/P(7-6-AC)-*b*-PNIPAAm composites with different ratio of P(7-6-AC) and PNIPAAm is summarized in Table 1. Finally, we choose the largest molecular weight in PDI under 1.2 as the target product ($M_n$ = 8100, PDI =1.17, 25 units) to graft onto the surface of silica nanosphere. The photoresponse of the prepared $SiO_2$/P(7-6-AC)-*b*-PNIPAAm was monitored by UV-Vis spectra by the exposure of the clear dilute suspension of $SiO_2$/P(7-6-AC)-*b*-PNIPAAm in THF under different wavelengths (365 and 254 nm) of UV light. As illustrated in Figure 6a and the absorbed intensity of

**Table 1.** The thermal-sensitive characteristics and the contact angles of the $SiO_2$/P(7-6-AC)-*b*-PNIPAAm composites with different ratio of P(7-6-AC) and PNIPAAm

| The ratio of P(7-6-AC) and PNIPAAm | The thermal-sensitive characteristics | The contact angles of the prepared nanoparticles |
|---|---|---|
| 30:5 | Not obvious | 159±2° |
| 30:10 | Obvious | 157±2° |
| 30:20 | Obvious | 148±2° |
| 30:30 | Obvious | 141±2° |

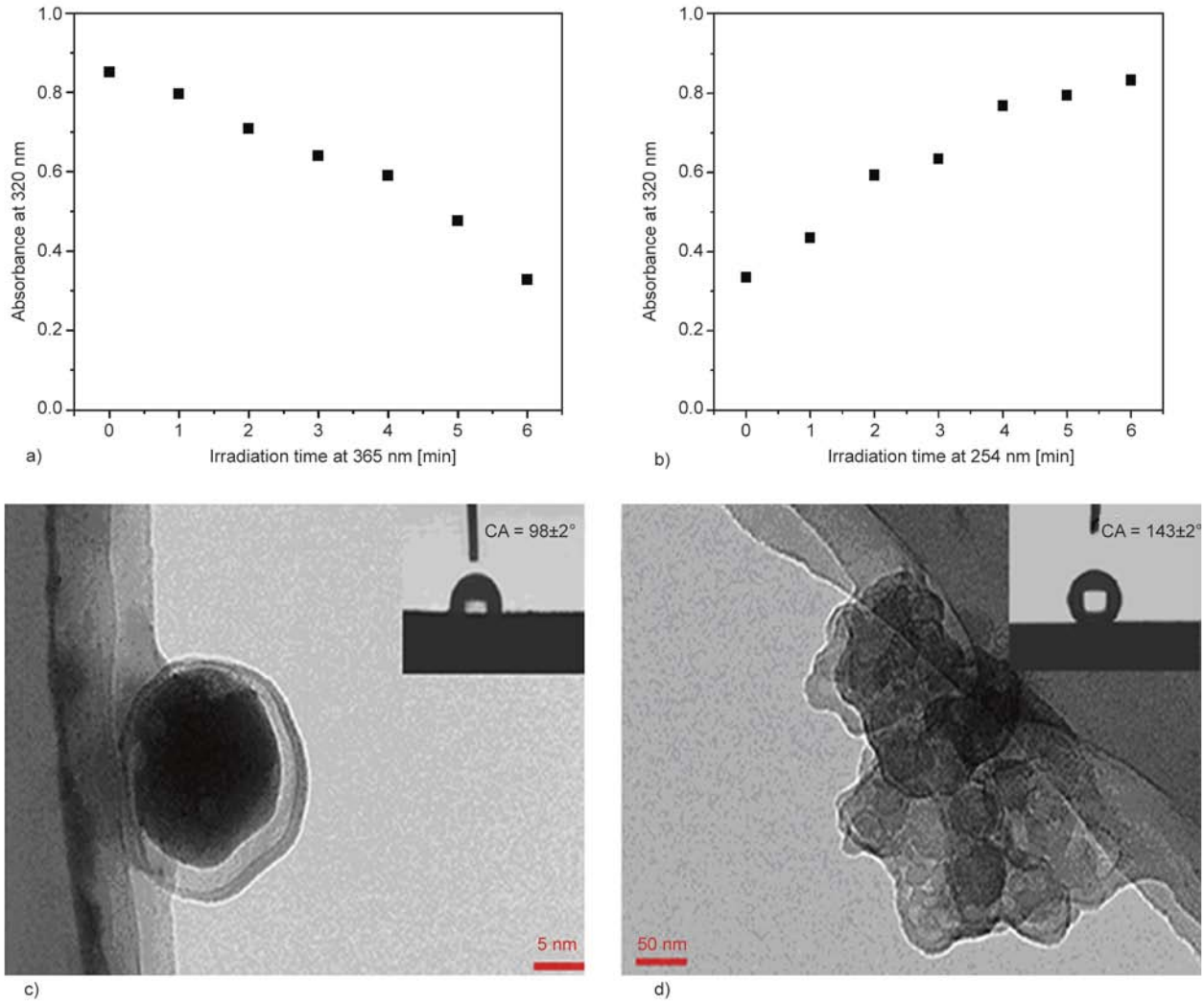


**Figure 6.** The absorbance at 320 nm according to the exposure time under the irradiation of 356 nm (a) and the subsequent irradiation at $\lambda$ = 254 nm (b); TEM images of the prepared $SiO_2$/P(7-6-AC)-*b*-PNIPAAm (c) and its aggregations (d) under 365 nm irradiation

coumarin at 320 nm (characteristic absorption peak) decreases continuously with the exposure time under UV irradiation at 365 nm (Figure 6b). To the contrast, the absorbance at 320 nm starts to increase for the photocleavage of coumarin after exposure under the irradiation of 254 nm UV light (Figure 6b) [51]. This interconversion between hydrophobic and superhydrophobic can attributed to the reversible photodimerization and photocleavage of the coumarin group on $SiO_2$/P(7-6-AC)-*b*-PNIPAAm under UV irradiation at different wavelengths.

The reversible photodimerization and photocleavage of $SiO_2$/P (7-6-AC)-*b*-PNIPAAm are also studied by TEM. As presented in Figure 6c, a well-defined core-shell structure (20–30 nm) with $SiO_2$ nanospheres as core and block polymer as shell has been observed. It suggested that the $SiO_2$ particles were surrounded by P(7-6-AC)-*b*-PNIPAAm with a thickness of about 3 nm. Moreover, the silica nanoparticles modified by P(7-6-AC)-*b*-PNIPAAm is dispersive spherical particle with the size of 50 nm before the exposure of UV light. On the contrary, the $SiO_2$/P(7-6-AC)-*b*-PNIPAAm nanoparticle aggregated after the irradiation of UV light (365 nm), and the size of the aggregations increased up to 300 nm, suggesting that $SiO_2$/P(7-6-AC)-*b*-PNIPAAm have been cross-linked together by the photodimerization of the coumarin under UV light at 365 nm irradiation (Figure 6d).

Figure 7 shows AFM and SEM images of the single and aggregations of $SiO_2$/P(7-6-AC)-*b*-PNIPAAm. Compared with the results of TEM, the aggregations of the $SiO_2$/P(7-6-AC)-*b*-PNIPAAm were also observed by AFM and SEM (Figure 7b and 7d) [52]. On Figure 7a, we can find that the $SiO_2$/P(7-6-AC)-*b*-PNIPAAm disperse with each other, but at the irradiation of 365 nm, the $SiO_2$/P(7-6-AC)-*b*-PNIPAAm aggregate together (Figure 7b), which can be due to the photodimerization of the coumarin groups. Therefore, we can find the same result on the SEM images (Figure 7c and Figure 7d). And a great number of cavities have also been constructed among the $SiO_2$/P(7-6-AC)-*b*-PNIPAAm in the process of the UV irradiation at 365 nm.

The agglomeration of the prepared $SiO_2$/P(7-6-AC)-*b*-PNIPAAm caused by temperature and UV light are also investigated by dynamic light scattering (DLS). Figure 8b shows the size of $SiO_2$/P(7-6-AC)-*b*-PNIPAAm based on DLS results changed with temperature and the UV irradiation at 365 nm. As shown in Figure 8a, the radius of hydration of the $SiO_2$/P(7-6-AC)-*b*-PNIPAAm were about 50 nm, while the temperature rises to 35°C, the radius of hydration increases up to 90 nm. The results indicate that the block polymer around the silica nanosphere is responsible for temperature, and the formation of the aggregates changed with temperature. Compared with the original $SiO_2$/P(7-6-AC)-*b*-PNIPAAm nanosphere, when the temperature rise to 35°C, the size of the $SiO_2$/P(7-6-AC)-*b*-PNIPAAm nanosphere is up to 90 from 50 nm. On the other hand, the size of the $SiO_2$/P(7-6-AC)-*b*-PNIPAAm nanosphere after the UV irradiation at 365 nm is up to 350 nm (25°C) from 50 nm, and further increased to 530 nm after the temperature rising to 35°C (Figure 6b), which can be attributed to the crosslinking of the coumarin after photodimerization. The data of DLS are consistent with the results of TEM, and it also shows the same results with the images of atomic force microscope (AFM).

The mechanism of photo-sensitive and thermal-sensitive of $SiO_2$/P(7-6-AC)-*b*-PNIPAAm is proposed in Figure 9. The photodimerization of the coumarins is the primary factor for photo-sensitivity, and the formation of cyclobutane rings ([2π + 2π]s cycloaddition) (Figure 9a) leads to the aggregation of $SiO_2$/P(7-6-AC)-*b*-PNIPAAm, which will be further illustrated by TEM. In general, there are two main mechanisms for the explanation of the thermal-sensitivity of PNIPAAm. One is the change of the temperature leading to the change of the polymer structure transition from linear structure to a nearly spherical structure [53]. Another one is the formation and rupture of the hydrogen bonds [54]. In $SiO_2$/P (7-6-AC)-*b*-PNIPAAm, we think that the thermal-sensitivity can be mostly attributed to the formation and rupture of hydrogen bonds between water and amide (Figure 9b). It is favorable for the formation of hydrogen bonds between the water molecules and amide bond under low temperature, while the hydrogen bonds are broken under high temperature.

In general, contact angle (CA) is used to estimate the wettability of a solid surface. Figure 10 describes the changes of contact angles and the reversible wettability transitions of the surface of $SiO_2$/P(7-6-AC)-*b*-PNIPAAm on glass slide by alternating the temperature and UV irradiations at the wavelengths of 365 and 254 nm. Obviously, the $SiO_2$ particles grafted with block polymer exhibit the hydrophobic behavior (CA = 98±2° Figure 10 a) below the lower criti-

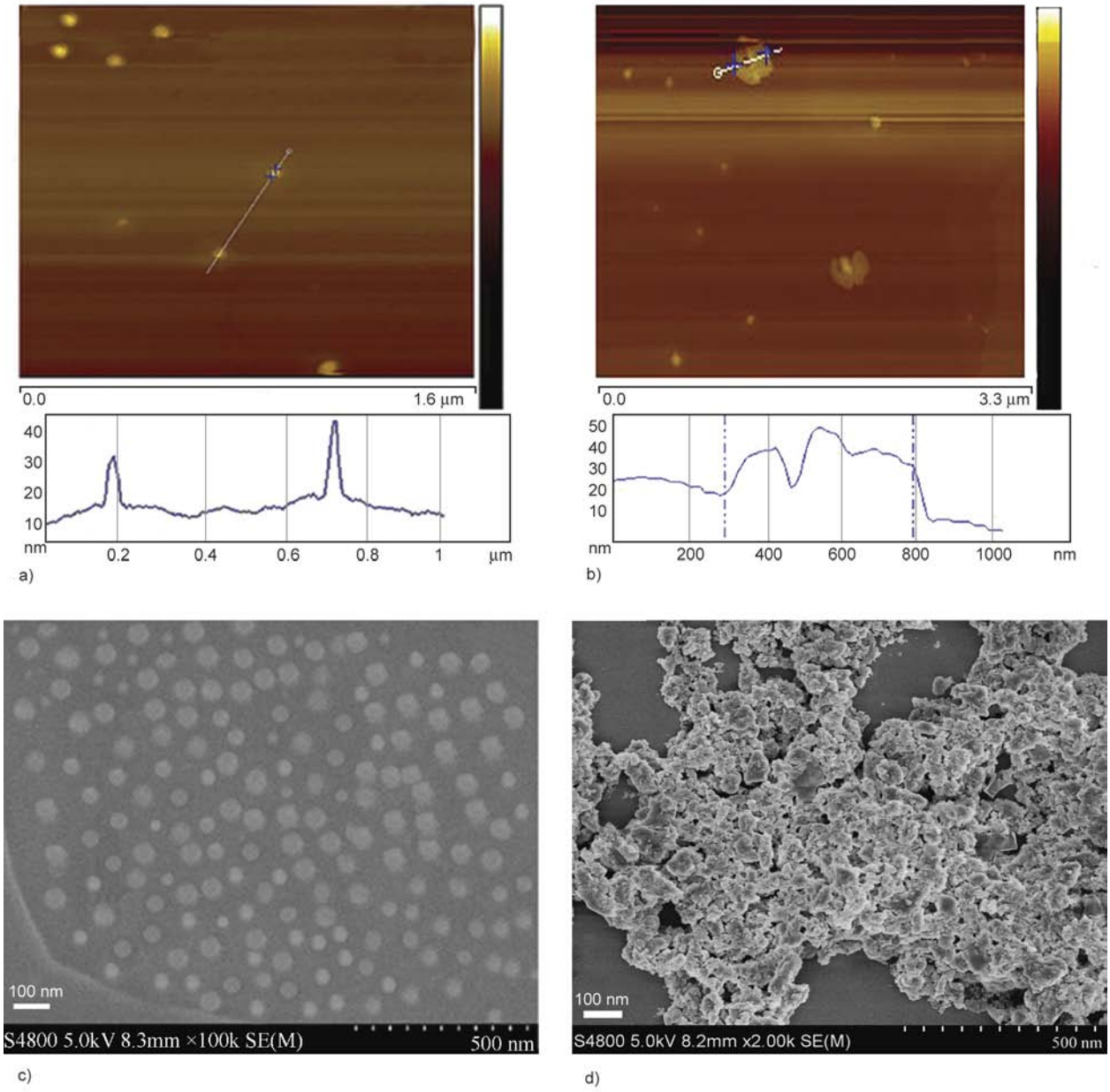


**Figure 7.** The AFM (a, b) and SEM (c, d) images of $SiO_2$/P(7-6-AC)-*b*-PNIPAAm upon 254 and 365 nm UV light irradiation, respectively

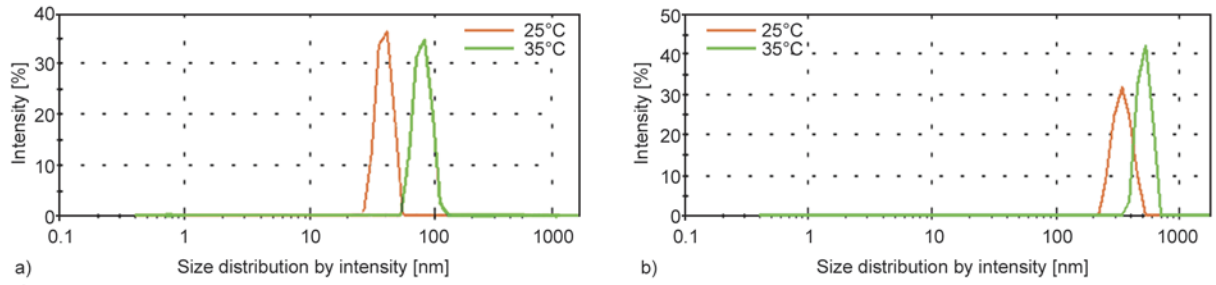


**Figure 8.** The size distribution of $SiO_2$/P(7-6-AC)-*b*-PNIPAAm nanoparticles (a) UV light at 254 nm and (b) UV light at 365 nm

cal solution temperature (LCST =32°C). However, the CA increased evidently to 137±2° (Figure 10b) when the temperature was up to 40°C, and the contact angle can further increase once again to 157±2° (Figure 10d) after UV irradiation at 365 nm, which shows the superhydrophobic property. On the other

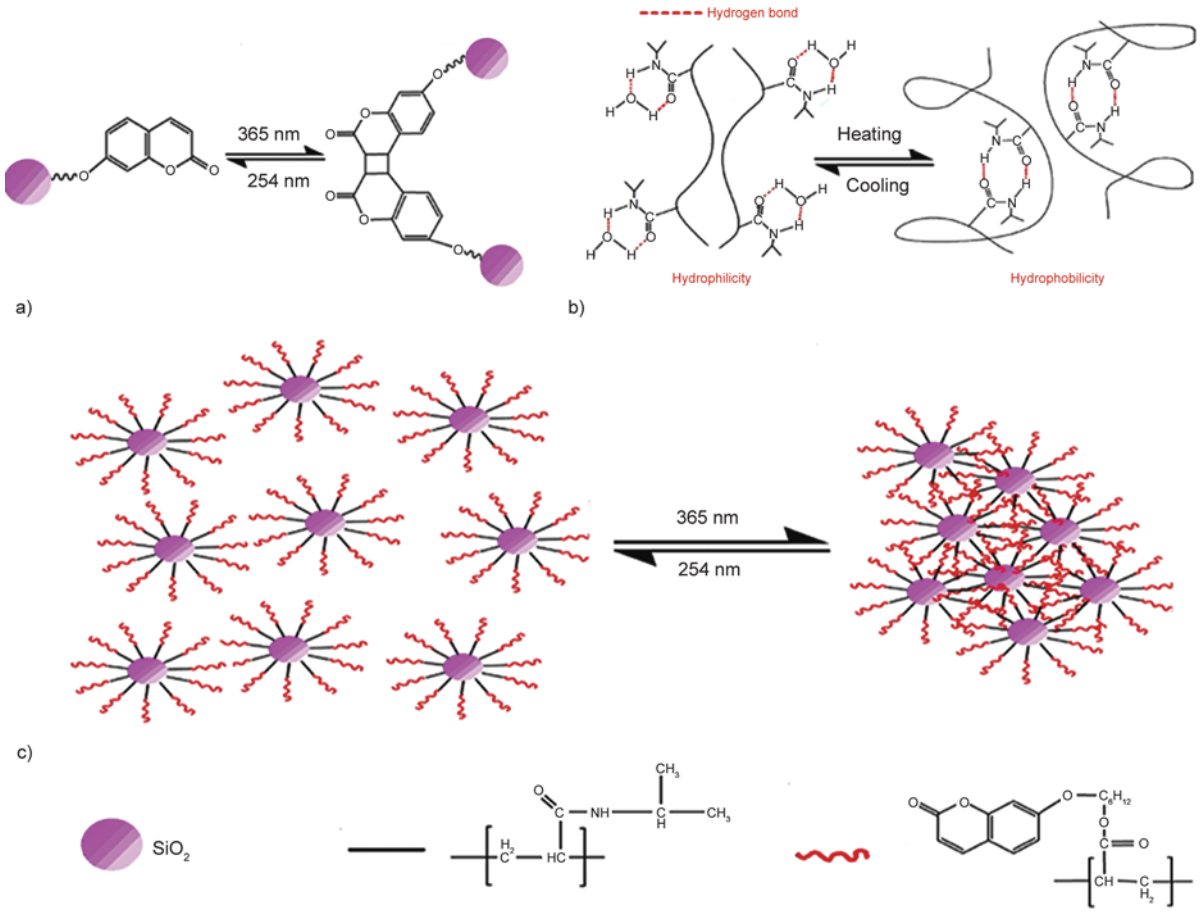


**Figure 9.** The mechanism for photoreaction and thermal-sensitive of the $SiO_2$/P (7-6-AC)-*b*-PNIPAAm: (a) photodimerization of coumarin, (b) the thermal-sensitive mechanism of PNIPAAm, (c) the morphological characteristics of the prepared nanoparticles under different UV irradiation

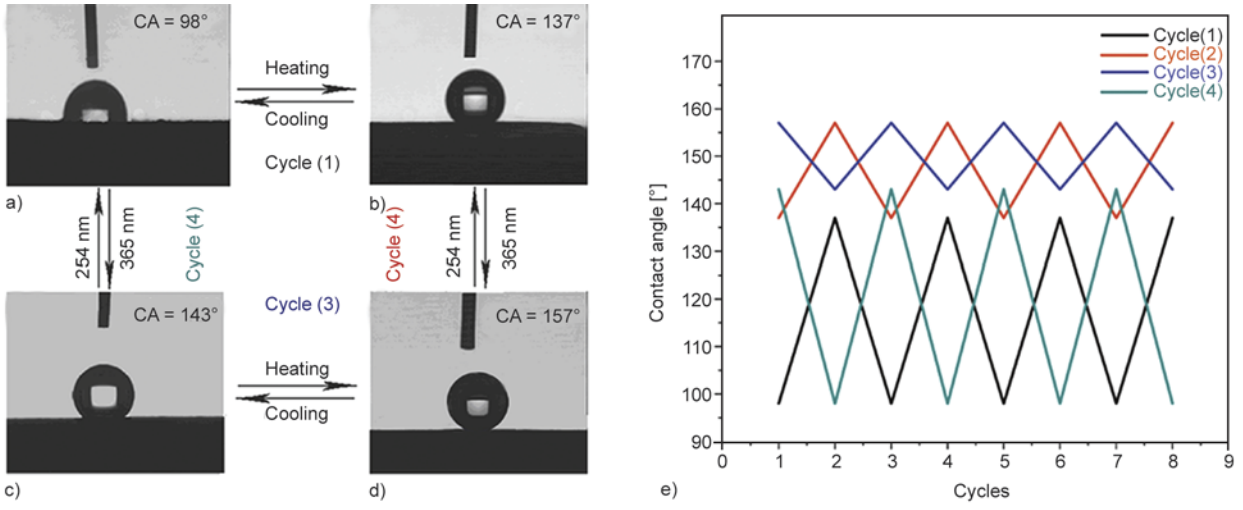


**Figure 10.** The changes of contact angles (a)–(d) and the reversible wettability transitions (e) of the surface of $SiO_2$/P(7-6-AC)-*b*-PNIPAAm particles on glass slide by alternating the temperature and UV irradiations at the wavelengths of 365 and 254 nm. The interval time of each cycle is five days.

hand, we change the order of the stimulation, first irradiating at 365 nm and then heating to 40°C, the same result (157±2°) can be obtained. It is noted that the superhydrophobic surface can return to the original state by changing temperature (143±2°) and using UV irradiations at the wavelengths of 254 nm. The results suggest that the surface with the reversible wettability transitions properties has been acquired

by $SiO_2$/P(7-6-AC)-*b*-PNIPAAm particles. To explore the thermal-sensitive and photo-sensitive behavior of the surface, cycles between hydrophobic and superhydrophobic are shown in Figure 10e. We repeatedly irradiated the particle surface with alternating UV light at 365 and 254 nm, heating and cooling, and measured the value of the CA as shown in Figure 10e. These results prove that the surface wettability can be reversibly tuned for several cycles. The results show excellent reversibility and a quick transformation between hydrophobicity and superhydrophobicity. Each cycle lasts only several minutes. It was reported that PNIPAAm [55] shows its LCST at 32°C in aqueous solution. The hydrogen bond is formed between the water and N-isopmpylacrylamide group when the temperature under the LCST, and it will display the hydrophilic properties. Upon heating, the predominantly intermolecular hydrogen bonding between the PNIPAAm chains and water molecules, which contributes to the hydrophilicity and relaxed PNIPAAm chains, is replaced by intramolecular hydrogen bonding between C=O and N–H groups along the PNIPAAm chains. This results in compact and collapsed chains that interact minimally with water and thus exhibit hydrophobicity.(Figure 6b).

N-isopmpylacrylamide group becomes exposed and leads to a low surface free energy and large water CAs, and the surface showed the hydrophobic property. Oppositely, the hydrogen bond is formed between water and amide, shown its hydrophilicity of as prepared $SiO_2$ particles at the temperature lower than 32°C. The photo-sensitive behavior of the surface can be mainly attributed to the coumarin group in the block polymer. At the irradiation of 365 nm, the coumarin groups crosslink with each other and form the disordered structure surrounding the silica.

The TEM results (Figure 6c) have demonstrated that a well-defined core-shell structure with $SiO_2$ as core and block polymer as shell had been constructed. Therefore, the particles convert into a series of aggregations and the air trapping forming among the aggregations at the same time after UV irradiation at 365 nm, which will result in the construction of the hierarchical structure [56].

According to the results observed from AFM and SEM images (Figure 8), the surface can be constructed a hierarchical structure for the formation of a series of branched and rugby-ball-like nanoparticles, which indicates that this hierarchical structure has the largest roughness. On the other hand, 7-(6-(acryloyloxy) hexyloxy) coumarin possess a lower surface energy for the alkyl chains, which may affect the hydrophobic property of the coatings. As for the thermal-sensitivity, the oxygen groups on the prepared nanoparticles may be wrapped with alkyl chains and be trapped between particles after 365 nm UV irradiation to avoid forming hydrogen bonds with water. As a result, the CA increases with irradiation time. After photocleavage of the dimers, there is no chemical bonding between the prepared nanoparticles, and water molecules interact with oxygen groups by forming hydrogen bonds to decrease the CA.

The Wenzel and Cassie mode can explain well why the surface switches from hydrophobicity to superhydrophobicity after the irradiation of UV at 365 nm. And it also demonstrates that the mutual transformation between Wenzel model and Cassie model can be occurred via UV irradiation. The Wenzel model can also be used to explain the static contact angle. As described by Wenzel's Equation (2) [57]:

$$\cos\theta = r\cos\theta_r \tag{2}$$

where is the roughness coefficient and the $\theta_Y$ is the static contact angle calculated by Young's equation. After the 365 nm UV irradiation, the rough surface comes into contact with water, air trapping in the rough area may occur, which would contribute greatly to the increase of hydrophobicity. By now, because of the air trapping in the trough area, the Cassie model was used to calculate the static contact angle. The Cassie's equation can by described by Equation (3):

$$\cos\theta = f\cos\theta_Y - (1 - f) \tag{3}$$

where $f$ is the fraction of the liquid–solid interface, while $(1 - f)$ is the air–liquid interface. And the air trapping would contribute greatly to the increase of hydrophobicity.

## 4. Conclusions

In conclusion, a stable superhydrophobic surface with thermal- and photo-sensitivity was fabricated successfully by a facile approach which combined technology of RAFT with click-chemistry. The $SiO_2$ particles as prepared form the air trapping by the photoisomerization of coumarin groups under 365 nm UV irradiation along with the Wenzel Cassie

transition, and the formation and rupture of hydrogen bond between amide and water were controlled by the changing of temperature, all resulting in the CA changing from 98±2 to 157±2°. The repeated experiments of the CA changing indicate that the surface wettability can be transformed between hydrophobicity to superhydrophobicity reversibly, indicating that the surface has good stability. This novel method using RAFT technology to synthesize multiple responsive block polymers will be widely used in fabricating multiple responsive superhydrophobic surfaces. The multiple responsive superhydrophobic surfaces have great potential application in the controlled release of drugs fields and the fabrication of responsive switches.

## Acknowledgements

This work was supported by the Research Fund for the Doctoral Program of Higher Education of China (20120161110024) and the National Natural Science Foundation of China (No. J1210040).

## References

[1] Boinovich L., Emelyanenko A. M., Pashinin A. S.: Analysis of long-term durability of superhydrophobic properties under continuous contact with water. ACS Applied Materials and Interfaces, **2**, 1754–1758 (2010). DOI: 10.1021/am100241s

[2] Sun T., Feng L., Gao X., Jiang L.: Bioinspired surfaces with special wettability. Accounts of Chemical Research, **38**, 644–652 (2005). DOI: 10.1021/ar040224c

[3] Verplanck N., Coffinier Y., Thomy V., Boukherroub R.: Wettability switching techniques on superhydrophobic surfaces. Nanoscale Research Letters, **2**, 577–596 (2007). DOI: 10.1007/s11671-007-9102-4

[4] Liu Y., Mu L., Liu B., Kong J.: Controlled switchable surface. Chemistry: A European Journal, **11**, 2622–2631 (2005). DOI: 10.1002/chem.200400931

[5] Wang X., Gao M.: A facile route for preparing rhabdophane rare earth phosphate nanorods. Journal of Materials Chemistry, **16**, 1360–1365 (2006). DOI: 10.1039/B517179B

[6] Han J. T., Lee D. H., Ryu C. Y., Cho K.: Fabrication of superhydrophobic surface from a supramolecular organosilane with quadruple hydrogen bonding. Journal of the American Chemical Society, **126**, 4796–4797 (2004). DOI: 10.1021/ja0499400

[7] Russell T. P.: Surface-responsive materials. Science, **297**, 964–968 (2002). DOI: 10.1126/science.1075997

[8] Feng C. L., Zhang Y. J., Jin J., Song Y. L., Xie L., Qu G., Jiang L., Zhu D.: Reversible wettability of photoresponsive fluorine-containing azobenzene polymer in Langmuir–Blodgett films. Langmuir, **17**, 4593–4598 (2001). DOI: 10.1021/la010071r

[9] Calliesa M., Quéré D.: On water repellency. Soft Matter, **1**, 55–61 (2005). DOI: 10.1039/B501657F

[10] Nosonovsky M., Bhushan B.: Hierarchical roughness makes superhydrophobic states stable. Microelectronic Engineering, **84**, 382–386 (2007). DOI: 10.1016/j.mee.2006.10.054

[11] Wang M., Chen C., Ma J., Xu J.: Preparation of superhydrophobic cauliflower-like silica nanospheres with tunable water adhesion. Journal of Materials Chemistry, **21**, 6962–6966 (2011). DOI: 10.1039/C1JM10283D

[12] Li J., Liu X., Ye Y., Zhou H., Chen J.: Fabrication of superhydrophobic CuO surfaces with tunable water adhesion. Journal of Physical Chemistry C, **115**, 4726–4730 (2011). DOI: 10.1021/jp111296n

[13] Feng X. J., Jiang L.: Design and creation of superwetting/antiwetting surfaces. Advanced Materials, **18**, 3063–3078 (2006). DOI: 10.1002/adma.200501961

[14] Azzaroni O., Brown A. A., Huck W. T. S.: Tunable wettability by clicking counterions into polyelectrolyte brushes. Advanced Materials, **19**, 151–155 (2007). DOI: 10.1002/adma.200601257

[15] Fan X., Jiang L.: Bio-inspired, smart, multiscale interfacial materials. Advanced Materials, **20**, 2842–2858 (2008). DOI: 10.1002/adma.200800836

[16] Wang S., Song Y., Jiang L.: Photoresponsive surfaces with controllable wettability. Journal of Photochemistry and Photobiology C: Photochemistry Reviews, **8**, 18–29 (2007). DOI: 10.1016/j.jphotochemrev.2007.03.001

[17] Chen H., Pan S., Xiong Y., Peng C., Pang X., Li L., Xiong Y., Xu W.: Preparation of thermo-responsive superhydrophobic $TiO_2$/poly(*N*-isopropylacrylamide) microspheres. Applied Surface Science, **258**, 9505–9509 (2012). DOI: 10.1016/j.apsusc.2012.04.096

[18] Wu D., Wu S-Z., Chen Q-D., Zhang Y-L, Yao J., Yao X., Niu L-G., Wang J-N., Jiang L., Sun H-B.: Curvature-driven reversible in situ switching between pinned and roll-down superhydrophobic states for water droplet transportation. Advanced Materials, **23**, 545–549 (2011). DOI: 10.1002/adma.201001688

[19] Feng N., Zhao H., Zhan J., Tia D., Li H.: Switchable wettability sensor for ion pairs based on calix[4]aza-crown clicking. Organic Letters, **14**, 1958–1961 (2012). DOI: 10.1021/ol203226q

[20] Bi H., Yin K., Xie X., Zhou Y., Wan N., Xu F., Banhart F., Sun L., Ruoff R. S.: Low temperature casting of graphene with high compressive strength. Advanced Materials, **22**, 5125–5128 (2012).
DOI: 10.1002/adma.201201519

[21] Stayton P. S., Shimoboji T., Long C., Chilkoti A., Ghen G., Harris J. M., Hoffman A. S.: Control of protein–ligand recognition using a stimuli-responsive polymer. Nature, **378**, 472–474 (1995).
DOI: 10.1038/378472a0

[22] Dai S., Ravi P., Tam K. C.: Thermo- and photo-responsive polymeric systems. Soft Matter, **5**, 2513–2533 (2009).
DOI: 10.1039/B820044K

[23] Jochum F. D., zur Borg L., Roth P. J., Theato P.: Thermo- and light-responsive polymers containing photoswitchable azobenzene end groups. Macromolecules, **42**, 7854–7862 (2009).
DOI: 10.1021/ma901295f

[24] Jochum F. D., Theato P.: Temperature and light sensitive copolymers containing azobenzene moieties prepared via a polymer analogous reaction. Polymer, **50**, 3079–3085 (2009).
DOI: 10.1016/j.polymer.2009.05.041

[25] Xia F., Feng L., Wang S., Sun T., Song W., Jiang W., Jiang L.: Dual-responsive surfaces that switch between superhydrophilicity and superhydrophobicity. Advanced Materials, **18**, 432–436 (2006).
DOI: 10.1002/adma.200501772

[26] Das S., Ranjan P., Maiti P. S., Singh G., Leitus G., Klajn R.: Dual-responsive nanoparticles and their self-assembly. Advanced Materials, **25**, 422–426 (2013).
DOI: 10.1002/adma.201201734

[27] Liu H., Li Y., Sun K., Fan J., Zhang P., Meng J., Wang S., Jiang L.: Dual-responsive surfaces modified with phenylboronic acid-containing polymer brush to reversibly capture and release cancer cells. Journal of the American Chemical Society, **135**, 7603–7609 (2013).
DOI: 10.1021/ja401000m

[28] Fu Q., Rao G. V. R., Basame S. B., Keller D. J., Artyushkova K., Fulghum J. E. G., López P.: Reversible control of free energy and topography of nanostructured surfaces. Journal of the American Chemical Society, **126**, 8904–8905 (2004).
DOI: 10.1021/ja047895q

[29] Liu Y., Zhao M., Bergbreiter D. E., Crooks R. M.: pH-switchable, ultrathin permselective membranes prepared from multilayer polymer composites. Journal of the American Chemical Society, **119**, 8720–8721 (1997).
DOI: 10.1021/ja972075h

[30] Roy D., Cambre J. N., Sumerlin B. S.: Future perspectives and recent advances in stimuli-responsive materials. Progress in Polymer Science, **35**, 278–301 (2010).
DOI: 10.1016/j.progpolymsci.2009.10.008

[31] Rosario R., Gust D., Garcia A. A., Hayes M., Taraci J. L., Clement T., Dailey J. W., Picraux S. T.: Lotus effect amplifies light-induced contact angle switching. Journal of Physical Chemistry B, **108**, 12640–12642 (2004).
DOI: 10.1021/jp0473568

[32] Li L., Pan S., Pang X., Chen H., Hu D., Ke L., Xiong Y., Xu W.: Fabrication of a coumarin-driven switchable superhydrophobic silica surface by photochemistry. Soft Matter, **8**, 7357–7360 (2012).
DOI: 10.1039/c2sm25888a

[33] Pang X., Pan S., Feng S., Chen H., Li L., Su X., Xiong Y., Xu W.: Photoreversible superhydrophobic surfaces with switchable sticky-rolling state of water droplets. Macromolecular Materials and Engineering, **297**, 979–984 (2012).
DOI: 10.1002/mame.201100386

[34] Lim M. H., Stein A.: Comparative studies of grafting and direct syntheses of inorganic–organic hybrid mesoporous materials. Chemistry of Materials, **11**, 3285–3295 (1999).
DOI: 10.1021/cm990369r

[35] Peng J., Yu P., Zeng S., Liu X., Chen J., Xu W.: Application of click chemistry in the fabrication of cactus-like hierarchical particulates for sticky superhydrophobic surfaces. Journal of Physical Chemistry C, **114**, 5926–5931 (2010).
DOI: 10.1021/jp909430z

[36] Liu R., Guo Y., Oldusote G., Qu F., Priestley R. D.: Core–shell $Fe_3O_4$ polydopamine nanoparticles serve multipurpose as drug carrier, catalyst support and carbon adsorbent. ACS Applied Materials and Interfaces, **18**, 9167–9171 (2013).
DOI: 10.1021/am402585y

[37] Kehrlösser D., Träger J., Kim H-C., Hampp N.: Synthesis and photochemistry of coumarin-based self-assembled monolayers on silicon oxide surfaces. Langmuir, **26**, 3878–3882 (2010).
DOI: 10.1021/la903433r

[38] Liu J-G., Nakamura Y., Suzuki Y., Shibasaki Y., Ando S., Ueda M.: Highly refractive and transparent polyimides derived from 4,4′-[*m*-sulfonylbis(phenylenesulfanyl)]diphthalic anhydride and various sulfur-containing aromatic diamines. Macromolecules, **40**, 7902–7907 (2007).
DOI: 10.1021/ma0713714

[39] Babin J., Pelletier M., Lepage M., Allard J-F., Morris D., Zhao Y.: A new two-photon-sensitive block copolymer nanocarrier. Angewandte Chemie International Edition, **48**, 3329–3332 (2009).
DOI: 10.1002/anie.200900255

[40] Ting S. S. R., Granville A. M., Quémener D., Davis T. P., Stenzel M. H., Barner-Kowollik C.: RAFT chemistry and huisgen 1,3-dipolar cycloaddition: A route to block copolymers of vinyl acetate and 6-*O*-methacryloyl mannose? Australian Journal of Chemistry, **60**, 49–50 (2007).
DOI: 10.1071/CH07089

[41] Schricker S., Palacio M., Thirumamagal B. T. S., Bhushan B.: Synthesis and morphological characterization of block copolymers for improved biomaterials. Ultramicroscopy, **110**, 639–649 (2010). DOI: 10.1016/j.ultramic.2010.02.025

[42] Zhang T., Wu Y., Pan X., Zheng Z., Ding X., Peng Y.: An approach for the surface functionalized gold with pH-responsive polymer by combination of RAFT and click chemistry. European Journal Polymer, **45**, 1625–1633 (2009). DOI: 10.1016/j.eurpolymj.2009.03.016

[43] Nambiar R., Woody K. B., Ochocki J. D., Brizius G. L., Collard D. M.: Synthetic approaches to regioregular unsymmetrical dialkoxy-substituted poly(1,4-phenylene ethynylene)s. Macromolecules, **42**, 43–51 (2009). DOI: 10.1021/ma802215y

[44] Yen Y-C., Ye Y-S., Cheng C-C., Lu C-H., Tsai L-D., Huang J-M., Chang F-C.: The effect of sulfonic acid groups within a polyhedral oligomeric silsesquioxane containing cross-linked proton exchange membrane. Polymer, **51**, 84–91 (2010). DOI: 10.1016/j.polymer.2009.11.033

[45] Ballesteros O. G., Maretti L., Sastre R., Scaiano J. C.: Kinetics of cap separation in nitroxide-regulated 'living' free radical polymerization: Application of a novel methodology involving a prefluorescent nitroxide switch. Macromolecules, **34**, 6184–6187 (2001). DOI: 10.1021/ma0103831

[46] Shen X., Kitajyo Y., Duan Q., Narumi A., Kaga H., Kaneko N., Satoh T., Kakuchi T.: Synthesis and photocrosslinking reaction of *N*-allylcarbamoylmethyl cellulose leading to hydrogel. Polymer Bulletin, **56**, 137–143 (2006). DOI: 10.1007/s00289-005-0482-2

[47] Zhuravlev L. T.: Structurally bound water and surface characterization of amorphous silica. Pure and Applied Chemistry, **61**, 1969–1976 (1989). DOI: 10.1351/pac198961111969

[48] Zhou L., Gao C., Xu W.: Efficient grafting of hyperbranched polyglycerol from hydroxyl-functionalized multiwalled carbon nanotubes by surface-initiated anionic ring-opening polymerization. Macromolecular Chemistry and Physics, **210**, 1011–1018 (2009). DOI: 10.1002/macp.200900134

[49] Chen J., Liu M., Chen C., Gong H., Gao C.: Synthesis and characterization of silica nanoparticles with well-defined thermoresponsive PNIPAM via a combination of RAFT and click chemistry. ACS Applied Materials and Interfaces, **3**, 3215–3223 (2011). DOI: 10.1021/am2007189

[50] Guo T-Y., Liu P., Zhu J-W., Song M-D., Zhang B-H.: Well-defined lactose-containing polymer grafted onto silica particles. Biomacromolecules, **7**, 1196–1202 (2006). DOI: 10.1021/bm051011t

[51] Trenor S. R., Shultz A. R., Love B. J., Long T. E.: Coumarins in polymers: From light harvesting to photocross-linkable tissue scaffolds. Chemical Reviews, **104**, 3059–3062 (2004). DOI: 10.1021/cr030037c

[52] Yilgor L., Bilgin S., Isik M., Yilgor E.: Tunable wetting of polymer surfaces. Langmuir, **28**, 14808–14814 (2012). DOI: 10.1021/la303180k

[53] Zhang J. L., Srivastava R. S., Misra R. D. K.: Core–shell magnetite nanoparticles surface encapsulated with smart stimuli-responsive polymer: Synthesis, characterization, and LCST of viable drug-targeting delivery system. Langrnuir, **23**, 6342–6351 (2007). DOI: 10.1021/la0636199

[54] Chen M., Dong M., Havelund R., Regina V. R., Meyer R. L., Besenbacher F., Kingshott P.: Thermo-responsive core–sheath electrospun nanofibers from poly (*N*-isopropylacrylamide)/polycaprolactone blends. Chemistry of Materials, **22**, 4214–4221 (2010). DOI: 10.1021/cm100753r

[55] Rueda J., Zschoche S., Komber H., Schmaljohann D., Voit B.: Synthesis and characterization of thermoresponsive graft copolymers of NIPAAm and 2-alkyl-2-oxazolines by the 'grafting from' method. Macromolecules, **38**, 7330–7336 (2005). DOI: 10.1021/ma050570p

[56] Pan S., Kota A. K., Mabry J. M., Tuteja A.: Superomniphobic surfaces for effective chemical shielding. Journal of the American Chemical Society, **135**, 578–581 (2013). DOI: 10.1021/ja310517s

[57] Nishino T., Meguro M., Nakamae K., Matsushita M., Ueda Y.: The lowest surface free energy based on $-CF_3$ alignment. Langmuir, **15**, 4321–4324 (1999). DOI: 10.1021/la981727s